Development of photonic technologies for astronomical instruments using ultrafast laser inscription

David Guillaume MacLachlan

Submitted for the degree of Doctor of Philosophy

Heriot Watt University

School of Engineering and Physical Sciences

February 2017

Abstract

Recently there has been a desire to apply photonic concepts and technologies to astronomical applications, with the aim of replacing traditional bulk optic instruments. This astrophotonic approach is envisioned to produce compact devices that have the potential to provide the unprecedented precision and stability required for current astronomical goals, such as the detection of Earth-like exoplanets capable of supporting life.

The work in this thesis covers the investigation of the technique of Ultrafast Laser Inscription (ULI) to create the building blocks that may lead to a fully integrated compact spectrograph for astronomy. Unlike conventional fabrication technologies, ULI allows custom three-dimensional optical devices to be directly inscribed within a bulk substrate.

Volume gratings with high first order diffraction efficiencies optimised for a variety of wavelengths are demonstrated, with a view to providing efficient gratings for the mid-infrared wavelength range. Initially the mid infrared transmitting material GLS was used to create gratings with a first order efficiency of 63 % up to a wavelength of 1.35 μm. Anti-reflection coatings were applied to GLS and gratings with an efficiency of 95 % at 1.02 μm were produced.

A second material, IG2 was used and diffraction gratings with a first order efficiency of 63 % were produced, which were efficient up to a wavelength of 2.5 μm, with thicker gratings produced which have yet to be characterised in a mid-infrared setup. These developments show that practical mid-infrared volume gratings can be produced by the process of ULI.

Photonic reformatters have also been developed to reshape a multimode telescope point spread function into a pseudo-slit, suitable as an input for a diffraction-limited spectrograph. Two device designs were investigated. The first was a fully integrated ULI component which, tested in the laboratory reformatted a multimode input at 1550 nm into a slit, single mode in one axis and highly multimode in the orthogonal axis with an efficiency of 66 %. The device was tested on-sky at the William Herschel Telescope and performed with an efficiency of 19.5 % over the wavelength range 1450 to 1610 nm.

The second, improved device combined a ULI component with a multicore fibre component, and performed with a similar performance in the laboratory demonstrating an efficiency of 69 %, but a much improved on sky efficiency of 53 % showing a potential for such devices to be used as an input for a diffraction limited spectrograph.

To my Grandad, Ernie.

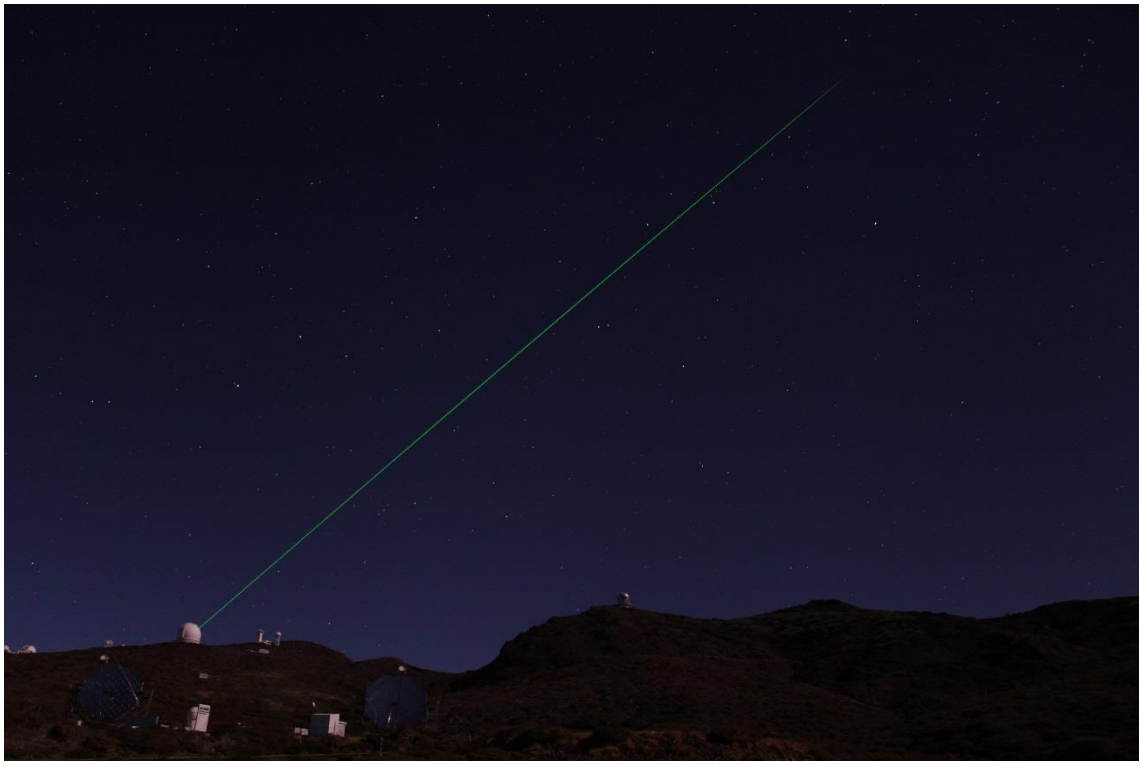

CANARY laser guide star at the William Herschel Telescope, La Palma.

Acknowledgements

Firstly, I would like to thank Professor Robert Thomson, my academic supervisor for the opportunity to do this PhD and all his help and support throughout, in particular for his patience in the very painful process of writing up this thesis.

I would like to thank all the members of the Photonic Instrumentation group for all their work and assistance, in particular Dr Debaditya Choudhury who has been invaluable in staying late and assisting with several deadlines and help writing and checking papers.

I also thank Optoscribe, in particular Dr Graham Brown for assistance in using the stages and the chance to adapt and use his programming code for initial device inscription.

I would also like to thank Professor Ajoy Kar for his support, particularly in the early years with access to his labs and equipment when first starting out. I am additionally very thankful for the opportunity to travel to a conference in India with him and his group.

I thank the staff at the Edinburgh Astronomy and Technology Centre, in particular Professor Colin Cunningham and Dr David Lee for the opportunity to use their labs and equipment in the development and testing of the volume gratings, without whom this work would not have been possible.

I would like to thank Dr Jeremy Allington-Smith and Dr Robert Harris of Durham University for all their work on the photonic reformatter, in particular Robert Harris for the challenging summer we spent at Heriot-Watt designing and manufacturing the photonic dicer.

I would also like to thank the entire CANARY AO demonstrator team, in particular Professor Richard Myers, Dr Tim Morris and Dr Alistair Basden of Durham University and Dr Eric Gendron of l'Observatoire de Paris for the opportunity to travel out to La Palma and test the photonic reformatters on their system at the William Herschel Telescope. Additionally, I thank the team at the Centre for Advanced Instrumentation in Durham University for making me very welcome in my trip there.

I would also like to thank Professor Tim Birks and Dr Itandehui Gris-Sánchez from the University of Bath for manufacturing the multicore fibre photonic lanterns without which the hybrid reformatter would not have been possible.

I wish to thank my office mates for keeping me grounded and sane throughout this experience.

Last but not least I wish to thank all my family in particular Mum, Dad and Grandma for all their support, patience and, when required nagging to complete this opportunity.

ACADEMIC REGISTRY
Research Thesis Submission

Name*:*	David Guillaume MacLachlan		
School:	Engineering and Physical Sciences		
Version: *(i.e. First, Resubmission, Final)*	Final	Degree Sought:	PhD (Physics)

Declaration

In accordance with the appropriate regulations I hereby submit my thesis and I declare that:

1) the thesis embodies the results of my own work and has been composed by myself
2) where appropriate, I have made acknowledgement of the work of others and have made reference to work carried out in collaboration with other persons
3) the thesis is the correct version of the thesis for submission and is the same version as any electronic versions submitted*.
4) my thesis for the award referred to, deposited in the Heriot-Watt University Library, should be made available for loan or photocopying and be available via the Institutional Repository, subject to such conditions as the Librarian may require
5) I understand that as a student of the University I am required to abide by the Regulations of the University and to conform to its discipline.
6) I confirm that the thesis has been verified against plagiarism via an approved plagiarism detection application e.g. Turnitin.

* *Please note that it is the responsibility of the candidate to ensure that the correct version of the thesis is submitted.*

Signature of Candidate*:*		Date:	

Submission

Submitted By *(name in capitals):*	
Signature of Individual Submitting:	
Date Submitted:	

For Completion in the Student Service Centre (SSC)

Received in the SSC by *(name in capitals):*			
Method of Submission *(Handed in to SSC; posted through internal/external mail):*			
*E-thesis Submitted (**mandatory for final theses)***			
Signature:		Date:	

Please note this form should be bound into the submitted thesis.

Contents

List of publications by the candidate

Peer reviewed journal articles

D. G. MacLachlan, R. R. Thomson, C. R. Cunningham, and D. Lee, "Mid-Infrared Volume Phase Gratings Manufactured using Ultrafast Laser Inscription," *Opt. Mater. Express* **3**, 1616–1623 (2013).

Personal contribution: fabricated all volume gratings and performed characterisation and performance tests. Significant contributions to writing of paper.

R. J. Harris, **D. G. MacLachlan**, D. Choudhury, T. J. Morris, E. Gendron, A. G. Basden, G. Brown, J. R. Allington-Smith, and R. R. Thomson, "Photonic spatial reformatting of stellar light for diffraction-limited spectroscopy," *Mon. Not. R. Astron. Soc.* **450**, 428–434 (2015).

Joint first author paper with R.J.H. Personal contributions: designed and fabricated device with R.J.H. Designed and built experimental setup with R.J.H., R.R.T. and T.M. Conducted on-sky experiment with R.J.H., R.R.T., D.C. and T.M. Peformed image analysis to determine throughput (this was also seperately performed by R.J.H. to confirm). Wrote paper in collaboration with R.J.H. R.R.T. and D.C.

D. G. MacLachlan, R. J. Harris, D. Choudhury, R. D. Simmonds, P. S. Salter, M. J. Booth, J. R. Allington-Smith, and R. R. Thomson, "Development of integrated mode reformatting components for diffraction-limited spectroscopy," *Opt. Lett.* **41**, 76–79 (2016).

Personal contributions: designed and fabricated device with R.J.H. Performed full laboratory characterisation. Wrote paper with R.R.T.

D. G. MacLachlan, R. J. Harris, I. Gris-Sánchez, D. Choudhury, T. J. Morris, E. Gendron, A. G. Basden, I. J. Spaleniak, A. Arriola, T. A. Birks, J. R. Allington-Smith, and R. R. Thomson, "Efficient photonic reformatting of celestial light for diffraction-limited spectroscopy," *Mon. Not. R. Astron. Soc.* **464**, 4950–4957 (2017).

Joint first autor paper with R.J.H. Personal contributions: designed device with R.R.T., R.J.H., I.G-S. and T.B. Fabricated and characterised reformatter component. Bonded reformatter and lantern to create full device with D.C. Designed and built experimental setup with R.J.H., R.R.T. and T.M. Conducted on-sky experiment with R.J.H., I.G-S. and T.M. Peformed image analysis to determine throughput (this was also seperately

performed by R.J.H. to confirm). Wrote paper in collaboration with R.J.H., R.R.T. and D.C.

Conference submissions

D. G. MacLachlan, D. Choudhury, A. Arriola, C. Cunningham, R. R. Thomson, A. Kirkham, and D. Lee, "Developing ultrafast laser inscribed volume gratings," *Adv. Opt. Mech. Technol. Telesc. Instrum. Proc. SPIE* **9151**, 91511H (2014).

D. G. MacLachlan, R. Harris, D. Choudhury, A. Arriola, G. Brown, J. Allington-Smith, and R. R. Thomson, "Development of integrated photonic-dicers for reformatting the point-spread-function of a telescope," *Adv. Opt. Mech. Technol. Telesc. Instrum. Proc. SPIE* **9151**, 91511W (2014).

D. G. MacLachlan, R. J. Harris, I. Gris-Sánchez, T. Morris, D. Choudhury, E. Gendron, A. Basden, I. J. Spaleniak, A. Arriola, et al., "Efficient photonic reformatting of stellar light for high precision spectroscopy," *Conf. Lasers Electro-Optics*, JF1N.5 (2016).

D. G. MacLachlan, R. J. Harris, I. Gris-Sánchez, D. Choudhury, T. J. Morris, E. Gendron, A. G. Basden, I. J. Spaleniak, A. Arriola, et al., "Development of an efficient photonic device for the reformatting of celestial light," *Adv. Opt. Mech. Technol. Telesc. Instrum. II. Proc. SPIE* **9912**, 991227–991229 (2016).

I. Spaleniak, **D. G. MacLachlan**, I. Gris-Sánchez, D. Choudhury, R. J. Harris, A. Arriola, J. R. Allington-Smith, T. A. Birks, and R. R. Thomson, "Modal noise characterisation of a hybrid reformatter," *Adv. Opt. Mech. Technol. Telesc. Instrum. II. Proc. SPIE* **9912**, 991228–991229 (2016).

D. Lee, **D. G. MacLachlan**, H. L. Butcher, R. A. Brownsword, D. Weidmann, C. R. Cunningham, H. Schnetler, and R. R. Thomson, "Mid-infrared transmission gratings in chalcogenide glass manufactured using ultra-fast laser inscription," 99122X (2016).

R. J. Harris, L. Labadie, U. Lemke, **D. G. MacLachlan**, R. R. Thomson, S. Reffert, and A. Quirrenbach, "Performance estimates for spectrographs using photonic reformatters," *Adv. Opt. Mech. Technol. Telesc. Instrum. II. Proc. SPIE* **9912**, 99125Q (2016).

Chapter 1 – Introduction

1.1 Aim

In the past few decades the telecommunications industry has experienced remarkable growth, with unprecedented connections across continents. Two of the primary technologies that have enabled this are the development of the laser [1], and low-loss optical fibres [2]. These technologies enable information to be encoded on an optical carrier wave and transmitted with low-loss over vast distances in short timescales. This has led to further investment into the development of photonic technologies, in order to increase performance and reduce costs. It has recently been proposed that many of these technologies can be adapted for other applications - in particular astronomy [3].

Recently, the first confirmed detection of planets outside our solar system was reported in 1992 with two planets identified orbiting a pulsar [4]. Advances in astronomical techniques and new specialised telescopes have led to a rapid increase in the number of planets discovered, and the ability to detect smaller planets in close orbit to their stars. This has led to the genuine possibility that life on other planets could be detected in the near future by performing atmospheric spectroscopy on small rocky planets in the habitable zone around their parent star. This has led to the current drive to design and build larger and more complex telescopes including; the 24.5 m Giant Magellan Telescope (GMT) in Chile; the 30 m Thirty Metre Telescope (TMT) in Hawaii; the 39 m European Extremely Large Telescope (E-ELT) in Chile and the 6.5 m James Webb Space Telescope (JWST).

For reasons that will become clear in this thesis, the size of a spectrograph scales with increasing telescope size. The use of conventional bulk optic technologies to create instruments for the next generation of large ground based telescopes will therefore result in very expensive instruments, which are challenging to environmentally stabilize and require larger, lower quality optics [5]. The use of photonic technologies to collect and direct the light with optical fibres and the potential to fabricate small integrated components may enable the creation of smaller, cheaper and higher precision instruments. Such components will also be lighter and as such may be suitable for use in space-based applications.

One of the most common methods of fabricating photonic components is photolithography and etching. This technique allows very small (tens of nanometres)

structures to be defined and the process can be scaled up to enable cost effective mass-production. The draw-backs of a photolithographic process are that the substrate must be flat, is most suited to creating two dimensional devices, and requires a specialist clean room environment and chemicals that may carry health risks if mishandled.

A potential alternative technique to creating photonic devices is Ultrafast Laser Inscription (ULI). This process relies on the use of ultrashort pulses of sub-bandgap radiation, which are focused within a bulk substrate to alter the material at the point of focus and induce a permanent modification to the material structure. This modification can manifest itself in a variety of ways, including alteration to the refractive index [6] and the chemical etch rate of the modified material [7]. The substrate can be translated through the laser beam on high precision mechanical stages to create fully three-dimensional structures, including waveguides. The benefits of this technique include the ability to fabricate three-dimensional structures, the ability to use a variety of substrate materials, the ability to alter the device design without having to create a new photolithography mask, and a significant reduction in the need for any post processing steps. As such, this process has been identified as one that may be suitable for applications in astronomy [8].

1.2 Thesis outline

In this thesis applications of ULI to create devices for use in future astronomical spectrographs is investigated.

Chapter 2 presents a review of astrophotonic technologies and their application to the field of astronomy. This includes; laser frequency combs to produce a calibration reference for high precision spectroscopy; photonic lanterns to efficiently convert a multimode input into an array of single modes; fibre Bragg gratings to remove bright atmospheric absorption lines and compact integrated spectrographs to increase stability and reduce instrument size.

Chapter 3 describes the technique of ULI used to produce custom three-dimensional optical devices, including the experimental setup, control parameters and the various waveguide shaping techniques that have been applied.

Chapter 4 presents the development of ULI produced volume gratings in mid-infrared transmitting materials to provide high first order diffraction efficiencies as an alternative

to volume phase holographic gratings. A detailed optimisation of the parameter space, including laser pulse energy, grating layer spacing and number of layers was performed in order to obtain optimum gratings in two separate materials. The effect of applying anti-reflection coatings to samples, both before and after modification was also investigated.

Chapter 5 describes the design, development, manufacture and testing of "photonic dicers". These components are designed to collect a multimode telescope point spread function (PSF) and reshape the output into a linear pseudo-slit that is single-mode in one axis and highly multimode in the orthogonal axis. The use of such devices has the potential to enable the use of diffraction-limited spectrographs on seeing-limited telescopes, and to enable the acquisition of astronomical spectra that are free of modal noise. The component was tested on-sky at the 4.2 m William Herschel Telescope (WHT) using the CANARY adaptive optics (AO) system as the input.

Chapter 6 presents the "hybrid reformatter" - an upgrade and improvement to the photonic dicer discussed in Chapter 5. This component combines a low loss photonic lantern created from a multicore fibre (MCF), together with a ULI manufactured reformatter component. This device was also tested at the WHT with the CANARY team, and a device with a greatly improved throughput was demonstrated which approached the performance required for astronomical applications.

Chapter 7 presents the conclusions drawn from the work presented in this thesis on the use of ULI to create devices for astronomical applications. Suggested improvements for the work and possible future devices are discussed and presented.

1.3 References

[1] T. H. Maiman, "Stimulated Optical Radiation in Ruby," *Nature* **187**, 493–494 (1960).

[2] K. C. Kao and G. A. Hockham, "Dielectric-fibre surface waveguides for optical frequencies," *IEE Proc. J - Optoelectron.* **133**, 191–198 (1986).

[3] J. Bland-Hawthorn and P. Kern, "Molding the flow of light: Photonics in astronomy," *Phys. Today* **65**, 31 (2012).

[4] A. Wolszczan and D. A. Frail, "A planetary system around the millisecond pulsar PSR1257 + 12," *Nature* **355**, 145–147 (1992).

[5] C. Cunningham, "Future optical technologies for telescopes," *Nat Phot.* **3**, 239–241 (2009).

[6] K. M. Davis, K. Miura, N. Sugimoto, and K. Hirao, “Writing waveguides in glass with a femtosecond laser,” *Opt. Lett.* **21**, 1729–1731 (1996).

[7] A. Marcinkevičius, S. Juodkazis, M. Watanabe, M. Miwa, S. Matsuo, H. Misawa, and J. Nishii, “Femtosecond laser-assisted three-dimensional microfabrication in silica,” *Opt. Lett.* **26**, 277–279 (2001).

[8] R. R. Thomson, A. K. Kar, and J. Allington-Smith, “Ultrafast laser inscription: an enabling technology for astrophotonics,” *Opt. Express* **17**, 1963–1969 (2009).

Chapter 2 – Review of the field of Astrophotonics

2.1 Motivation for astrophotonics

Astronomical instruments are almost always bespoke, one-of-a-kind instruments, that are constructed for a specific science case on a specific telescope. From an engineering perspective, they are highly impressive, often operating at cryogenic temperatures for many years at a time with minimal maintenance. However, despite their impressive nature, conventional astronomical instruments are almost always designed according to the capabilities of well-established optical technologies e.g. diffraction gratings, prisms and mirrors - devices that even Newton would have been comfortable with.

Since the 1960's a new area of optics has emerged known as photonics - the optical equivalent of electronics. The field of photonics has given birth to a range of "guided-wave" technologies, such as optical waveguides, optical fibres and Bragg gratings. These devices offer a route to provide enhanced manipulation of astronomical signals over the conventional optical technologies used in traditional astronomical instruments. Thus, over the past decade, a new field has emerged – the field of astrophotonics, which now seeks to harness the power of photonic technologies in astronomical instruments. The aims of this burgeoning field are manifold, but the hope is that astrophotonic instruments may be more compact, more precise and lower cost, but ultimately that they will provide greater scientific output. This Chapter outlines the motivations behind the field of astrophotonics, the currently used technologies if they exist, and the proposed photonic alternatives.

2.2 Multimode-to-single-mode coupling

2.2.1 Motivation

Photonic technologies are almost always designed to operate most efficiently in the single-mode (SM) regime. This is, as shall be discussed later in this Chapter, in stark contrast to astronomy, which is usually concerned with collecting and analysing highly multimode (MM) light. It is therefore immediately clear that the success of astrophotonics is reliant on the availability of a technology that facilitates the efficient coupling of multimode light to single-mode devices. The technology that can enable this

has become known as a "*photonic lantern"* – invented by Prof. Tim A. Birks at the University of Bath.

2.2.2 Photonic lanterns

The photonic lantern is a relatively new type of guided-wave device that allows the transformation of a multimode input to an array of single mode outputs (Fig. 2.1). As long as the number of single mode outputs is at least equal to, or greater than, the number of modes excited in the multimode input, and the transition is optically slow this can be achieved adiabatically and with low loss. Photonic lanterns are a key astrophotonic technology, as without them there is currently no other way to efficiently couple a seeing-limited multimode telescope PSF to single-mode photonic devices.

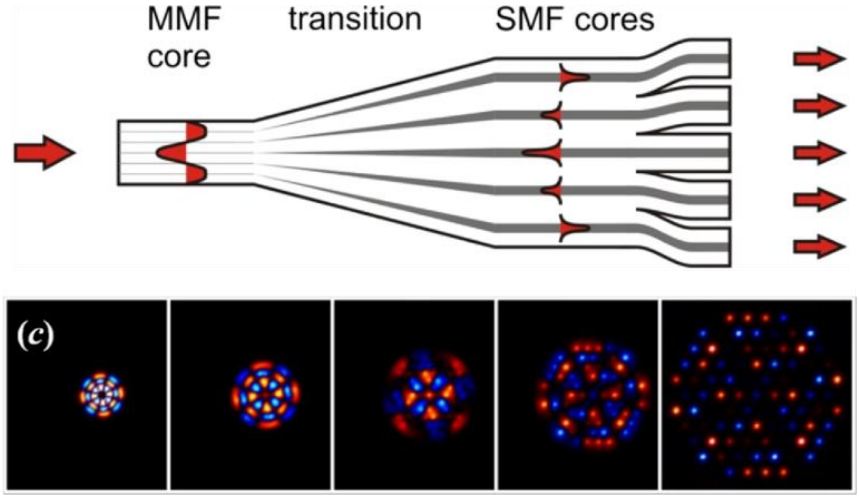

Figure 2-1 – (Top) Schematic diagram of a photonic lantern, with a bundle of single mode fibres on the right, which are drawn and fused together to form a multimode fibre core on the left, image from [1]. (Bottom) Simulated propagation of modes within an 85 core photonic lantern, showing how a multimode profile (left) transitions to an array of single mode cores (right), the colours represent opposite phases, image from [2].

2.2.1 Types of photonic lantern

2.2.1.1 Optical-fibre photonic lanterns

The first photonic lanterns were produced in 2005 and were originally fabricated using techniques borrowed from the photonic crystal fibre (PCF) field [1]. PCFs are, in many cases, glass fibres with air holes in the cladding that lower its refractive index and confine light to the core by either total internal reflection or via a photonic bandgap [3]. To

manufacture the first photonic lantern, single mode fibres were inserted into a PCF preform which contained a series of holes, with the outer ring of holes left empty (Fig. 2.2 a). The cane was then placed into a fibre drawing tower and tapered down, such that the cores of the SMFs no longer supported well confined modes, instead merging together to form a multimode system, with the outer section still containing holes functioning as the cladding (Fig. 2.2 c).

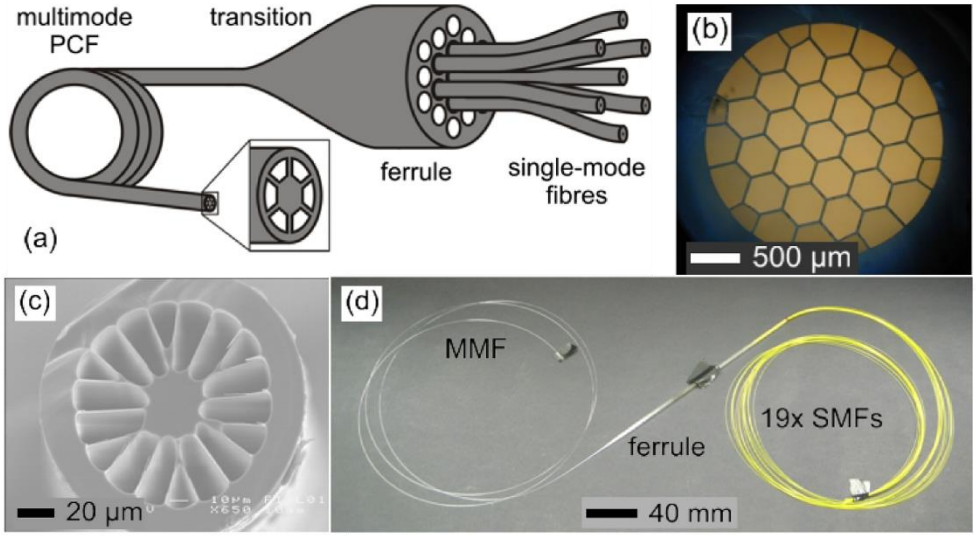

Figure 2-2 – (a) Schematic of first manufactured photonic lantern with single mode fibres integrated with a multimode photonic crystal fibre. (b) Optical micrograph of the silica cane, each of the 19 central holes will have a SMF inserted. (c) Scanning electron microscope image of multimode PCF drawn from the filled cane. (d) Photograph of the completed device. Figure from [1].

A more practical approach to manufacturing photonic lanterns was developed in 2009, that removed the need for a fibre drawing tower [4]. In this case, SMFs were bundled together and placed inside a cylindrical glass capillary, which had a lower refractive index than that of the cladding of the SMFs. This structure was then placed in a fibre tapering machine and tapered down until the cores of the SMFs are too small to support well confined modes. The claddings of the SMFs formed the core of a multimode waveguide with the cladding formed from low index capillary (Fig 2.3). A full MM-to-SM-to-MM photonic lantern produced by this stack and draw technique using 61 SMFs demonstrated an insertion loss of < 0.67 dB [5]. Stack and drawn type photonic lanterns have been used in on-sky demonstrations of SMF fibre-Bragg-gratings and arrayed-waveguide-gratings (See Sections 2.5.2.1 and 2.6.2). Unfortunately, this technique can be expensive and time consuming, and therefore may not be suited to mass production or the fabrication of lanterns supporting a large number of modes.

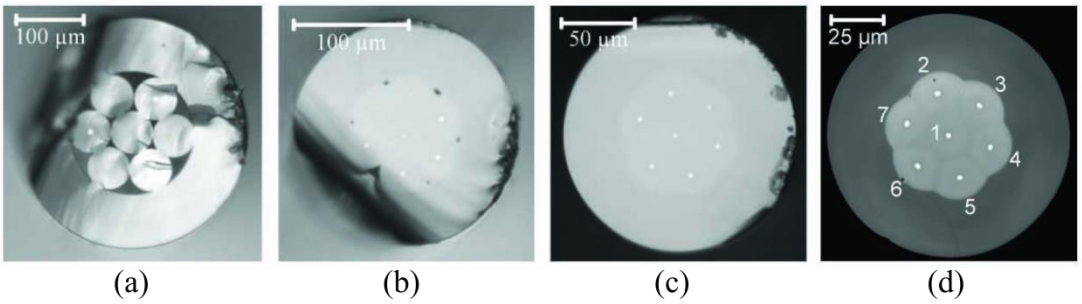

Figure 2-3 – Microscope facet images of fibre bundle cross section at different positions of the taper transition. Full taper length is 40 mm with 0 mm position referencing the single mode end, images taken at: (a) 5 mm, (b) 20 mm, (c) 25 mm and (d) 45 mm along the transition. Image from [4].

An improvement to stack and drawn devices is to use multicore fibres (MCFs), which can be encased in a capillary and similarly be drawn down to form a multimode end. Birks et al have recently demonstrated a MM-to-SM-to-MM transition with a loss of < 0.5 dB supporting 120 cores [2] (Fig 2.4). The down side of an MCF lantern is the single mode outputs are locked in a certain arrangement dictated by the arrangement of the cores in the MCF, most commonly arranged in a centred hexagonal arrangement so producing a fibre that supports 7, 19, 37, or 61, etc. modes. MCFs with a low numbers of cores can be used to feed a spectrograph using the TIGER approach [6], however a separate reformatting device would normally be required to reformat the output cores into the desired format.

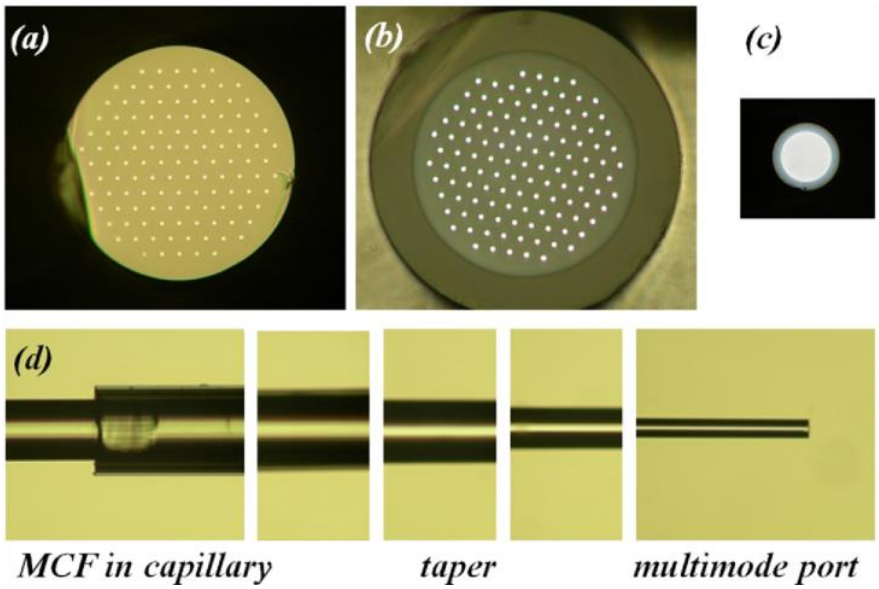

Figure 2-4 – Micrographs of: (a) 120 core MCF, (b) MCF jacketed in a capillary, (c) jacketed MCF tapered down to form a multimode input port, all to the same scale. (d) Series of micrographs showing the lantern transition, performed over a length of 20 mm. Figure from [2].

2.2.1.2 Integrated waveguide photonic lanterns

In 2011 Thomson *et al.* demonstrated that the technique of ultrafast laser inscription (ULI) (see Chapter 3) could be used to create an integrated photonic lantern in a bulk glass substrate [7] (Fig 2.5). A ULI fabricated photonic lantern was produced supporting 16 modes and demonstrating an insertion loss of < 5.7 dB, the majority of losses originating from input coupling losses that subsequent devices have improved. ULI exhibits the advantages that it can be performed in mid-infrared materials, therefore enabling a potential route to producing mid-infrared photonic lanterns [8], that may be more difficult to produce in chalcogenide fibres. The technique of ULI also allows for full three-dimensional control of the waveguide position and device design, where the output of the photonic lantern can be custom designed to suit the application and support any desired number of modes. This would permit a photonic lantern and a reformatting transition that arranges the output waveguides into a diffraction-limited pseudo-slit to be manufactured as a single monolithic device as first proposed by Thomson *et al.* [9].

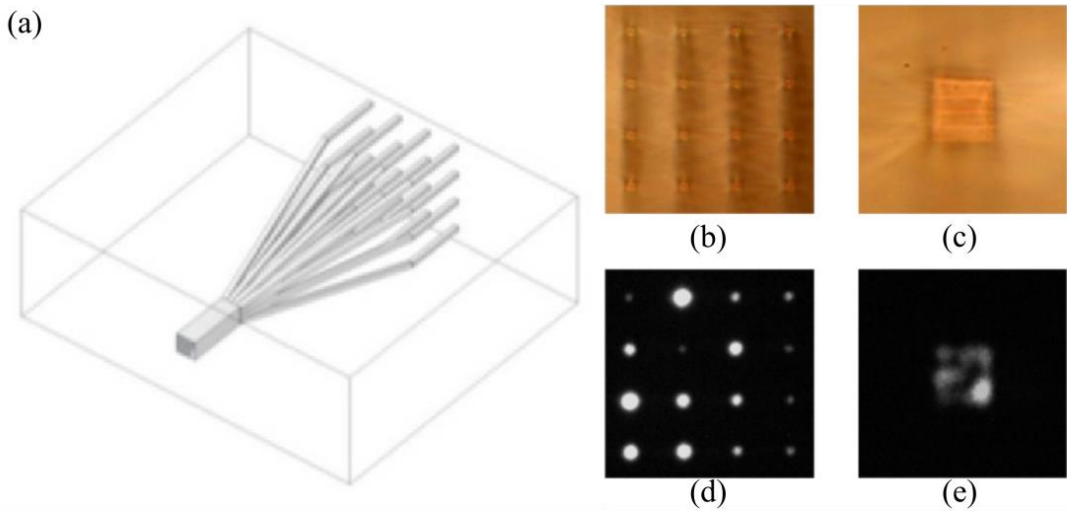

Figure 2-5 – (a) schematic of an integrated photonic lantern with a large square multimode waveguide split into 16 single mode square cores. Optical micrograph images of: (b) single mode array and (c) multimode waveguide of ULI fabricated lantern. Output patterns of: (d) single mode array and (e) multimode core, for 1539 nm light. Field of view, 200 μm square for b & d, and 100 μm square for c & e, image from [7].

2.3 Spectrograph calibration for exoplanet detection

2.3.1 Motivation

Ever since the first confirmed observation of an exoplanet in the 1990's [10], there has been great interest in the discovery and investigation of exoplanets (planets that exist beyond the known solar system) and there are currently over 2000 confirmed planets.

There are a wide variety of exoplanets, from very large gas giants in close orbits around their host star, (so-called "hot Jupiters") to small rocky worlds similar to our own. To detect these planets a variety of techniques may be employed.

Direct imaging of a planet is a highly non-trivial task, given the fact that the parent star is many magnitudes larger and brighter than the planet. The first direct imaging of an exoplanet was a Jupiter mass (M_{Jup}) planet in orbit around a 25 M_{Jup} brown dwarf star [11]. Brown dwarf stars are much smaller and dimmer than a star such as the Sun (~1048 M_{Jup}) and therefore more suited to direct imaging. In 2008, multiple planets were directly imaged orbiting the star HR 8799 (~1.5 M_{sun}) by the Keck and Gemini telescopes [12] (Fig 2.6). The three gas giant planets (3 – 13 M_{Jup}) occupy large orbits and represent a scaled up model of our solar system.

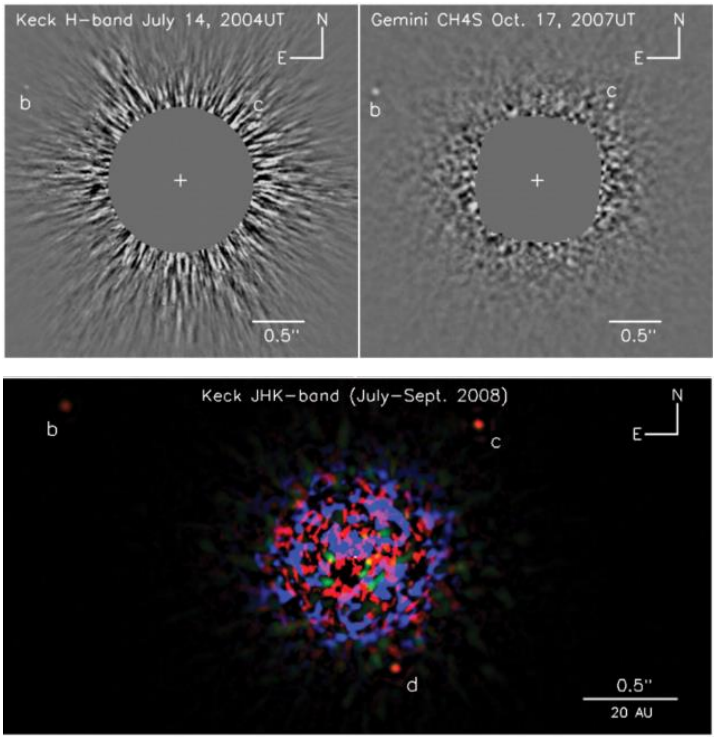

Figure 2-6 – Direct imaging of HR8799bcd with the host star removed by the Keck telescope (Top Left) and Gemini telescope (Top Right). The three identified planets are labelled b, c and d. (Bottom) Colour image of the planetary system obtained by the Keck telescope. The central region is left unmasked, clearly showing the magnitude of noise at d demonstrating that this technique is unsuitable to planets in close orbits. Images from [12].

The transit method of exoplanet detection is more suitable to a greater variety of planet types. The transit technique is rather simple conceptually and relies on the fact that if a planet passes between an observer and its parent star (transits), there will be an observable

reduction in the measured flux from the star (Fig 2.7). The magnitude of this reduction will be dependent on the relative sizes and distances of the planet and star. The first transiting planets were confirmed in 2000 by Henry *et al.* [13] and Chabonneau *et al.* [14]. As would be expected, the observed dip in the stellar brightness is generally very faint, and many false positives are recorded. As a result, the transit technique requires long term observations to confirm the orbital period or an agreement with another detection method. The 0.95 m diameter Kepler space telescope launched by NASA in 2009 uses the transit method to detect exoplanets, and has successfully confirmed over 2300 planets in around 440 different stellar systems, with a further 2300 planetary candidates awaiting confirmation. These discoveries have included 12 planets that are rocky, near Earth in size and occupying the "habitable region" of their parent star (the range over which liquid water can exist), making them a potentially viable site for extra-terrestrial life.

In addition to facilitating the detection of exoplanets, the transit technique also enables information about the exoplanet atmosphere composition to be determined by detecting the changes in the stellar spectrum as the planet transits [15].

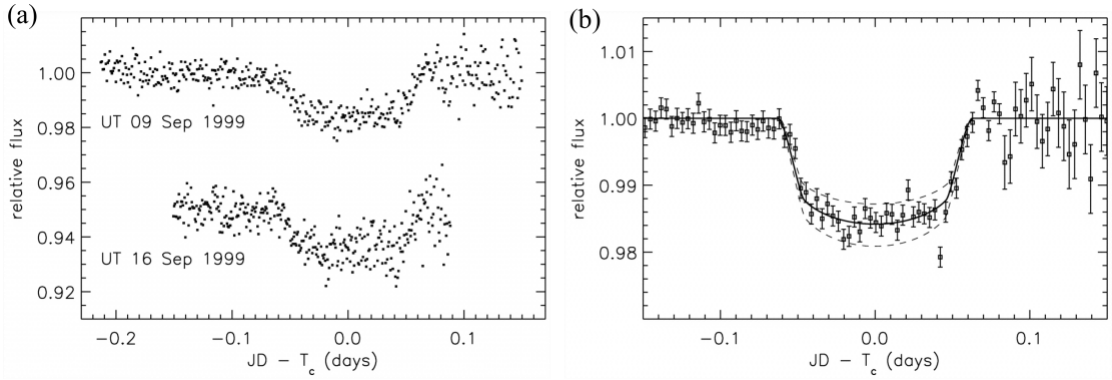

Figure 2-7 – (a) Data from two successive transits of a planetary transit around star HD209458. Data from 16 September offset by – 0.05 for clarity. (b) Binned averaged data, with the solid line indicating the transit of the best fit planet, with the dashed lines indicating transits for planetary radiuses ± 10%. Images from [14].

The radial velocity, or Doppler, method uses the "barycentric wobble" a planet imparts on its stellar host for detection. According to Newton's third law of motion, a planet and its parent star orbit a common centre of mass. As the star moves backwards and forwards relative to an observer, Doppler induced displacements in the well-known elemental spectral absorption lines can be observed in the stellar spectra. Unlike the transit

technique, the Doppler technique enables the mass of the planet to be determined if the plane of the planet's obit is known.

As would be expected, the magnitude of the Doppler shift is dependent on the mass of the planet, its distance from the host star, and the mass of the star. For these reasons, the first planet detected using the radial velocity technique was a large Jupiter-like planet orbiting a solar-type star, consequently imparting a large ~ ± 60 m/s radial velocity shift in the stellar spectrum [16] (Fig. 2.8). For smaller, lighter planets the observed Doppler shift will be greatly reduced. For example, in order to detect an Earth-like planet in the habitable zone around a solar-type star, we expect to observe Doppler shifts as low as 0.05 m/s. In order to measure such a small shift, the spectrograph must be precisely calibrated over long periods.

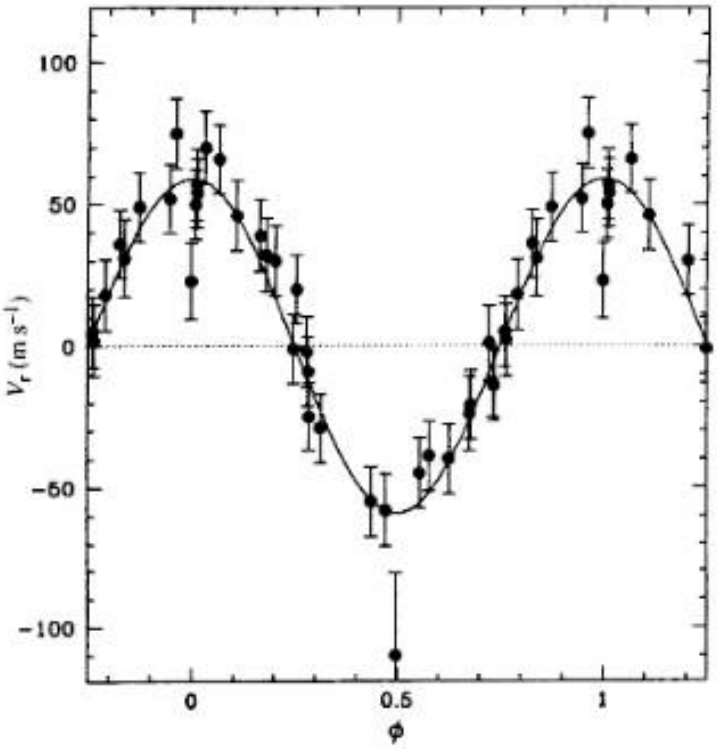

Figure 2-8 – Orbital motion of one of the first discovered exoplanets, with a large Jupiter like planet orbiting the Sun-like star 51 Pegasi orbiting every 4.2 days. Figure from [16].

The ideal calibration source for a planet finding spectrograph would exhibit a number of distinct properties, including [17] [18];

(i) The spectral positions of the calibration lines would be traceable back to fundamental measurement standards.

(ii) The calibration lines would be generated over a broad wavelength range.

(iii) The calibration lines would be well separated from each other spectrally.

(iv) The calibration lines would be spectrally sharp, such that they are unresolved by the spectrograph.

(v) The calibration lines would be sufficiently intense to be clearly identified (e.g. shot noise would be negligible).

(vi) The calibration lines would be of uniform strength.

(vii) The calibration source should be stable over a long period of time (years).

It is also worth noting as an aside that the Doppler technique has further applications outside exoplanet science e.g. detecting the rate of expansion of the universe if the accuracy of the instruments can achieve an absolute prediction 0.01 – 0.1 m/s over several decades [19].

2.3.2 Conventional spectrograph calibration

Conventional astronomical spectrographs traditionally use elemental arc lamps to produce emission spectra for spectrograph calibration. For example, the Intermediate Dispersion Spectrograph at the Isaac Newton Telescope has a range of five different calibration arc lamps available (Copper-Argon, Copper-Neon, Thorium-Argon, Helium, and bi-alkali (Al/Ca/Mg-Neon)). The lamps can either be used alone, or in conjunction with each other to produce a suitable calibration spectra for the wavelength range and grating used [20]. The Thorium-Argon hollow-cathode emission-line lamp is one the most commonly used calibration sources, with a large number of spectral lines covering the wavelength range from 691 to 5804 nm. However, the intensity and spacing of these lines varies greatly and the relative intensity of these lines can vary over time as the current and pressure of the lamp varies as it ages [17].

Gas absorption cells are also used as calibration sources, with the iodine cell being one of the most commonly used. Iodine cells have a reduced wavelength range – typically useful between 500 – 650 nm, and also absorb approximately half of the object light, thereby reducing the signal-to-noise of the system. These I_2 cells have similar downsides to Th-Ar lamps and current work is focused on producing a calibration source that can meet all the desired criteria.

2.3.3 Astrophotonic spectrograph calibration

In 2005 the Nobel Prize in Physics was in part awarded to J. L. Hall and T. W. Hänsch for their work on laser-based precision spectroscopy, and the development of the laser-based optical frequency comb as a tool in precision spectroscopy [21]. A laser-based optical frequency comb is based on a mode-locked laser system, which produces a train of optical pulses at a repetition rate determined by the laser cavity. By transforming this output to the frequency domain, a comb of spectral lines is obtained, where each tooth of the comb is separated from its neighbour by a frequency equal to the pulse repetition frequency. By employing carrier envelope phase locking techniques, a frequency comb can be locked to an atomic clock and the spectral positions of the comb lines are then traceable to an atomic standard.

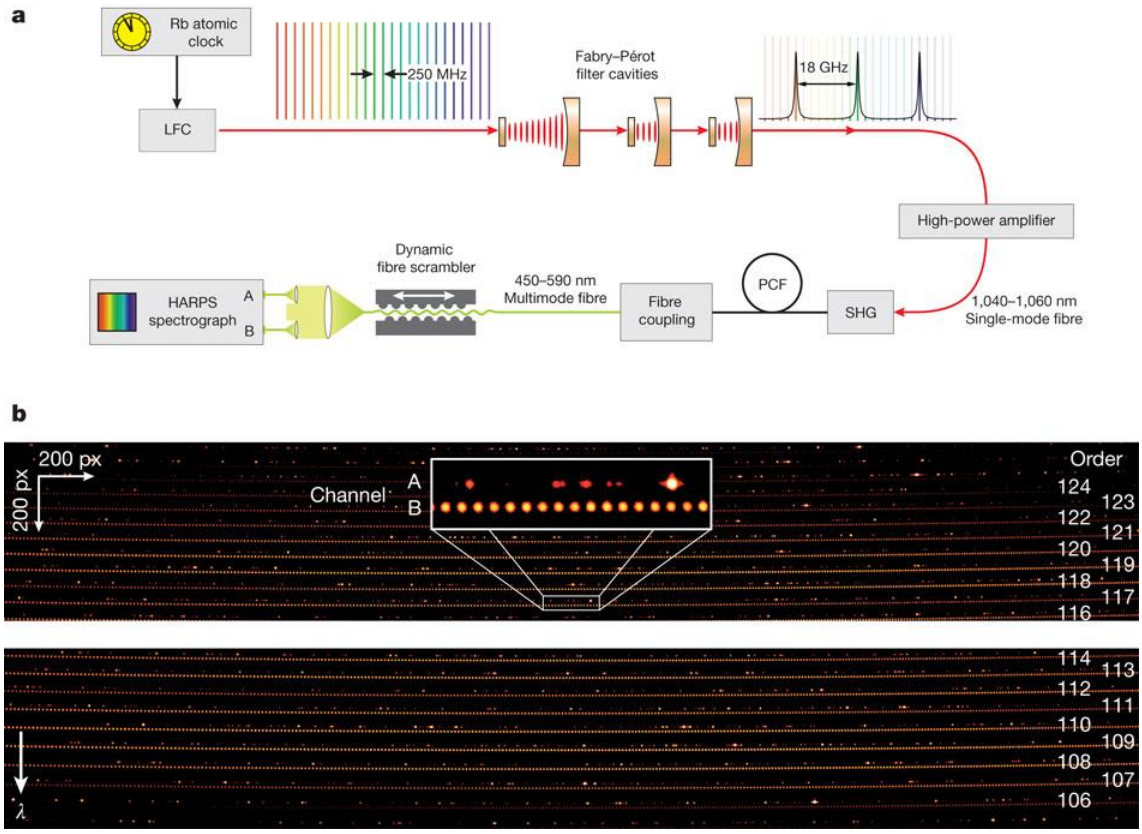

Figure 2-9 – (a) Schematic of the laser frequency comb system used to calibrate the HARPS spectrograph. (b) Raw data of one acquisition with HARPS, Channel A is illuminated by a Thorium spectral lamp, Channel B is illumined by the laser frequency comb, demonstrating the equal spacing and even illumination of the comb teeth. Image from [22].

Laser frequency combs can produce precisely calibrated, evenly spaced lines over a broad optical range with long-term stability, making them of great interest for astronomical

spectrograph calibration [23]. For example, a laser frequency comb calibration system was tested on-sky at the HARPS (High Accuracy Radial velocity Planet Searcher) Spectrograph and could determine Doppler shifts to an uncertainty of 0.025 m/s [22] compared to the 0.1 m/s uncertainty achieved with a Thorium lamp over short timescales (Fig. 2.9).

2.3.4 Future directions

Conventional laser frequency combs are limited to certain wavelengths, and cannot readily generate frequency combs in the mid-infrared wavelength range. Recently, however, it has been demonstrated that optical parametric oscillators (OPOs) can be used to generate a broadly tunable, high repetition femtosecond frequency comb source [24]. Frequency combs generated by an OPO were first developed in 2007 [25], and their subsequent development has produced stabilised combs that cover the mid-infrared and offer a potential application as an astronomical calibration source [26]. Furthermore OPO frequency combs have been developed at high repetition rates (10 GHz), producing short (42 fs) pulses that can be resolved with a simple grating spectrometer [27] - removing the need for the filtering often required with standard laser frequency combs.

It is also worth noting that a variety of other technologies offer possibilities as alternatives to conventional frequency combs. For example, high Q-factor micro-ring resonators can be manufactured from materials such as silicon using e-beam or conventional UV lithography. These resonators generally consist of a simple circular ring waveguide which can be evanescently coupled to a single mode waveguide or fibre [28] (Fig. 2.10). Such components can either be used as high Q-factor filters, for example for selecting specific lines from a laser frequency comb, or as a miniature OPO cavity to generate the calibration frequency comb itself [29]. Another promising alternative to conventional laser frequency astrocombs is to generate a comb via direct modulation of a narrow band CW laser [30].

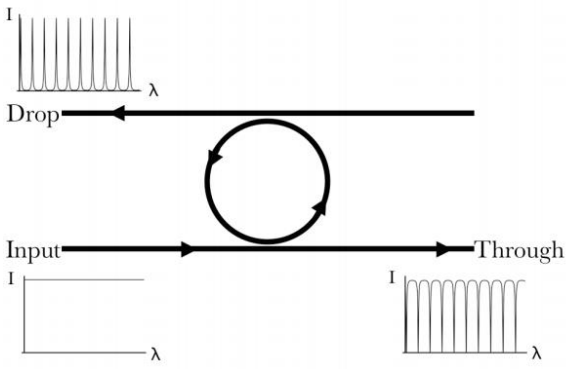

Figure 2-10 – Schematic of a simple ring resonator with a sketch of observed spectrum at each port [29].

2.4 Improving spectrograph stability

2.4.1 Motivation

To achieve the precision required for exoplanet detection the spectrograph must be well stabilised, with minimal variation. There are a number of factors that can limit the precision an instrument can achieve, these include:

2.4.1.1 Spectrograph size

It is an obvious fact that ground based telescopes must observe celestial objects through the Earth's atmosphere. Unfortunately, the atmosphere is highly turbulent, and the celestial light passes through different patches of the atmosphere propagating at different speeds, disrupting the plane waves produced by stars. This effect is responsible for the "twinkling" visually observed in stars, where they appear to vary in intensity over relatively short periods of time. To reduce this effect, telescopes are generally built at high altitudes to reduce the volume of atmosphere that the light must travel through. This does not fully remove the turbulence, however, and large telescopes in particular require adaptive optics (AO) systems to correct for the atmospheric aberrations in quasi-real-time.

We can, in fact, consider the telescope point spread function (PSF) to be formed out of a series of orthogonal spatial modes, the approximate number of which is given by Equation 2.1.

$$N_m \approx \frac{\pi^2}{16}\left(\frac{\theta_{seeing}\, D_T}{\lambda}\right)^2 \qquad \text{(Eq. 2.1)}$$

Where N_m is the number of supported modes, θ_{seeing} is the atmospheric seeing of the site in radians, D_T is the diameter of the telescope aperture, and λ is the wavelength of light [31]. As can clearly be seen from Equation 2.1 the number of modes that form the PSF scales with the square of the telescope diameter. The next generation of extremely large telescopes (ELTs), such as the 30 m TMT (thirty meter telescope) which may be located in Hawaii; the 24.5 m GMT (Giant Magellan Telescope) in Chile and the 39 m E-ELT (European Extremely Large Telescope) located in Chile are now entering the early building stages, with first light expected around 2022 – 2025. According to Equation 2.1, even with the assistance of an AO system, the PSF of an ELT will likely consist of a significantly greater number of modes than the current generation of telescopes. As such, the size and cost of a conventional spectrograph will also significantly increase if the same spectral resolution and throughput requirements remain constant [32]. Larger instruments will also require greater environmental stability with the spectrograph placed in a separate temperature controlled room, usually located in the basement of the observatory, with the light relayed to it via multimode optical fibres.

2.4.1.2 Modal Noise

In comparison to single-mode fibres (SMFs), which usually have core sizes in the region of a few microns, multimode fibres (MMFs) generally larger cores in the region of ~ 50 → 200 μm in diameter. Furthermore, MMFs also generally exhibit larger numerical apertures (NAs) than SMFs. As such, MMFs are able to collect and guide a larger cone of light, which can travel down the fibre in any combination of different ray paths, or modes, each of which exhibits a distinct electric field distribution (Fig. 2.11).

For astronomical instrumentation applications, one end of the MMF is generally placed in the telescope focal plane, and is used to capture light from a specific celestial object (e.g. a star) and transport it to a spectrograph for analysis. As the telescope slews to track the object, the fibre is moved and the image position on the fibre input can shift, exciting different modes in the fibre. This in turn can change the output intensity profile of the fibre, as the relative phases and amplitudes of the fibre modes change. This phenomena, which is known as modal noise, effectively results in an instability in the spectrograph line profile, limiting the spectral resolution and signal to noise ratio achievable. Modal noise is most prevalent in systems operating in the few mode regime, (≤ 100), reducing

in importance as the number of modes supported by the MMF increases, with the worst case being in a system supporting only two modes.

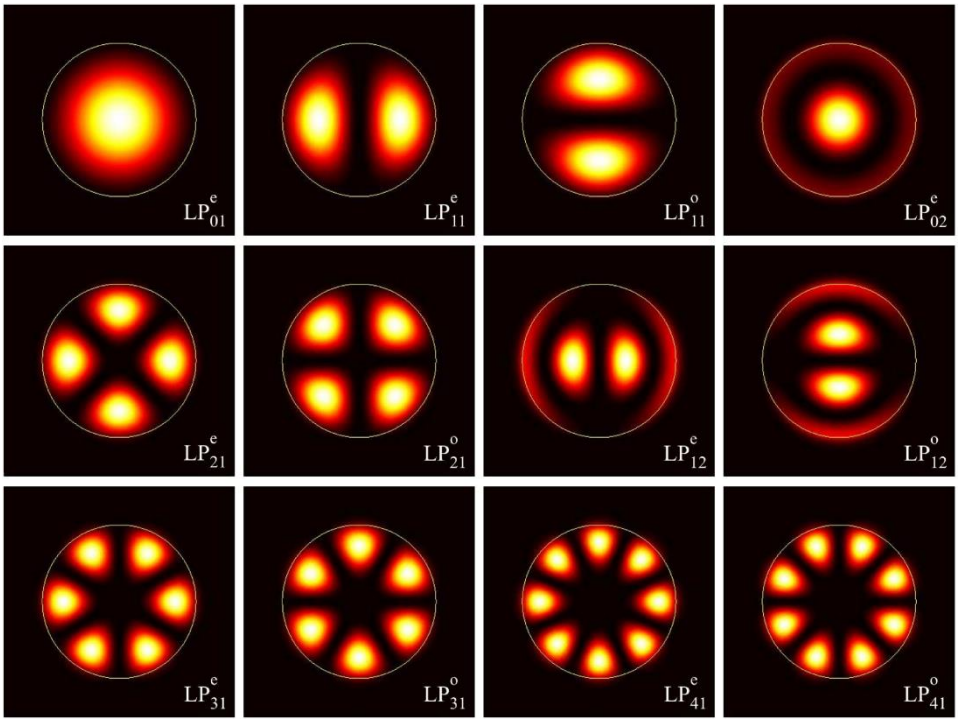

Figure 2-11 – Intensity distribution of fibre modes within a multimode fibre, top left image demonstrates the fundamental mode, a single mode fibre will only support this mode. Image from [33].

Clearly, SMFs only support one transverse mode (one for each orthogonal polarisation state) and spectrographs fed with SMFs should, in principle, exhibit no modal noise. Unfortunately, however, the efficiency of a SMF fibre fed system would usually be too low for astronomical applications, although recent results have demonstrated the use of extreme AO systems on an 8 m class telescope that can efficiently couple the telescope PSF to one SMF with an efficiency of ~ 70% in the H-band [34]. A spectrograph fed with light in such a way could enable extremely precise spectroscopic measurements, but it is yet to be shown that such systems can be applied to ELTs, or at shorter wavelengths, furthermore such extreme AO systems are only suitable for a limited number of targets.

For some current MMF-fed instruments, modal noise does not have a significant effect and can be ignored. One example is the HARPS spectrograph mounted on the 3.6 m European Southern Observatory telescope located in La Silla [35]. This site has an average seeing of 0.75 arcseconds, meaning that the telescope PSF would be formed from ~ 1200 modes at 378 nm and ~360 modes at 691 nm – the spectral range over which HARPS operates. This PSF is fed into a large ~300 μm diameter MMF that supports

thousands of modes whereby the already minimal effect of modal noise can be removed by a simple mechanical agitation mode scrambler.

As already stated, modal noise becomes increasingly problematic as the number of modes excited in the fibre decreases. Examination of Equation 2.1 therefore immediately suggests that even if modal noise is not important at one wavelength (e.g. the visible), it may still be important at a longer wavelength (e.g. the near-IR). This is important for a key science application of relevance to this thesis; of the stars so far investigated by Kepler, it has been reported that an anomalously high proportion of M-Dwarf type stars are orbited by small planets of near-Earth radius. M-Dwarf stars are smaller than the Sun, at around 0.1 to 0.5 solar masses, and as such are cool objects (surface temperatures < 4000K), with the black body emission of the star shifted towards the infra-red. When this fact is combined with the fact that M-Dwarf stars account for ~75 % of the stars in our local galactic neighbourhood, it is obvious why these stars are becoming increasing interesting in the search for small rocky planets orbiting stars in and around the habitable region [36].

GIANO, is a MMF-fed spectrograph designed to operate in the near infrared region, with the goal of investigating cool objects such as M-dwarves. GIANO was previously mounted on the 3.58 m Telescopio Nazionale Galileo located in La Palma, a site with an average seeing of 0.6 arcseconds. With these parameters, the telescope PSF at 0.95 μm would consist of ~ 120 modes, but at 2.5 μm this would drop to just ~ 17 modes. This low number of modes results in a significant contribution from modal noise that restricts the instrument precision. Unfortunately, modal noise has now been identified as a limiting factor in is operation [37]. This effect is so limiting that current plans are underway to remove the fibres from the GIANO and deliver the telescope PSF via free-space optics, which will require significant effort and produce new challenges.

2.4.2. Photonic Integrated Multimode Microspectrograph

One potential astrophotonic solution to both the current scaling of instrument size and modal noise is the photonic integrated multimode microspectrograph (PIMMS) instrument concept. The PIMMS concept, first proposed by Bland-Hawthorn *et al.* in 2010 [38], aims to use photonic concepts to enable a fully integrated spectrograph - the size of which is independent of the telescope aperture. As shown in Fig. 2.12, the PIMMS instrument accepts an input from a MMF, and then uses a photonic lantern to split the

light into several SMFs (see Section 2.2.2). These single modes can then be subject to further operations such as atmospheric filtering (see Section 2.5), but the key to the PIMMS concept is that the SMFs can then be reformatted into a linear array or pseudo-slit that is diffraction limited in one axis, but highly multimode in the orthogonal axis. As such, any modal noise in this output is present as amplitude variations along the slit with no modal noise present across the single-moded axis of the pseudo-slit or linear array. The output array can then be aligned perpendicular to the entrance slit of a spectrograph to provide a diffraction-limited input, in principle, regardless of telescope size.

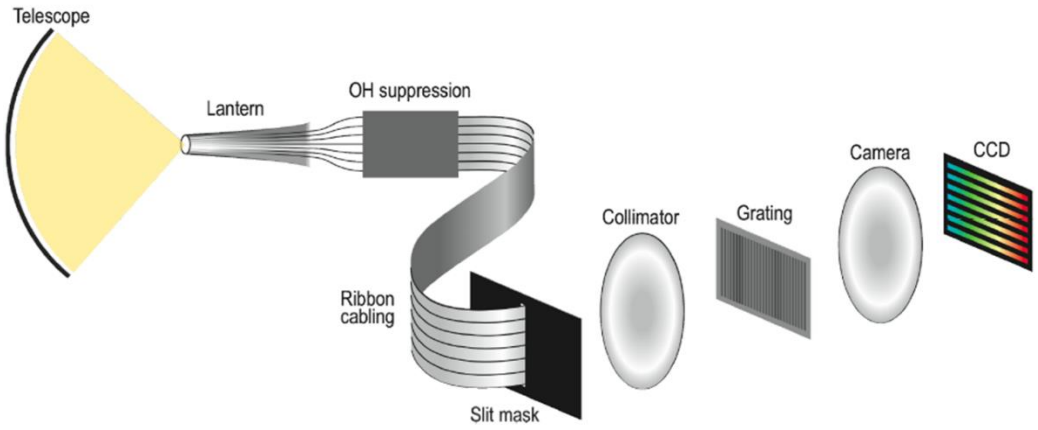

Figure 2-12 – PIMMS instruments concept, a multimode AO corrected telescope PSF is collected by a multimode input, transformed by a photonic lantern transition into an array of single modes where Bragg gratings provide atmospheric filtering. The single modes are rearranged into a linear array and fed into a spectrograph to produce an array of spectra. Figure from [38].

2.4.3 Photonic Mode Scrambling

As previously mentioned, modal noise is mitigated in conventional spectrographs through the use of mode scrambling devices (e.g. shakers). Astrophotonic technologies may also provide a route to enable high efficiency mode scrambling – even in the few-mode regime. These scramblers operate using two photonic lantern transitions back-to-back to create a MM-to-SM-to-MM transition which, when used in conjunction with gentle agitation, produces an output that is highly scrambled regardless of the input illumination [2] (Fig. 2.13). One current issue with this approach is that the current scrambler effectively results in maximal focal ratio degradation (FRD) – where all modes at the output end are equally excited. FRD is, in general, highly undesirable as it increases the size of the instrument beyond that required according to the telescope PSF.

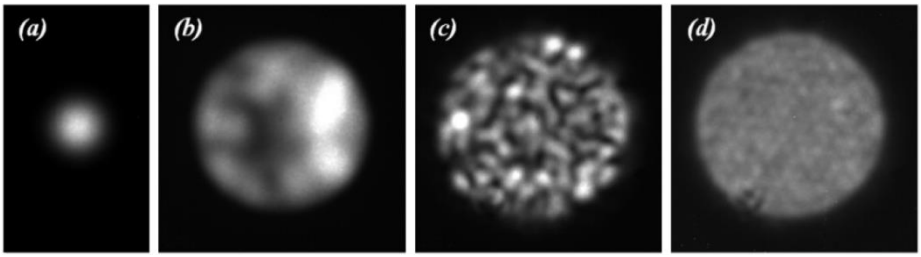

Figure 2-13 – Near field mode images at 1550 nm of: (a) graded-index multimode fibre, favouring the fundamental mode. (b) step-index multimode fibre, (c) multicore fibre photonic lantern showing 'lumpy' modal patterns. The photonic lantern output demonstrates a much higher spatial frequency than the MMF due to enhanced mode mixing in the 120 core lantern. (d) Multimode fibre photonic lantern as in (c) with the fibre gently agitated scrambling all the modes demonstrating an even output pattern. Image from [2].

2.5 Spectral filtering

2.5.1 Motivation

At visible wavelengths, in areas of low population density where light pollution is low, stars are easily visible against a dark background and isolating an optimal signal from a desired target is easy. Unfortunately, as observations move towards the near-infrared wavelength range the night sky is observed to be very bright. This local background originates from the rotation-vibration spectrum of excited hydroxyl radicals (OH) in the atmosphere, which produce a dense "forest" of very bright, very narrow emission lines which can easily swamp the very faint celestial light of interest (Fig. 2.14) – particularly when wishing to perform deep observations of distant galaxies [39]. Thus, it is desirable to have a very high-resolution optical filter that would remove these OH-emission lines, while allowing the faint celestial light of interest to enter the spectrograph.

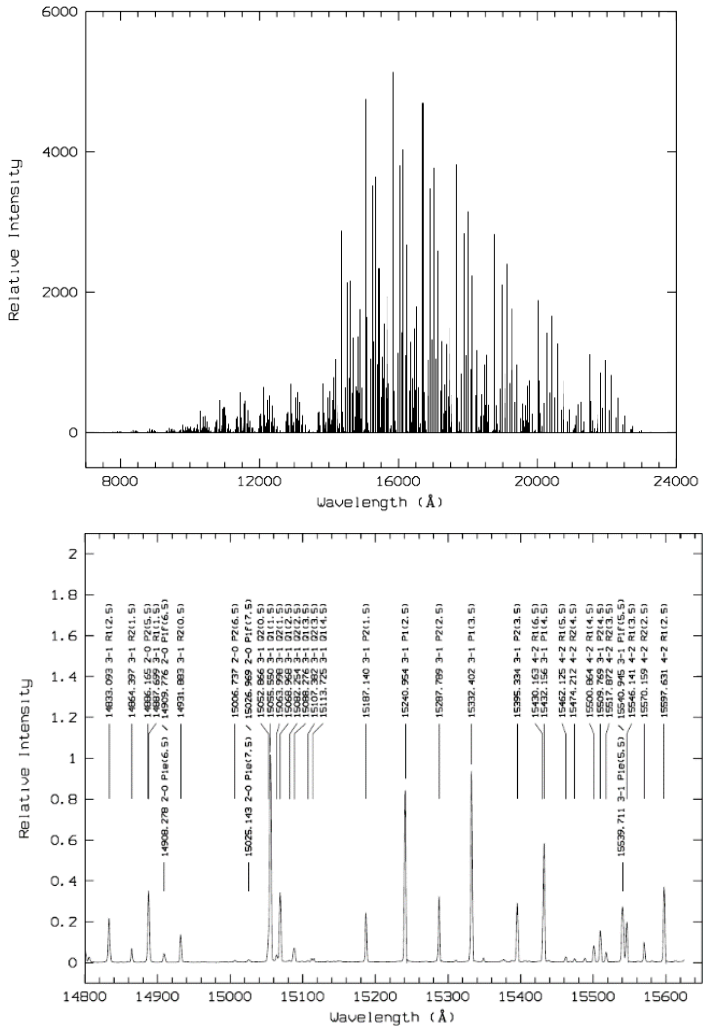

Figure 2-14 – (Top) Theoretical spectrum of the night sky OH emission. (Bottom) Detailed view from 1480 to 1560 nm with key lines identified showing the very intense, narrow nature of these emissions. Figures from [40].

2.5.2 Astrophotonic spectral filters

2.5.2.1 Optical fibre filters

The ideal OH-emission filter would only suppress the OH-emission lines, while allowing the light between the filter lines to pass uninhibited. Due to the large number of emission lines, their aperiodic spacing and varying intensities, the ideal interference filter would be extremely complex. Currently the most viable approach to realising a suitable filter is to use Fibre Bragg Gratings (FBGs) [41] – an SMF that has imprinted on it an extremely complex modulation in refractive index that effective acts as a guided wave version of a thin film interference filter. FBG's can be designed into a SMF which exhibits many >100 aperiodically spaced narrow notches, precisely aligned to specific OH-emission lines. It is important to emphasize that it is essential to use SMFs for this application,

since the different modes in a MMF experience a different grating, thereby degrading the filter response.

The GNOSIS instrument installed at the 3.39 m Anglo-Australian telescope (AAT) has successfully used FBGs to remove over 100 OH doublets over the wavelength range 1.47 – 1.7 μm, before light is injected into the IRIS2 spectrograph [42] (Fig 2.15). The instrument consists of a 1 x 19 photonic lantern, to collect the light from the telescope and couple it into 19 pairs of FBGs for OH-line suppression. This is followed by a 19 x 1 photonic lantern to recouple the SMFs into a MMF as the input to the IRIS2 spectrometer. The first set of FBGs cover the 1.47 – 1.58 μm wavelength region, the second the 1.58 – 1.7 μm region. The FBGs are custom printed in photosensitive fibre, and packaged to maintain temperature stability.

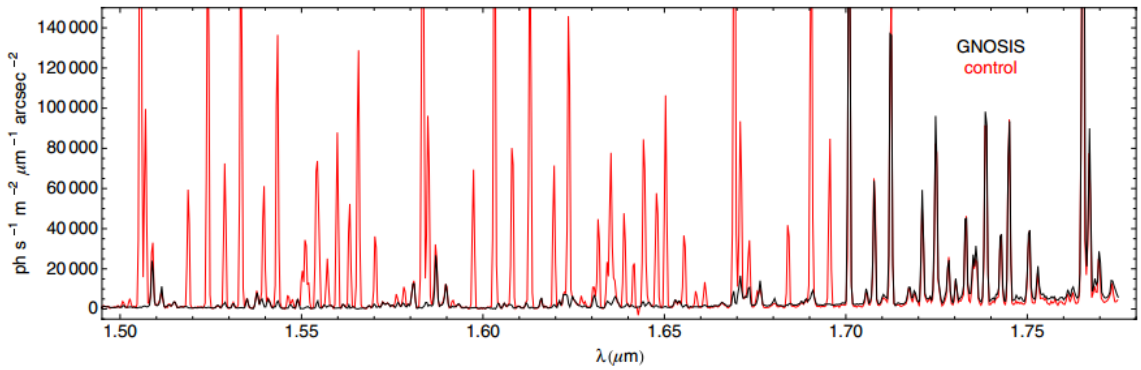

Figure 2-15 – Spectrum of the night sky at the Anglo-Australian telescope: (black) with and (red) without OH suppression. GNOSIS suppresses the 103 brightest OH lines between 1500 and 1700 nm, figure from [42].

A possible improvement to a GNOSIS type device could utilise an MCF-type lantern supporting a large number of modes with the suppression gratings inscribed in all cores of the MCF simultaneously. The practicality of such a grating inscribed in a multicore fibre was investigated by Birks *et al.* in 2012, who performed proof of principle work to inscribe a simplified single notch filter across all 120 cores of a multicore fibre [2] (Fig 2.16). The gratings were inscribed in a similar manner to that used to create gratings in single mode fibre. A photosensitive fibre is exposed to a UV beam, passed through a phase mask grating – a one-dimensional surface relief grating that approximates a square wave pattern, with the zeroth order nulled. In the work by Birks *et al*, a photosensitive fibre was generated by hydrogen-loading the MCF for two weeks to reduce the fabrication threshold for the Ge-doped fibre.

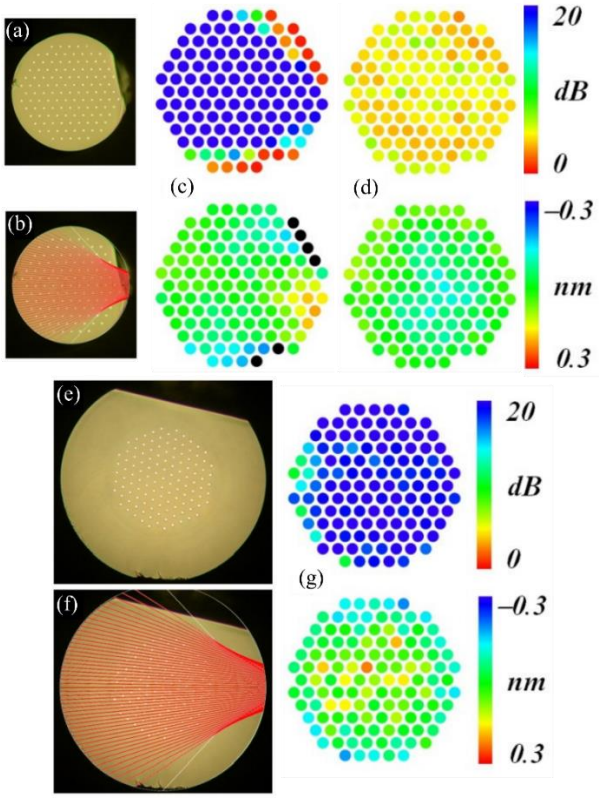

Figure 2-16 – (a) Optical micrograph of 121 core MCF with an outer diameter of 230 μm, (b) image overlaid with ray trace for grating inscription beam, demonstrating some cores are 'missed'. (c) Map of notch depth (top) and offset of notch centre wavelength from the mean (bottom) for fibre a clearly showing the cores with no grating present. (d) repeats (c) with the fibre immersed in index-matching-oil, where notch depth was more even but much reduced due to the UV absorption of the oil. (e) Optical micrograph of 121 core MCF in larger silica jacket with an outer diameter of 400 μm and (f) image overlaid with ray trace. (g) Map of notch depth (top) and centre wavelength (bottom) for the larger fibre demonstrating strong notch depth across all cores, with some left most cores showing a slightly reduced effectiveness due to a shadowing effect. Images from [2].

The work demonstrated that care needs to be taken to ensure all of the cores are subjected to the same grating inscription. In initial tests, the 120 core MCF was simply exposed to the UV beam which expands as it progresses and some of the cores were "missed" with no notch being inscribed within them (Fig. 2.16 c). Due to the extreme brightness of the OH-lines, relative to the signals of interest, even a single missed core will limit the usefulness of the filter. An improvement to this initial attempt was to encase the MCF in a fused silica capillary, effectively increasing the cladding diameter. This ensured the UV light fully overlapped with all the cores and all contained notch grating. However, as shown in Fig. 2.16 (g), it was observed that the notch strength was slightly lower for the further out cores due to a shadowing effect, this contribution will most likely increase as more cores are added.

2.5.2.2 Integrated waveguide filters

It has been demonstrated that while inscribing waveguides using the technique of ULI it is possible to modulate the laser to induce a Bragg grating within the waveguide. Spaleniak *et al.* have recently used this technique to write a three notch grating within a 19 mode integrated photonic lantern [43]. The waveguides were initially inscribed, then overwritten with an electro-optic pulse picker used to modulate the laser and create the Bragg gratings. The three gratings produced an extinction of approximately 5 dB over a 10 mm grating length. Longer gratings produce a greater notch depth, and it was calculated that waveguide gratings ~ 35 mm in length could provide the 20 – 30 dB notch required for atmospheric filtering. With further work demonstrating that complex grating structures can be inscribed it may be possible to produce a ULI device that accepts multimode light, performs OH suppression and reformats the single modes into an array in a single fully integrated device.

2.6 Multi-object spectrographs

2.6.1 Motivation

In order to increase the scientific output of a telescope, spectrographs can be designed to operate with high *multiplex-gains*, where the spectrograph provides spectral information for more than one object at a time. These multi-object-spectrographs (MOS's) operate in conjunction with some type of object selecting instrument. For example, the 2dF multi-object robotic optical fibre positioner can select ~300 individual objects (usually galaxies) for simultaneous analysis at the AAT [44]. The light from these objects is then routed to the basement, using multimode optical fibres, where it is coupled into the entrance slit of the AAOmega spectrograph.

In order to increase the achievable multiplex gains to even higher values than are achieved on instruments such as 2dF, there is a requirement to modularise the spectrographs themselves. One approach is to use the approach of VIRUS [45] – which effectively involves manufacturing ~150 small conventional spectrographs to construct the full instrument. Another approach is to pursue the use of photonic spectrographs, which are, in principle, mass producible.

2.6.2 Arrayed waveguide gratings

Phased array demultiplexers were first proposed in in 1988 by Smit [46], and demonstrated at ~633 nm [47] before being developed for longer telecommunications wavelengths at ~1300 nm [48]. Traditionally Arrayed Waveguide Gratings (AWGs), as they are known, are used to multiplex or de-multiplex a large number of wavelengths, each of which can carry a data signal in one SMF - greatly increasing the data capacity of telecommunications networks. A typical AWG consists of an input multimode waveguide coupled to a free-space propagation region. This feeds the light into an array of curved waveguides with each waveguide having a constant length increment from the previous – the output of this phase array effectively forms a high order diffraction grating. The output from the arrayed waveguides enters a second free propagation region whereby the outputs interfere and are refocused into single mode output waveguides, each supporting a different wavelength (Fig 2.17).

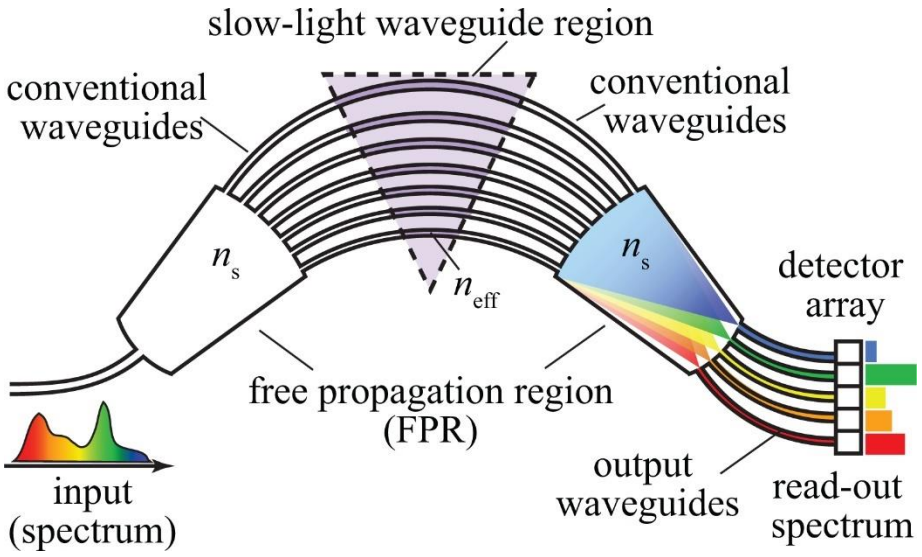

Figure 2-17 – Schematic of an arrayed waveguide grating spectrometer, in this particular case taking advantage of a slow-light section. Image from [49].

In order to be suitable for astronomical applications some adaptations are required to a typical AWG design used for telecommunications. The output waveguides are generally removed and the device polished back to the free propagation zone, so the output spectrum can be directly imaged onto a camera. The input to the AWG can also be altered to accept multiple single mode fibres to increase the resolving power [50]. These principles were applied on-sky in 2012 by Cvetojevic *et al.* to capture the first starlight spectrum with an integrated photonic microspectrograph [51] (Fig. 2.18).

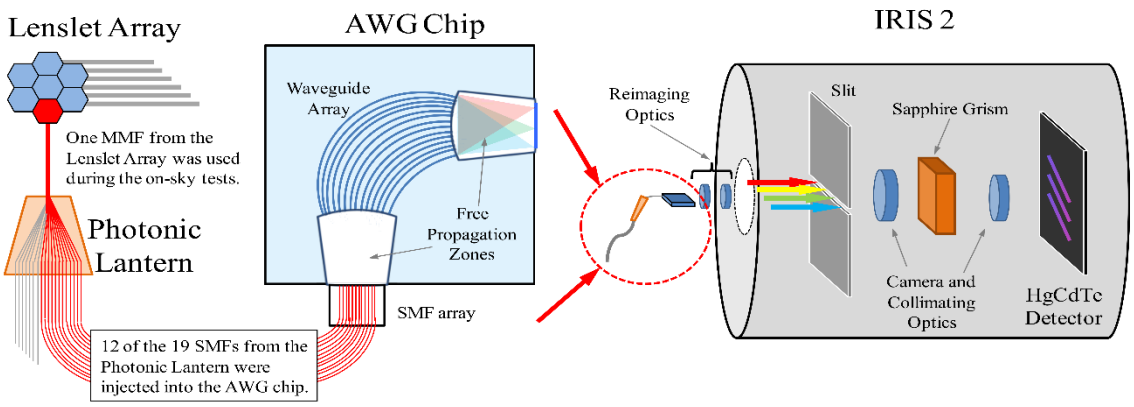

Figure 2-18 – Schematic of the AWG integrated with the IRIS 2 spectrograph used as a cross-disperser. Image from [51].

2.6.3 Stationary Wave Integrated Fourier Transform Spectrometer

An alternative photonic spectrograph is the Stationary Wave Integrated Spectrometer (SWIFTS) concept proposed by Etienne Le Coarer *et al.* [52] (Fig. 2.19). The concept uses a series of nanodetectors to sample the evanescent field of a standing wave interference pattern set up within a single mode waveguide. There are two possible configurations to set up a standing wave within the waveguide. In the first configuration, the SWIFTS-Lippman, the waveguide is terminated by a mirror to reflect back and form a standing wave. In the second configuration, SWIFTS-counter-propagative, the light is split and injected into both sides of the waveguide to set up a standing wave. An optimised SWIFTS devices will require fully optimised nanodetectors, which are still in development. For an initial demonstration of the device nanowires were imprinted across the waveguide to scatter the waveguide light which is subsequently detected.

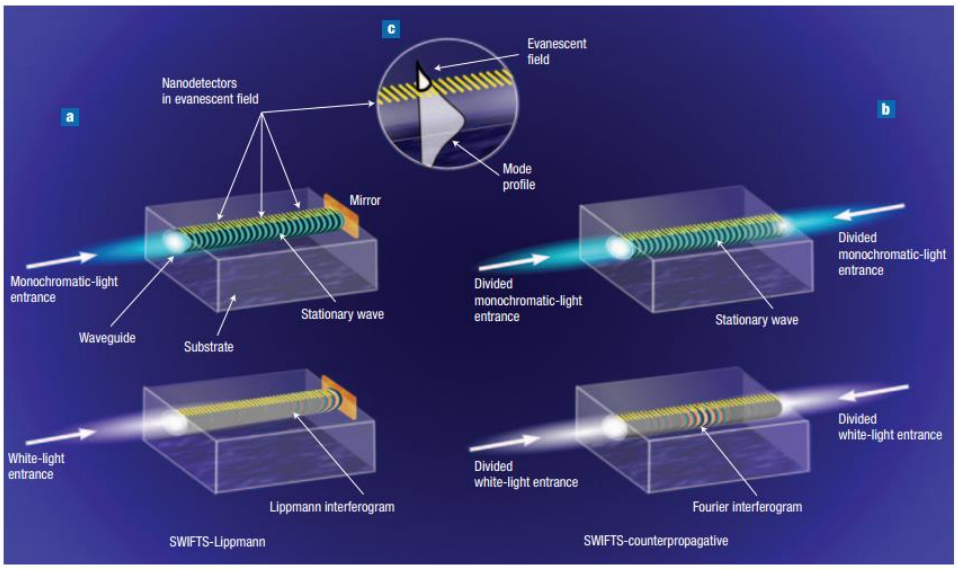

Figure 2-19 – Cartoon of example SWIFTS device; (a) Lippmann configuration, where the signal is reflected back along the waveguide; (b) Counterpropagative configuration, in which the signal is split and injected into opposite ends of the waveguide. (c) Schematic of the nanodetectors sampling the evanescent field to obtain the interferrogram. Image from [52].

2.7 Conclusions

The field of astrophotonics seeks to apply photonic solutions to astronomical applications. The goals of astrophotonics are manifold, including the development of smaller, cheaper and more stable instruments, but the overriding goal of astrophotonics is to enhance the scientific output from the telescope.

Astrophtonics has the potential to impact many areas of astronomical instrumentation, with numerous science goals. One particular area where astrophotonics may have a profound impact is the key questions of whether there is any life on planets outside our solar system. To answer this there is a drive to build larger telescopes that can detect distant worlds, and perform spectroscopy on the planetary atmosphere with sufficient resolution and signal-to-noise to detect biomarkers. Larger telescopes will require large and expensive instruments if they are constructed in the traditional manner of well-established optical technologies, but the advent of astrophotonic technologies may enable more compact instruments using higher quality optics that can be well isolated and stabilised, enabling unprecedented precision. One of the key devices for this is the photonic lantern, which uniquely facilitates the efficient collection of a multimode telescope PSF and efficiently transforms it into a set of single mode systems. Such devices have the potential to enable the removal of background sources of noise via SMF Bragg gratings, and provide an input suitable for a diffraction-limited spectrograph.

These photonic technologies also have the potential to work well with established astronomical techniques. In order to achieve a suitable PSF on the new generation of ELTs ever more complex AO systems will be required. A photonic lantern can efficiently collect multimode light and so reduce the degree of correction required by the AO system, in turn the control of the telescope PSF provided by AO can be used to achieve a perfect match with the integrated device input.

2.8 References

[1] S. G. Leon-Saval, T. A. Birks, J. Bland-Hawthorn, and M. Englund, "Multimode fiber devices with single-mode performance," *Opt. Lett.* **30**, 2545–2547 (2005).

[2] T. A. Birks, B. J. Mangan, A. Díez, J. L. Cruz, and D. F. Murphy, "'Photonic lantern' spectral filters in multi-core fibre," *Opt. Express* **20**, 13996–14008 (2012).

[3] P. S. J. Russell, "Photonic-Crystal Fibers," *J. Light. Technol.* **24**, 4729–4749 (2006).

[4] D. Noordegraaf, P. M. Skovgaard, M. D. Nielsen, and J. Bland-Hawthorn, "Efficient multi-mode to single-mode coupling in a photonic lantern," *Opt. Express* **17**, 1988–1994 (2009).

[5] D. Noordegraaf, P. M. W. Skovgaard, M. D. Maack, J. Bland-Hawthorn, R. Haynes, and J. Lægsgaard, "Multi-mode to single-mode conversion in a 61 port Photonic Lantern," *Opt. Express* **18**, 4673–4678 (2010).

[6] S. G. Leon-Saval, C. H. Betters, and J. Bland-Hawthorn, "The Photonic TIGER: a multicore fiber-fed spectrograph," *Mod. Technol. Space- Ground-based Telesc. Instrum. II. Proc. SPIE* **8450**, 84501K (2012).

[7] R. R. Thomson, T. A. Birks, S. G. Leon-Saval, A. K. Kar, and J. Bland-Hawthorn, "Ultrafast laser inscription of an integrated photonic lantern," *Opt. Express* **19**, 5698–5705 (2011).

[8] A. Arriola, D. Choudhury, and R. R. Thomson, "Towards efficient mid-infrared integrated photonic-lanterns," *J. Opt.* **17**, 125804 (2015).

[9] R. R. Thomson, A. K. Kar, and J. Allington-Smith, "Ultrafast laser inscription: an enabling technology for astrophotonics," *Opt. Express* **17**, 1963–1969 (2009).

[10] A. Wolszczan and D. A. Frail, "A planetary system around the millisecond pulsar PSR1257 + 12," *Nature* **355**, 145–147 (1992).

[11] G. Chauvin, A.-M. Lagrange, C. Dumas, B. Zuckerman, D. Mouillet, I. Song, J.-L. Beuzit, and P. Lowrance, "A giant planet candidate near a young brown dwarf," *A&A* **425**, L29–L32 (2004).

[12] C. Marois, B. Macintosh, T. Barman, B. Zuckerman, I. Song, J. Patience, D. Lafrenière, and R. Doyon, "Direct Imaging of Multiple Planets Orbiting the Star HR 8799," *Science* **322**, 1348–1352 (2008).

[13] G. W. Henry, G. W. Marcy, P. R. Butler, and S. S. Vogt, "A Transiting '51 Peg-like' Planet," *Astrophys. J. Lett.* **529**, L41 (2000).

[14] D. Charbonneau, T. M. Brown, D. W. Latham, and M. Mayor, "Detection of Planetary Transits Across a Sun-like Star," *Astrophys. J. Lett.* **529**, L45 (2000).

[15] D. Charbonneau, T. M. Brown, R. W. Noyes, and R. L. Gilliland, "Detection of an Extrasolar Planet Atmosphere," *Apj* **568**, 377–384 (2002).

[16] M. Mayor and D. Queloz, "A Jupiter-mass companion to a solar-type star," *Nature* **378**, 355–359 (1995).

[17] F. Kerber, G. Nave, C. J. Sansonetti, P. Bristow, A. Rosa, H.-U. Käufl, and M. R. Rosa, "The spectrum of Th-Ar hollow cathode lamps in the 900-4500 nm region: establishing wavelength standards for the calibration of VLT spectrographs," *Ground-based Airborne Instrum. Astron. Proc. SPIE* **6269**, 62692O (2006).

[18] M. T. Murphy, T. Udem, R. Holzwarth, A. Sizmann, L. Pasquini, C. Araujo-Hauck, H. Dekker, S. D'Odorico, M. Fischer, et al., "High-precision wavelength calibration of astronomical spectrographs with laser frequency combs," *Mon. Not. R. Astron. Soc.* **380**, 839–847 (2007).

[19] A. Loeb, "Direct Measurement of Cosmological Parameters from the Cosmic Deceleration of Extragalactic Objects," *Astrophys. J. Lett.* **499**, L111 (1998).

[20] E. J. Zuiderwijk and J. Knapen, "A spectral atlas of calibration lamps in use with the INT IDS," *ING La Palma Tech. Note* **70** (1989).

[21] J. Reichert, R. Holzwarth, T. Udem, and T. W. Hänsch, "Measuring the frequency of light with mode-locked lasers," *Opt. Commun.* **172**, 59–68 (1999).

[22] T. Wilken, G. Lo Curto, R. A. Probst, T. Steinmetz, A. Manescau, L. Pasquini, J. I. Gonzalez Hernandez, R. Rebolo, T. W. Hansch, et al., "A spectrograph for exoplanet observations calibrated at the centimetre-per-second level," *Nature* **485**, 611–614 (2012).

[23] T. Steinmetz, T. Wilken, C. Araujo-Hauck, R. Holzwarth, T. W. Hänsch, L. Pasquini, A. Manescau, S. D'Odorico, M. T. Murphy, et al., "Laser Frequency Combs for Astronomical Observations," *Science* **321**, 1335–1337 (2008).

[24] D. C. Edelstein, E. S. Wachman, and C. L. Tang, "Broadly tunable high repetition rate femtosecond optical parametric oscillator," *Appl. Phys. Lett.* **54**, 1728–1730 (1989).

[25] J. H. Sun, B. J. S. Gale, and D. T. Reid, "Composite frequency comb spanning 0.4-2.4μm from a phase-controlled femtosecond Ti:sapphire laser and synchronously pumped optical parametric oscillator," *Opt. Lett.* **32**, 1414–1416 (2007).

[26] R. A. McCracken and D. T. Reid, "Femtosecond Optical Parametric Oscillator Frequency Combs at Harmonics of the Pump Laser Repetition Frequency," *CLEO 2014*, STh4E.7 (San Jose, California, 2014).

[27] A. Bartels, D. Heinecke, and S. A. Diddams, "Passively mode-locked 10 GHz femtosecond Ti:sapphire laser," *Opt. Lett.* **33**, 1905–1907 (2008).

[28] W. Bogaerts, P. De Heyn, T. Van Vaerenbergh, K. De Vos, S. Kumar Selvaraja, T. Claes, P. Dumon, P. Bienstman, D. Van Thourhout, et al., "Silicon microring resonators," *Laser Photon. Rev.* **6**, 47–73 (2012).

[29] S. C. Ellis, A. Crouzier, J. Bland-Hawthorn, J. S. Lawrence, and J. Kepple, "Potential applications of ring resonators for astronomical instrumentation," *Mod. Technol. Space- Ground-based Telesc. Instrum. II. Proc. SPIE* **8450**, 84501J (2012).

[30] X. Yi, K. Vahala, J. Li, S. Diddams, G. Ycas, P. Plavchan, S. Leifer, J. Sandhu, G. Vasisht, et al., "Demonstration of a near-IR line-referenced electro-optical laser frequency comb for precision radial velocity measurements in astronomy," *Nat. Commun.* **7**, 10436 (2016).

[31] I. Spaleniak, N. Jovanovic, S. Gross, M. J. Ireland, J. S. Lawrence, and M. J. Withford, "Integrated photonic building blocks for next-generation astronomical instrumentation II: the multimode to single mode transition," *Opt. Express* **21**, 27197–27208 (2013).

[32] C. Cunningham, "Future optical technologies for telescopes," *Nat Phot.* **3**, 239–241 (2009).

[33] I. Gómez-Castellanos and R. M. Rodríguez-Dagnino, "Intensity distributions and cutoff frequencies of linearly polarized modes for a step-index elliptical optical fiber," *Opt. Eng.* **46**, 45003–45011 (2007).

[34] N. Jovanovic, N. Cvetojevic, C. Schwab, B. Norris, J. Lozi, S. Gross, C. Betters, G. Singh, O. Guyon, et al., "Efficiently feeding single-mode fiber photonic spectrographs with an extreme adaptive optics system: on-sky characterization and preliminary spectroscopy," *Ground-based Airborne Instrum. Astron. VI. Proc. SPIE* **9908**, 99080R (2016).

[35] M. Mayor, F. Pepe, D. Queloz, F. Bouchy, G. Rupprecht, G. Lo Curto, G. Avila, W. Benz, J.-L. Bertaux, et al., "Setting new standards with HARPS," *Messenger* **114**, 20–24 (2003).

[36] W. J. Borucki, D. G. Koch, G. Basri, N. Batalha, T. M. Brown, S. T. Bryson, D. Caldwell, J. Christensen-Dalsgaard, W. D. Cochran, et al., "Characteristics of Planetary Candidates Observed by Kepler. II. Analysis of the First Four Months of Data," *Astrophys. J.* **736**, 19 (2011).

[37] M. Iuzzolino, A. Tozzi, N. Sanna, L. Zangrilli, and E. Oliva, "Preliminary results on the characterization and performances of ZBLAN fiber for infrared spectrographs," *Ground-based Airborne Instrum. Astron. V Proc. SPIE* **9147**, 914711–914766 (2014).

[38] J. Bland-Hawthorn, J. Lawrence, G. Robertson, S. Campbell, B. Pope, C. Betters, S. Leon-Saval, T. Birks, R. Haynes, et al., "PIMMS: photonic integrated multimode microspectrograph," *Ground-based Airborne Instrum. Astron. III Proc. SPIE* **7735**, 77350N (2010).

[39] A. B. Meinel, "OH emission bands in the spectrum of the night sky," *Astrophys. J.* **111**, 555 (1950).

[40] P. Rousselot, C. Lidman, J.-G. Cuby, G. Moreels, and G. Monnet, "Night-sky spectral atlas of OH emission lines in the near-infrared," *A&A* **354**, 1134 (2000).

[41] A. Othonos, "Fiber Bragg gratings," *Rev. Sci. Instrum.* **68**, 4309 (1997).

[42] C. Q. Trinh, S. C. Ellis, J. Bland-Hawthorn, J. S. Lawrence, A. J. Horton, S. G. Leon-Saval, K. Shortridge, J. Bryant, S. Case, et al., "GNOSIS: The First Instrument to Use Fiber Bragg Gratings for OH Suppression," *Astron. J.* **145**, 51 (2013).

[43] I. Spaleniak, S. Gross, N. Jovanovic, R. J. Williams, J. S. Lawrence, M. J. Ireland, and M. J. Withford, "Multiband processing of multimode light: combining 3D photonic lanterns with waveguide Bragg gratings," *Laser Photon. Rev.* **8**, L1–L5 (2014).

[44] I. J. Lewis, R. D. Cannon, K. Taylor, K. Glazebrook, J. A. Bailey, I. K. Baldry, J. R. Barton, T. J. Bridges, G. B. Dalton, et al., "The Anglo-Australian Observatory 2dF facility," *Mon. Not. R. Astron. Soc.* **333**, 279–298 (2002).

[45] G. J. Hill, S. E. Tuttle, H. Lee, B. L. Vattiat, M. E. Cornell, D. L. DePoy, N. Drory, M. H. Fabricius, A. Kelz, et al., "VIRUS: production of a massively replicated 33k

fiber integral field spectrograph for the upgraded Hobby-Eberly Telescope," *Ground-based Airborne Instrum. Astron. IV. Proc. SPIE* **8446**, 84460N (2012).

[46] M. K. Smit, "New focusing and dispersive planar component based on an optical phased array," *Electron. Lett.* **24**, 385–386 (1988).

[47] A. R. Vellekoop and M. K. Smit, "Low-loss planar optical polarisation splitter with small dimensions," *Electron. Lett.* **25**, 946–947 (1989).

[48] H. Takahashi, S. Suzuki, K. Kato, and I. Nishi, "Arrayed-waveguide grating for wavelength division multi/demultiplexer with nanometre resolution," *Electron. Lett.* **26**, 87–88 (1990).

[49] Z. Shi and R. W. Boyd, "Fundamental limits to slow-light arrayed-waveguide-grating spectrometers," *Opt. Express* **21**, 7793–7798 (2013).

[50] N. Cvetojevic, N. Jovanovic, J. Lawrence, M. Withford, and J. Bland-Hawthorn, "Developing arrayed waveguide grating spectrographs for multi-object astronomical spectroscopy," *Opt. Express* **20**, 2062–2072 (2012).

[51] N. Cvetojevic, N. Jovanovic, C. Betters, J. S. Lawrence, S. C. Ellis, G. Robertson, and J. Bland-Hawthorn, "First starlight spectrum captured using an integrated photonic micro-spectrograph," *A&A* **544**, L1 (2012).

[52] E. le Coarer, S. Blaize, P. Benech, I. Stefanon, A. Morand, G. Lerondel, G. Leblond, P. Kern, J. M. Fedeli, et al., "Wavelength-scale stationary-wave integrated Fourier-transform spectrometry," *Nat Phot.* **1**, 473–478 (2007).

Chapter 3 – Ultrafast laser inscription

3.1 The technology of ultrafast laser inscription

The technique of waveguide fabrication by ultrafast laser inscription (ULI), also called femtosecond laser waveguide writing, was first demonstrated in 1996 by Davis *et al*. [1]. The motivation behind the work was the manufacture of optical devices for use in the telecommunications industry. Previous work in this area concentrated on using UV radiation to induce damage in high-silica glasses, in order to produce optical devices such as Bragg gratings within thin films and optical fibres [2]. Using visible and near infrared laser light to induce damage in glasses had been previously ignored due to the low photon energy of longer wavelength radiation. Driven by the recent development of high-energy density femtosecond pulsed laser systems, which can generate multiphoton absorption effects within the material, the group were able to explore this longer wavelength regime.

The most common solid state ultrafast laser system in use today is the Ti:sapphire (Ti:Al_2O_3) laser system [3] due to its broad tuning range from 670 – 1070 nm and relatively large gain cross-section [4]. The discovery of the Kerr-lens mode locking technique in 1991 produced a 60 fs pulse from a Ti:sapphire laser oscillator [5], and instigated a period of intense research into this platform, eventually resulting in pulse durations of less than 6 fs [6]. The commercial availability of amplified Ti:sapphire systems was key to the discovery by Davis *et al.* that it was possible to create damage lines within a bulk dielectric by translating the material through the focus of train of ultrashort sub-bandgap pulses. Using this approach, the group demonstrated that the modified material exhibited a higher refractive index of 0.035 in Ge-doped fused silica [1].

3.1.1 Material modification

The process of ULI relies on tightly focusing ultrashort sub-bandgap laser pulses inside the bulk of a dielectric material. The laser wavelength is appropriately chosen such that individual photons are insufficient to bridge the energy bandgap of the substrate. As such, under normal conditions, the linear absorption is negligible and the material is transparent to the laser. However, the extremely high peak intensities generated in the focal volume by the tight focussing of ultrashort pulses enable the promotion of electrons across this

bandgap due to nonlinear excitation processes, two such key processes being multi-photon ionisation and tunnelling ionisation.

In tunnelling ionisation, the electron quantum mechanically tunnels through the bandgap to the conduction band (Fig 3.1.a). In multi-photon ionisation several photons are incident upon, and deliver energy to the electron simultaneously and the total energy delivered is enough to overcome the material bandgap (Fig 3.1.b). Once an electron is promoted into the conduction band, the further process of avalanche ionisation becomes a factor, whereby free electrons residing at the bottom of the conduction band can absorb single photons of laser light through phonon-mediated absorption (Joule heating). Once the electron has absorbed sufficient energy, it may impact ionise a second electron residing at the top of the valence band (Fig 3.1.c). These processes create a free-electron plasma in the focal region, which can then transfer its energy to the material lattice on the picosecond and nanosecond timescales. This transfer of energy can result in a variety of structural modifications to the material, such as melting or plasmerisation. Regardless, after the material has cooled, a permanent structural modification can remain which manifests through variations in the properties of the material (e.g. refractive index and chemical etch rate). Away from the focal volume the laser passes through the material with no effect, which leads to the three-dimensional nature of the technique as an arbitrary structure can be created by simply moving the substrate through a stationary focal spot, with the substrate material only affected at the point of focus.

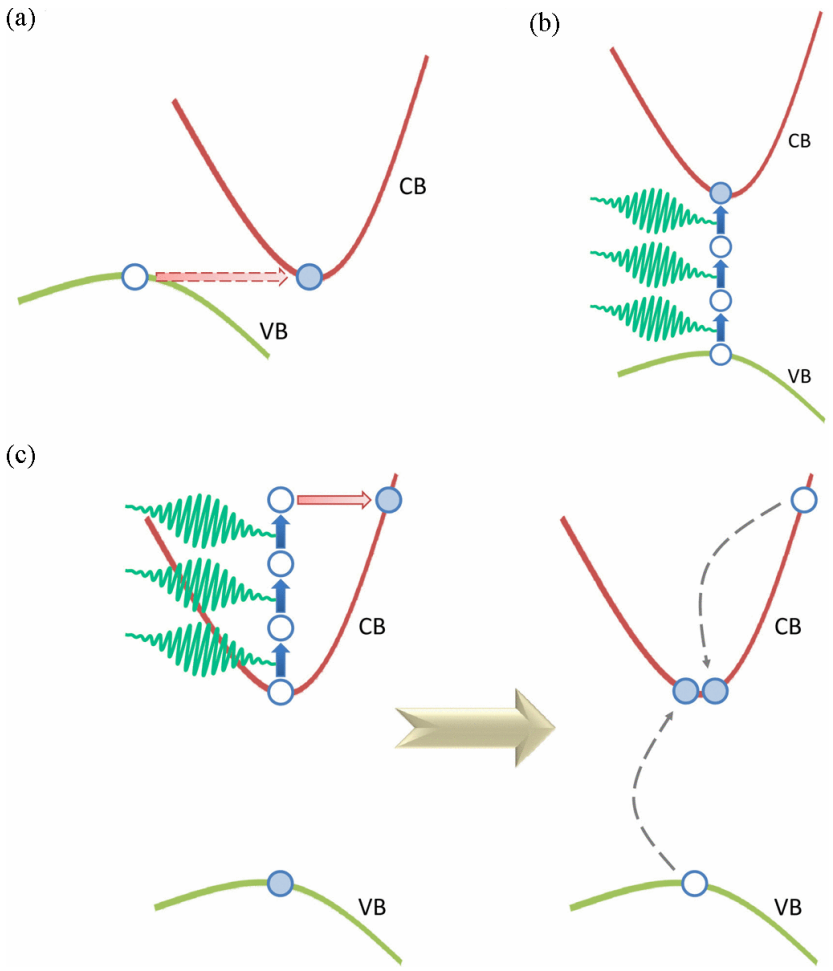

Figure 3-1 – Nonlinear excitation processes used to transfer energy from the laser to the material; (a) tunnelling ionisation, (b) multi-photon ionisation and (c) avalanche ionisation. Image from [7].

Three main material effects at the focal spot are observed as the pulse energy intensity increases. Low pulse energies can result in a smooth refractive index change, which can either be either positive or negative depending on the substrate material. In materials that exhibit a positive refractive index change, generally known as Type I modification (Fig 3.2 top), it is possible to directly fabricate optical waveguides and diffraction gratings within the material. In many crystalline materials it is not possible to generate Type I modification, and instead areas of negative refractive change are produced, Type II modification (Fig 3.2 bottom). In these instances, it is possible to create waveguides by inscribing two parallel damage lines, between which a guided mode can be supported. In general, Type I waveguides exhibit lower propagation losses than Type II waveguides with reported lowest propagation losses of 0.1 and 0.5 dB/cm reported respectively. The cause of this is most likely the existence of highly scattering damage regions in close proximity to the guided mode being present in the Type II case. Medium pulse energies can produce nanogratings within certain materials, which exhibit interesting properties

including form birefringence and lower thermal conductivity. Large pulse energies can produce voids, with microexplosions forcing material out of the focal volume.

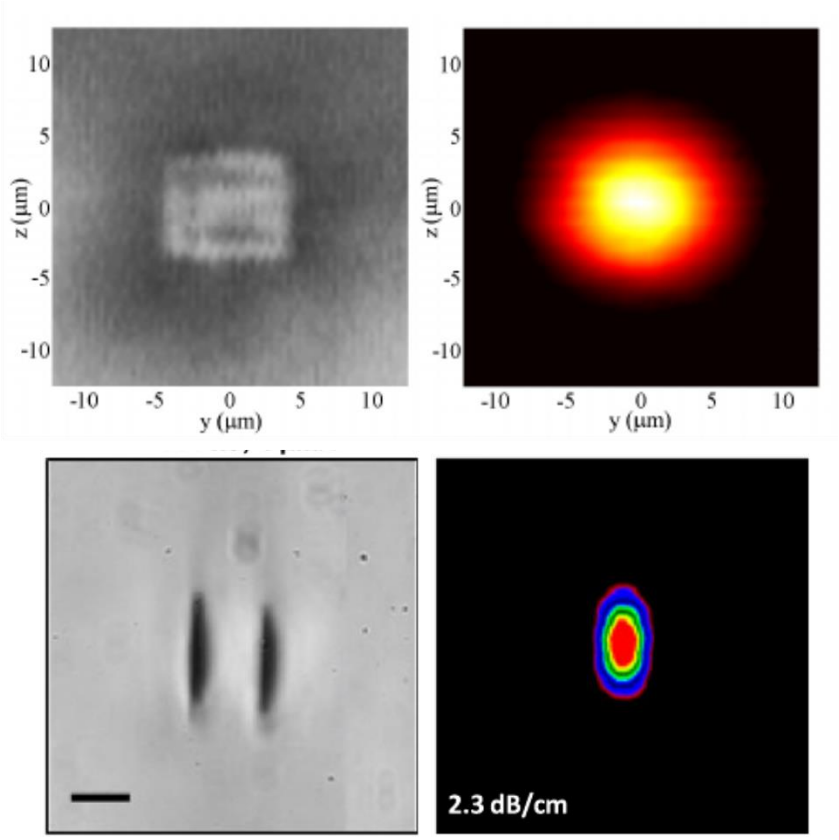

Figure 3-2 – (Top Left) Micrograph of end facet of a Type I optical waveguide, (Top Right) near field image of 1550 nm guided mode supported by the waveguide. Images from [8]. (Bottom Left) Micrograph of Type II damage lines in YAG ceramic, (Bottom Right) near field image of 633 nm guided mode confined by the structure. Scale bar represents 20 μm and corresponds to both images in the bottom row, taken from [9].

The technique of ULI has been demonstrated to work in a variety of materials, such as glasses, both common; fused silica [10], borosilicates [11], aluminosilicates [12], soda-lime glass [13] and more exotic varieties; phosphates [14], flurozirconate [15], bismuth borate [16] and chalcogenide glasses [17][18]. Chalcogenides glasses contain one or more of the chalcogenide elements (Sulphur, Selenium and Tellurium) and may be of particular interest in astronomical applications due to their transmission at near- and mid-infrared wavelengths (~1 – 10 μm). Polymers such as Poly(methyl methacrylate) (PMMA) [19] and CYTOP [20] and crystals such as lithium niobate [21], YAG [22], silicon [23], KTP [24] and sapphire [25] along with many others have also had waveguides inscribed within them via ULI.

An additional capability of ULI that has been observed in certain materials, such as fused silica and Schott *Foturan* photosensitive glass, is a ULI induced increase in the chemical etch rate of the exposed regions [26]. For example, the chemical etch rate of ULI modified fused silica in hydrofluoric (HF) acid has been shown to increase by a factor of around 100. This remarkable capability enables the fabrication of micro-mechanics, micro-fluidics and micro-lenses (Fig 3.3). This work has led to a considerable interest in the biomedical field due to the possibility of fabricating fully integrated lab-on-a-chip devices. After chemical etching, the surface quality of the etched surfaces is unsuitable for certain applications, however an additional post-etch annealing step, either heating the entire substrate or applying a high temperature flame to the etched area, can remove this effect leaving a sub-nm surface roughness.

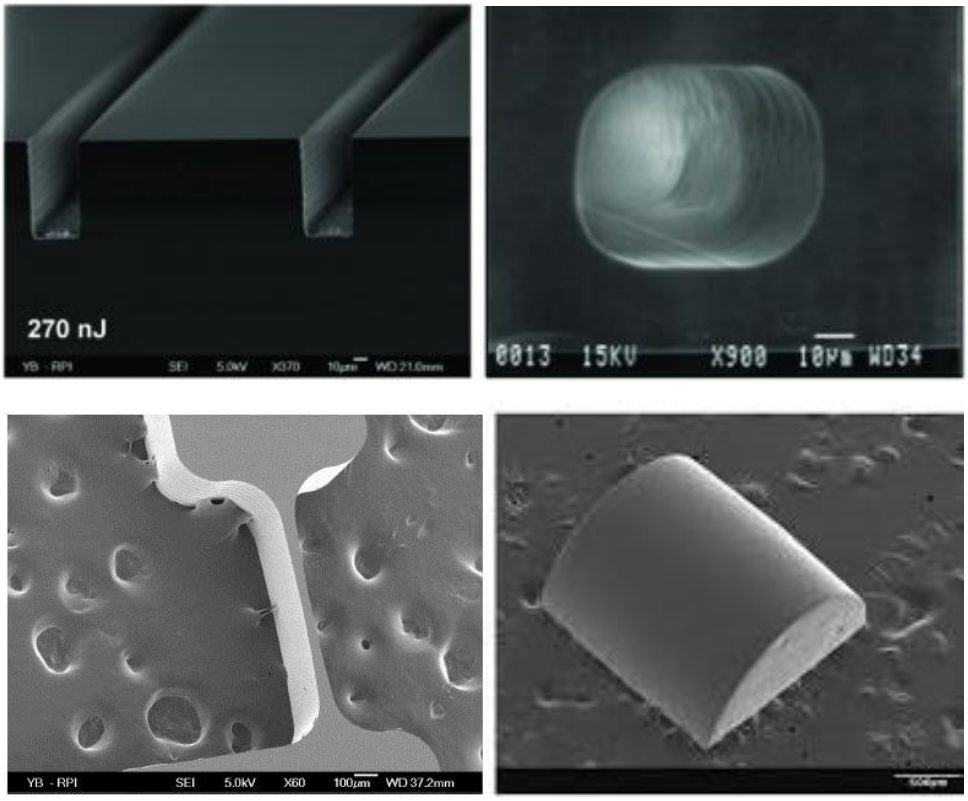

Figure 3-3 – Optical micrographs of: (Top Left) micro-channels, (Top Right) micro-fluidic tunnels, images taken from [27]. (Bottom Left) A micro-hinge, image from [28] and (Bottom Right) a micro-lens with a final smoothing step applied, image from [29], all devices fabricated by ULI and chemical etching.

3.1.2 Basic experimental setup

The basic experimental set-up for ULI (Fig 3.4) incorporates power and polarization control to fine-tune the inscription parameters. A computer controlled shutter is used to control the on-off state of the laser while preserving its stability. The power of the laser

can be adjusted through several methods; directly controlling the laser power, the insertion of absorptive neutral density filters, or the combination of a half waveplate and a polarising beamsplitter cube. A half and quarter waveplate combination allows the polarization of the inscription beam to be defined. Ideally these waveplates are in motorized rotation mounts allowing computer control during the inscription process. The inscription beam can subsequently be directed through a microscope objective and focused within the substrate, which is mounted on a high precision three axis translation stages. A back polished mirror and a camera setup just before the lens enables the back reflection from the substrate surface to be imaged to observe the surface quality and sample orientation.

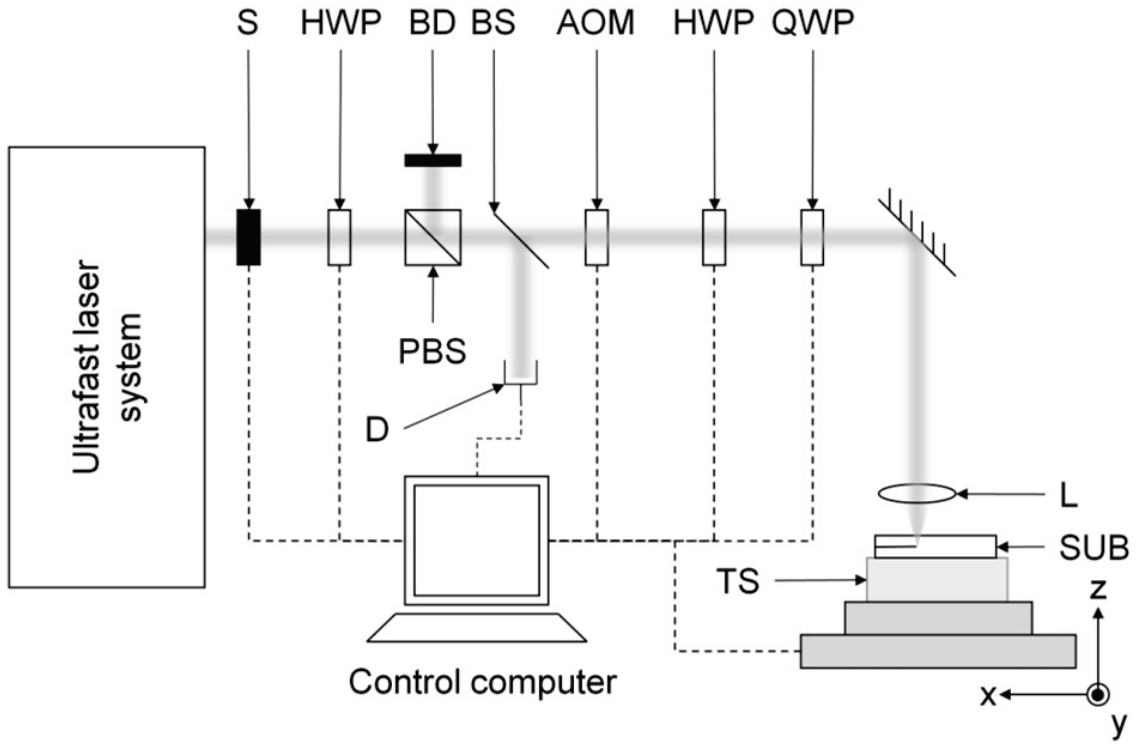

Figure 3-4 – Schematic of a basic ULI setup with an ultrafast laser, and a shutter to switch the beam on and off (S). A half waveplate (HWP) and polarising beamsplitter (PBS) control the pulse energy with a beam dump (BD) to safely absorb excess power. A beamsplitter (BS) reflects a fraction of the beam onto a detector (D) to monitor and set the pulse energy. An acoustic optic modulator is an optional component if additional control of the beam is required. The half waveplate (HWP) and quarter waveplate (QWP) enable control of the polarisation. A lens (L) focuses the beam within the substrate (S), which is mounted on three-dimensional translation stages (TS). A computer allows control of the stages, waveplates and shutter enabling automated control of the system.

3.2 The importance and role of ULI parameters

Through adjustment and control of the system parameters, the desired structure and modification of a substrate can be achieved. Some parameters, such as the wavelength of light, pulse duration, and repetition rate of the delivered pulses are determined by the ultrafast laser used and as such there may be less control over these for a given system. The focusing objective, pulse energy, translation speed and substrate material also play a significant role in ULI and these parameters are more easily adjusted and fine-tuned to produce the desired effect.

In general, the optimum fabrication parameters for a desired structure are most commonly determined by an iterative process, whereby many structures are written using a range of parameters. These structures are then tested and refined for an increasingly fine-tuned parameter space to hone in on the ideal parameters. For more complex structures, it is common to start by determining optimal parameters for a simple structure, e.g. a straight, single mode waveguide, and then progress to forming and testing the desired complex device. The starting parameters for this iterative process are most often determined based on previous knowledge and experience. Alternatively, limits can be determined, such as a minimum pulse energy, below which no modification occurs and a maximum pulse energy, above which the substrate is damaged and used to define an investigation window.

3.2.1 Writing Geometry

There are two main ULI geometries, transverse and longitudinal. For the longitudinal geometry, the substrate is translated in the same direction as the propagation of the inscription beam (Fig 3.5 a). This regime produces a symmetric circular cross-section, however the length of any waveguides is restricted by the working distance of the lens. Many aspheric and microscope objectives used for ULI have relatively short working distances, between 1 and 30 mm, which can limit the device lengths possible. In addition, the modification imparted to the sample demonstrates a depth dependence due to spherical aberrations induced at the sample surface, as such the inscription parameters required to induce a desired effect varies with depth within the sample. These limitations have prevented much investigation in this geometry, as the arbitrary path length and three-dimensional nature of the structures achievable with ULI are the primary benefit of this fabrication technique.

The alternative writing geometry is the transverse inscription geometry, where the sample is moved perpendicular to the direction of propagation of the inscription beam (Fig 3.5 b). In this set-up the waveguide depth can remain constant, with the waveguide length only limited by the size of the substrate and range of motion of the stages. The downside of the transverse geometry is that the cross-section of the inscribed waveguides can be highly asymmetric, determined by the inscription lens used and described in more detail in the following Section. This effect can be undesirable in creating certain structures. In order to produce symmetric waveguides in this geometry additional waveguide shaping techniques may be required.

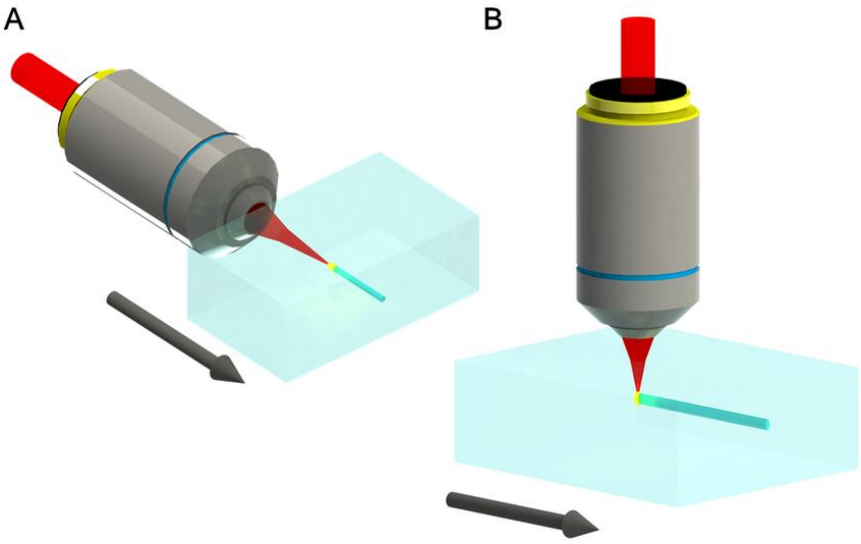

Figure 3-5 – Cartoon of; (a) the longitudinal and (b) transverse inscription geometry of ULI. Arrow indicates sample translation direction. Image from [30].

3.2.2 Inscription lens

The physical properties of the inscription lens determine the spatial distribution of the photo-induced plasma, and hence the shape and size of the modified region within the material. In the longitudinal writing geometry, the cross-section of the modification is symmetrically circular with its size determined by the beam waist diameter of the focused beam. The beam waist diameter (D) is defined as:

$$D = 2\,\omega_0 = \frac{2\,\lambda}{\pi\,NA} \qquad \text{(Eq. 3.1)}$$

Where ω_0 is the beam waist radius, λ is the wavelength of light, NA is the numerical aperture, or acceptance angle of the inscription lens defined as: $NA = n * \sin\theta$, where n is the refractive index and θ is the half angle of the cone of light that can enter the lens.

The larger the NA, the smaller the beam waist and the more tightly focused the focal spot. Most commonly used aspheric and microscope objectives have a diameter of a few mm's meaning, in general, a larger NA lens has a shorter focal length and hence a greater restriction when used in the longitudinal writing geometry.

For the transverse inscription geometry the extent of the modified material along the laser beam axis is defined by the confocal parameter of the lens (*b*):

$$b = \frac{2\,\pi\,n\,\omega_0^2}{\lambda} \qquad \text{(Eq. 3.2)}$$

Where *n* is the refractive index of the material and *b* is the confocal parameter, or twice the Rayleigh range, where the beam width is $\sqrt{2}$ larger than at its waist. The confocal parameter is, in general, much larger than the beam waist and as such the profile of modification is commonly highly asymmetric.

In order to gain more control over the cross-section and obtain a symmetrical region of modification, additional measures must be taken to shape the modified region and will be discussed in Section 3.3. The above equations hold true if spherical aberrations induced by the sample surface are disregarded, however in reality they must be taken into account as they induce a depth dependence to the modification shape.

3.2.3 Laser wavelength

In order to induce localised nonlinear absorption of the laser radiation, rather than linear absorption, the laser wavelength used must be such that the energy of a single photon is less than the bandgap energy of the substrate material, and as such will not be absorbed by the material. Generally speaking, the laser wavelength is not a readily adjustable parameter, although one can use frequency conversion techniques (e.g. second harmonic generation) to adjust the wavelength if required. For example, Nejadmalayeri *et al.* used such a technique in order to perform ULI in crystalline silicon with an 810 nm Ti:sapphire laser by shifting the wavelength to 2400 nm [23]. Frequency conversion has also been used to this effect with Shah *et al.* frequency doubling 1045 nm light generated from a Yb-doped fibre laser to 522 nm for inscription of waveguides in fused silica [31]. The waveguides written at 522 nm performed significantly better than those at 1045 nm.

3.2.4 Laser repetition frequency

The laser repetition frequency is of key importance to the process of ULI as it determines the modification regime in which the technique occurs. The heat deposited by an ultrashort laser pulse within the focal region of a substrate diffuses of the focal volume on the ~μs timescale. Thus, if the repetition rate of the laser is below ~1 MHz, the heat of the previous pulse has fully dissipated by the time the next pulse arrives. At repetition rates greater than ~1 MHz, heat is still present in the focal plane as the next pulse occurs and the heat accumulates within the focal region. This thermal accumulation regime allows the temperature within the focal region to be increased significantly above that achieved with lower repetition rates. As such, higher repetition rates allow larger regions of modification (Fig 3.6).

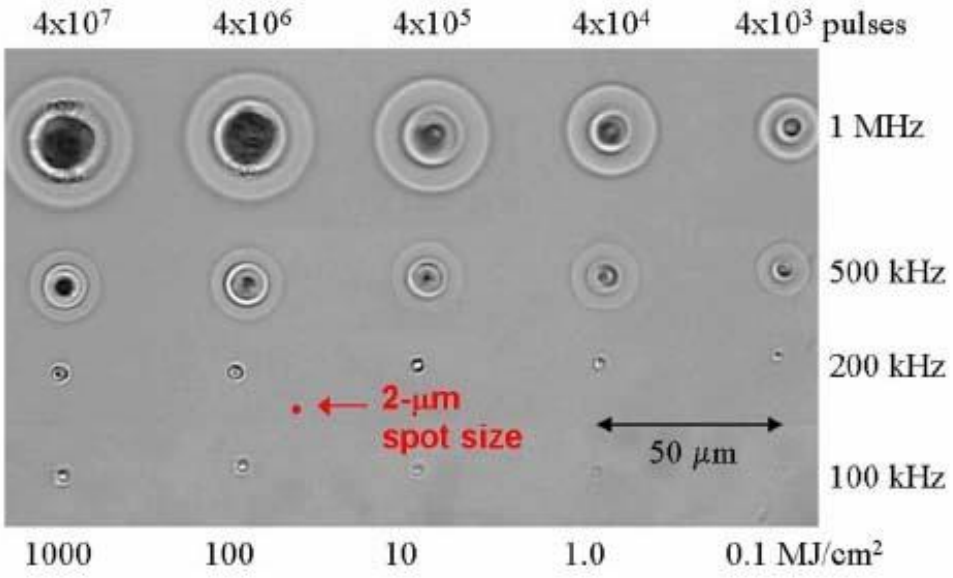

Figure 3-6 – Optical micrograph of heat affected zones in AF45 borosilicate glass using 450 nJ pulses from a 1045 nm femtosecond laser for a variety of repetition rates (Rows) and total pulses (Columns). Image from [32].

3.2.5 Pulse energy

The pulse energy is one of the most critical and easily controllable ULI parameters, determining the energy deposited at the focal region by each incident pulse. Three main material effects at the focal spot are observed as the pulse energy intensity increases. Low pulse energies result in a smooth refractive index change. Medium pulse energies may

induce structures such as nanogratings. Large pulse energies produce voids, with microexplosions forcing material out of the focal volume.

3.2.6 Substrate translation velocity

Varying the substrate translation velocity allows the energy deposited within an area of the substrate to be controlled while keeping the modification regime constant. This is one of the most easily adjustable parameters and can be changed during the writing process allowing a single waveguide to have different properties along its length if required. For certain applications, a slower speed and lower pulse energy can produce low-loss waveguides, however the overall time taken to write a complex structure can also become an important consideration. If a device is designed to be mass manufactured, then the process should not take too long and should be repeatable. The laboratory conditions thus have a significant effect on the process if the temperature stability of the laboratory or the laser stability varies over time. The temperature is often critical, as changes in the laboratory temperature can cause expansion or contraction of the sample or its mounting block causing variations of the focal position within the substrate. Due to this, the translation speed is often defined early in the design process to set how long a particular device will take to fabricate. Other inscription parameters are then set to produce the best results at the desired translation speed.

3.2.7 Beam Polarisation

The effect of the polarisation of the inscription beam has been investigated with Ams *et al.* writing waveguides in fused silica with linearly and circularly polarised light [10]. For linearly polarised light two regimes were tested; light polarised parallel to, and perpendicular to the translation direction of the substrate. The insertion loss of waveguides written with circularly polarised light was found to be significantly reduced compared to those fabricated using linearly polarised light. The reason for the increased transmission is still under investigation, with one proposed explanation being the modification of the periodic nanostructures aligned to the polarisation of a linearly polarised beam. This effect is of particular importance for applications taking advantage of the preferential selective etching of ULI demonstrating a significant correspondence between the polarisation direction and the chemical etch rate [33] (Fig 3.7).

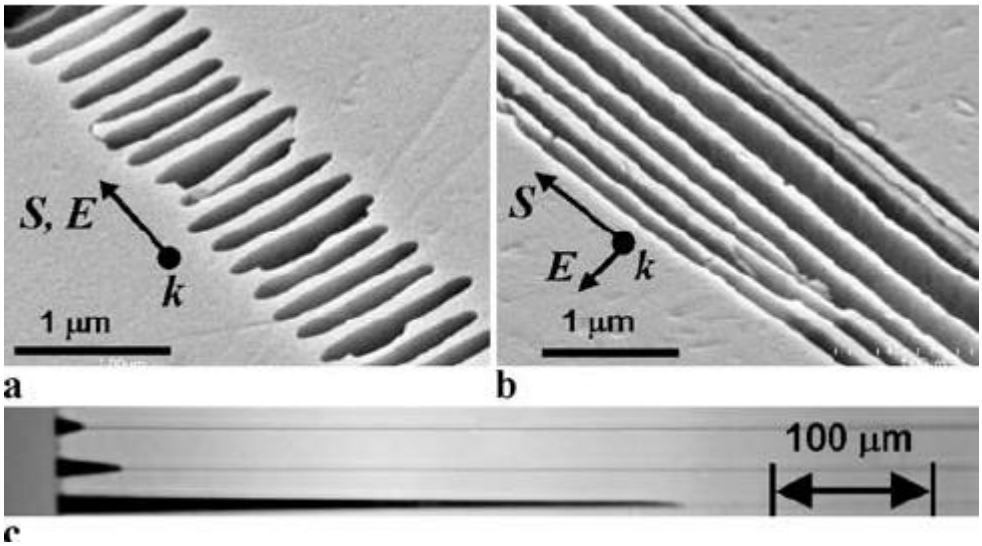

Figure 3-7 – Scanning electron microscope images of ULI fabricated etched channels in fused silica, with linear polarisation (a) parallel to and (b) perpendicular to, the writing direction. (c) Images of channels etched for 480 min 2.5 % HF solution, with the top channel corresponding to the polarisation in (a), middle channel, the polarisation at 45 degrees to the electric field and the bottom channel corresponding to the polarisation in (b). Image from [33].

3.3 Waveguide shaping techniques

As stated previously, when the transverse inscription geometry is used the focal spot is highly asymmetric. If the waveguide is to have a low propagation loss and low coupling loss to a single mode fibre, a symmetric cross-section is required. In addition, asymmetric waveguides can exhibit polarisation dependent guiding losses. By writing at a higher repetition rate and exploiting the thermal accumulation regime it is possible to achieve a more symmetric cross-section, however if it is desired to write with a lower repetition rate more complex beam and/or waveguide shaping techniques are required, a variety of which are described below.

3.3.1 Astigmatic beam shaping

This technique was first demonstrated by Cerullo *et al.* [14] and further investigated by Osellame *et al.* [34]. In this technique a cylindrical telescope is placed before the focussing objective, which can reduce the effective Rayleigh range of the focussed beam, and hence the height of the focal spot (Fig 3.8). This allows the height and width of the focal region to be decoupled and both can be tuned and adjusted allowing an almost symmetric cross-section to be achieved. Symmetric waveguides have been successfully

inscribed in Er:Yb-doped glass and fused silica, however the advent of simpler techniques have superseded this approach. One of the main downsides of the astigmatic beam shaping technique is the addition of extra lenses, which can induce more loss and aberrations as well as significantly complicating the alignment process.

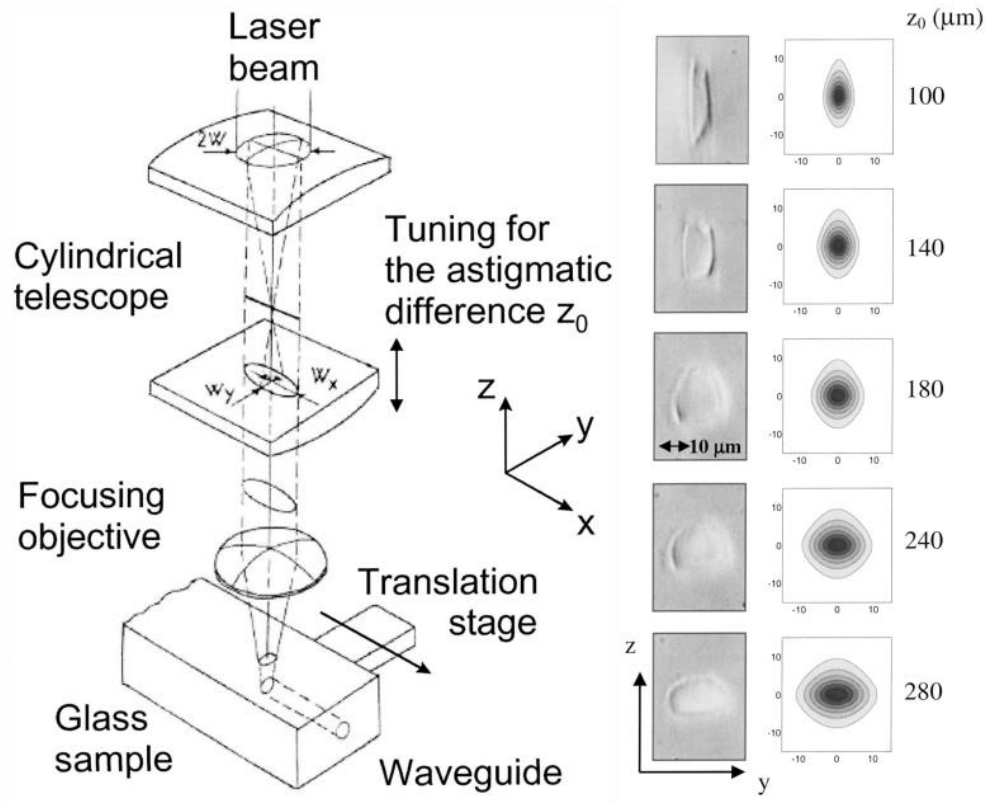

Figure 3-8 – (Left) Schematic of the waveguide inscription setup. (Middle) Optical micrographs of waveguide facets written with an astigmatic beam for increasing values of astigmatic difference. (Right) Simulated electron density profiles. Image from [34].

3.3.2 Slit beam shaping

A more simplified approach to decouple control of the beam height and width is the slit beam shaping technique whereby a slit, oriented along the translation direction of the sample, is placed before the focussing lens. This causes the lens to be under-filled in one axis, thus producing a different effective NA in the two axes (Fig 3.9). The beam waist ratio can then easily be controlled by simply adjusting the slit width. This technique was first demonstrated by Cheng *et al.* [35] before being applied to fabricate waveguides by Ams *et al.* [36]. One possible limitation of this technique is the loss induced by the slit limiting the intensity at the focal volume. A more significant limitation is that it only allows for control of the beam waist in one axis and if the waveguide is sufficiently curved

the cross-section will no longer remain symmetrical. Nevertheless this relatively simple technique has been extensively used by several groups in a variety of materials.

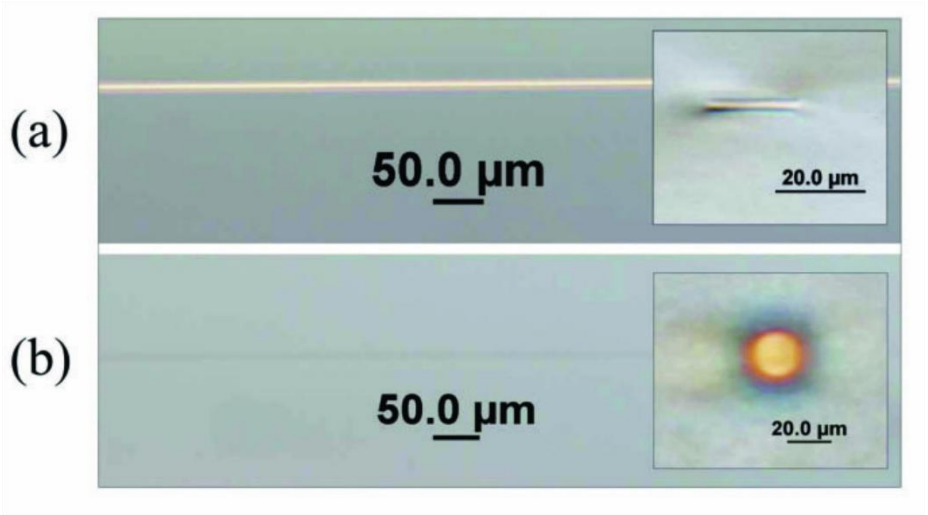

Figure 3-9 – Microscope images of waveguides fabricated in phosphate: (a) without a slit and (b) with a slit, demonstrating a symmetric waveguide. Image from [36].

3.3.3 Active optics

The use of active optics allows a similar approach to that of the previous two techniques to be applied, the reshaping of the beam before the focussing optic, while addressing the major limitation of both of these techniques. Namely, the flexibility of these methods, such that the cross-section cannot easily be changed during the inscription of a waveguide, or to accommodate a significant bend or curve. An active optic such as a deformable mirror or spatial light modulator can be used to shape the beam before the inscription lens and via computer control can adjust this during inscription to accommodate bends or a varying size as desired (Fig 3.10). This approach was first demonstrated with a deformable mirror by Thomson *et al.* using it to simulate a slit as in the slit shaping technique previously discussed to fabricate waveguides in soda-lime glass [37]. The use of active optic beam shaping was further developed by de la Cruz *et al.* who used a spatial light modulator to create an ellipse prior to the inscription beam to create a symmetric waveguide in phosphate glass [38]. These techniques however have the drawback of being quite complex and expensive to integrate into a system.

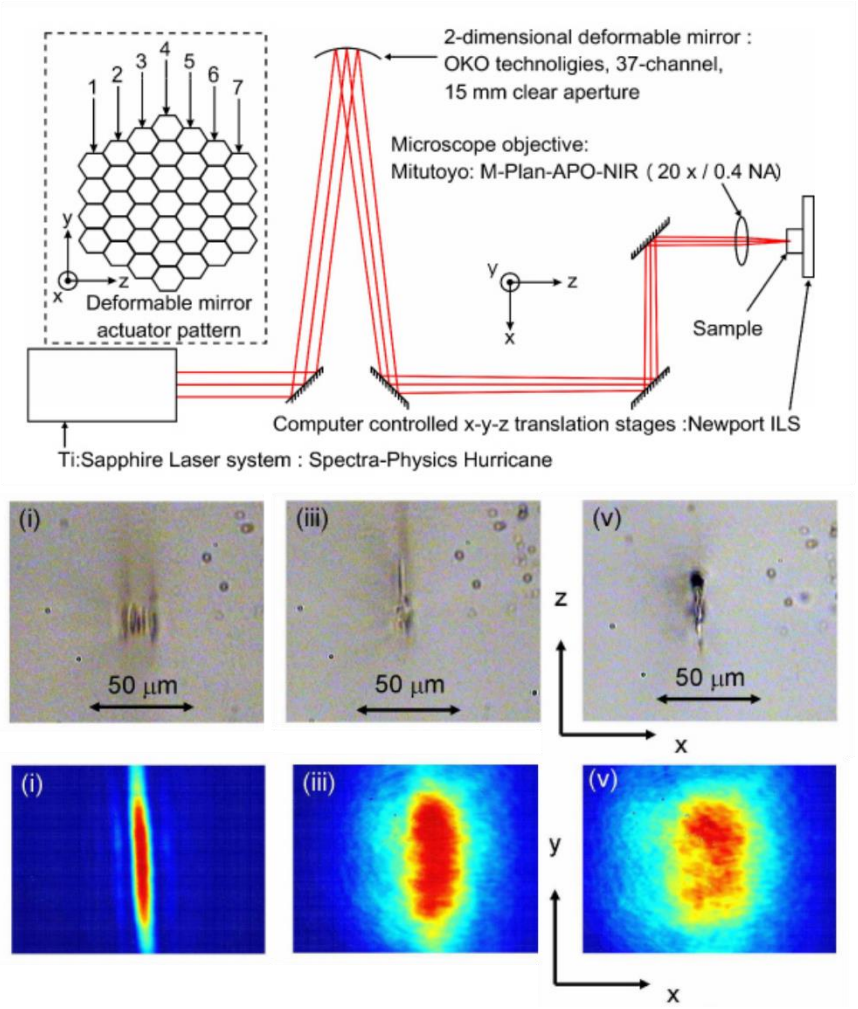

Figure 3-10 – (Top) Diagram of experimental setup used fabricate waveguides using active optics beam shaping. (Middle) Optical micrograph of waveguide cross sections for three different mirror settings and (Bottom) the corresponding CCD camera images of the laser beam. Image from [37].

3.3.4 Spatiotemporal focussing

A possibly simpler technique that retains the flexibility required for the inscription of certain structures is that of spatiotemporal focussing first implemented by He *et al.* in 2010 [39] (Fig 3.11). In this technique, a spectral chirp is applied across the beam, which reduces the spectral bandwidth of the pulse. The effect of this reduction is to stretch the pulse temporally, with the pulse duration fully restored only in the focal volume. The pulse duration determines the peak power, so the degree of spatial chirp determines the height of the modified region. This technique is therefore unique in that it allows a focal volume with a close to spherical cross-section, allowing the sample to be translated in any direction with little effect in the performance of the inscribed structure.

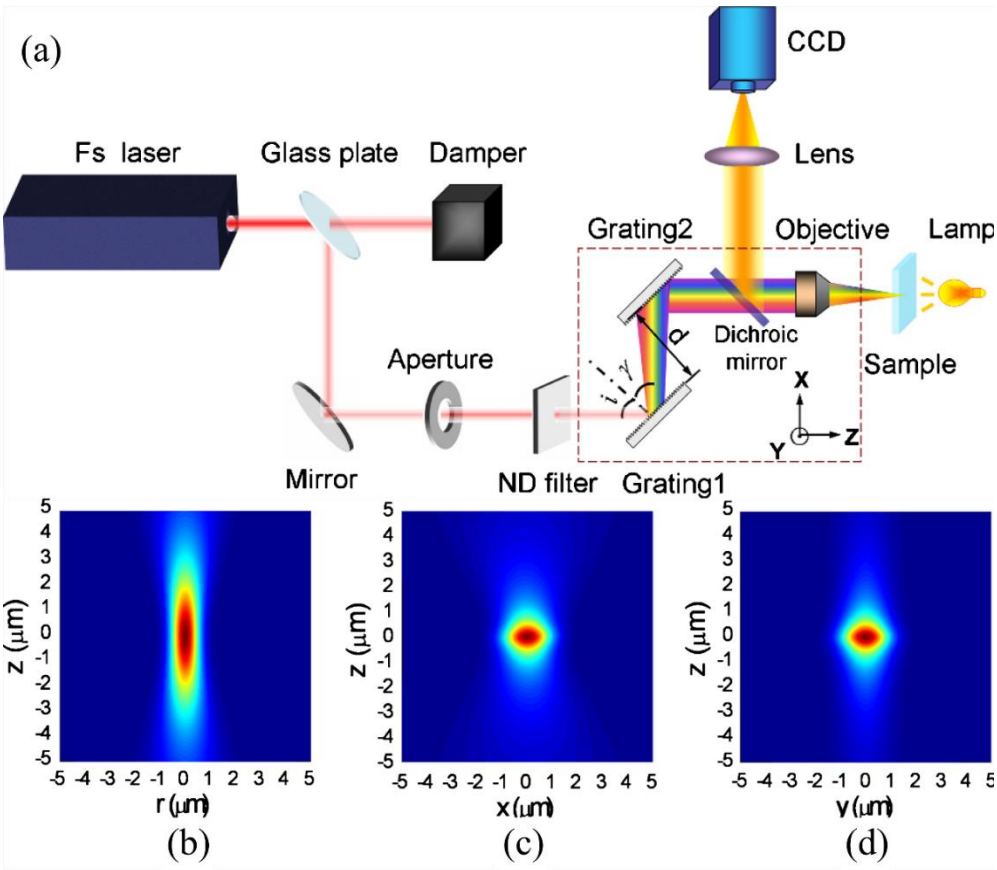

Figure 3-11 – (a) Schematic of the experimental setup for spatiotemporal focusing, calculated laser intensity distributions at the focus produced: (b) without temporal focusing and with temporal focusing in the (c) XZ and (d) YZ planes. Image from [39].

3.3.5 Multiscan technique

An alternative waveguide shaping technique that avoids beam shaping is that of the multiscan technique - first demonstrated in 2004 by Said *et al.* [40]. This technique has the benefit of being the simplest to implement with just the basic ULI setup required. The asymmetric beam is scanned through the sample multiple times, with each scan having a slight horizontal offset from the previous to build up a single waveguide with an overall symmetric profile (Fig 3.12). Waveguides inscribed using this technique have been shown to demonstrate an almost step-index refractive index profile, and as such any arbitrarily desired cross-section can be designed. As the structure is built up over many passes with some degree of overwriting, an inscription beam of relatively low peak intensity can be used, which should reduce defects and scattering centres inscribed into the modified region. As such some of the lowest loss ULI waveguides, with a propagation loss of 0.12 dB/cm, have been reported in 2005 by Nasu *et al.* using this technique [41]. This technique has been applied to a variety of materials, both active and passive. To

form a single mode waveguide around 20 scans with separations of a few hundred micrometres between each scan. This demonstrates a possible downside in this approach, the inscription of a single device will take a significantly longer than those manufactured with a technique that requires only a single scan to write each waveguide. Therefore, this technique may not be immediately suitable for more complex, larger structures or those intended for mass manufacture.

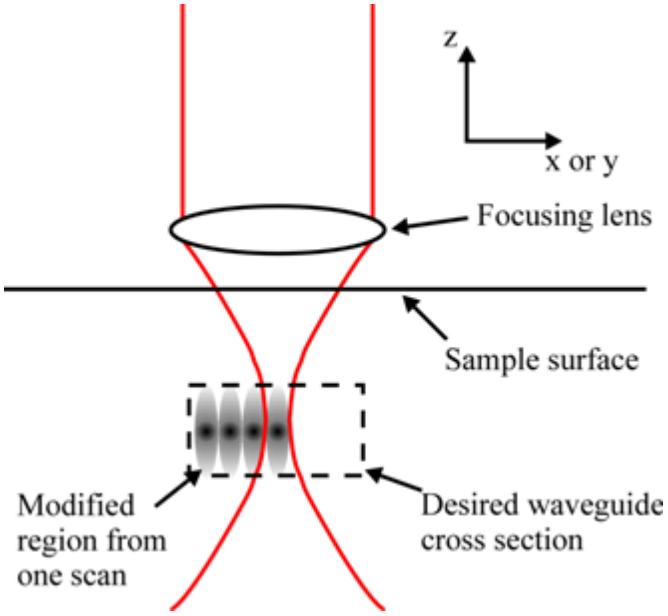

Figure 3-12 – Schematic diagram of how a symmetric waveguide can be produced from an asymmetric focal spot using the multiscan technique. Image from [42].

3.4 Conclusions

ULI is an adaptable technique that enables the design and fabrication of custom three-dimensional optical waveguide components. The technology facilitates the production of fully integrated, small components. This potential is further enhanced by the ability to inscribe channels and lenses and chemically etch these out. With the capability to directly write complex structures without the need for a mask the technique is highly adaptable and can be used to create unique one-off components for a relatively low cost. The ability to perform this in a large variety of substrates is also very desirable.

As a result of these reasons ULI has recently become an area of great interest to the field of astronomy and is being investigated by several groups around the world as a route to producing low-cost, efficient, and compact astronomical instruments. The current drive to produce ground based ELTs is only going to increase the demand for such components. Additionally, the production of stable, lightweight and passively aligned instruments

makes them potentially ideal for space-based applications where the need for low weight and the ability to survive a launch are key.

3.5 References

[1] K. M. Davis, K. Miura, N. Sugimoto, and K. Hirao, "Writing waveguides in glass with a femtosecond laser," *Opt. Lett.* **21**, 1729–1731 (1996).

[2] K. O. Hill, Y. Fujii, D. C. Johnson, and B. S. Kawasaki, "Photosensitivity in optical fiber waveguides: Application to reflection filter fabrication," *Appl. Phys. Lett.* **32**, 647–649 (1978).

[3] P. F. Moulton, "Spectroscopic and laser characteristics of Ti:Al2O3," *J. Opt. Soc. Am. B* **3**, 125–133 (1986).

[4] W. Koechner and M. Bass, *Solid-State Lasers - A Graduate Text* (Springer, 2003).

[5] D. E. Spence, P. N. Kean, and W. Sibbett, "60-fsec pulse generation from a self-mode-locked Ti:sapphire laser," *Opt. Lett.* **16**, 42–44 (1991).

[6] R. Ell, U. Morgner, F. X. Kärtner, J. G. Fujimoto, E. P. Ippen, V. Scheuer, G. Angelow, T. Tschudi, M. J. Lederer, et al., "Generation of 5-fs pulses and octave-spanning spectra directly from a Ti:sapphire laser," *Opt. Lett.* **26**, 373–375 (2001).

[7] M. Ams, G. D. Marshall, P. Dekker, M. Dubov, V. K. Mezentsev, I. Bennion, and M. J. Withford, "Investigation of Ultrafast Laser--Photonic Material Interactions: Challenges for Directly Written Glass Photonics," *IEEE J. Sel. Top. Quantum Electron.* **14**, 1370–1381 (2008).

[8] N. D. Psaila, R. R. Thomson, H. T. Bookey, N. Chiodo, S. Shen, R. Osellame, G. Cerullo, A. Jha, and A. K. Kar, "Er:Yb-Doped Oxyfluoride Silicate Glass Waveguide Laser Fabricated Using Ultrafast Laser Inscription," *IEEE Photonics Technol. Lett.* **20**, 126–128 (2008).

[9] A. Benayas, W. F. Silva, A. Ródenas, C. Jacinto, J. Vázquez de Aldana, F. Chen, Y. Tan, R. R. Thomsom, N. D. Psaila, et al., "Ultrafast laser writing of optical waveguides in ceramic Yb:YAG: a study of thermal and non-thermal regimes," *Appl. Phys. A* **104**, 301–309 (2011).

[10] M. Ams, G. D. Marshall, and M. J. Withford, "Study of the influence of femtosecond laser polarisation on direct writing of waveguides," *Opt. Express* **14**, 13158–13163 (2006).

[11] S. M. Eaton, M. L. Ng, J. Bonse, A. Mermillod-Blondin, H. Zhang, A. Rosenfeld, and P. R. Herman, "Low-loss waveguides fabricated in BK7 glass by high repetition rate femtosecond fiber laser," *Appl. Opt.* **47**, 2098–2102 (2008).

[12] S. M. Eaton, H. Zhang, M. L. Ng, J. Li, W.-J. Chen, S. Ho, and P. R. Herman, "Transition from thermal diffusion to heat accumulation in high repetition rate femtosecond laser writing of buried optical waveguides," *Opt. Express* **16**, 9443–9458 (2008).

[13] M. Kamata, M. Obara, R. R. Gattass, L. R. Cerami, and E. Mazur, "Optical vibration sensor fabricated by femtosecond laser micromachining," *Appl. Phys. Lett.* **87** (2005).

[14] G. Cerullo, R. Osellame, S. Taccheo, M. Marangoni, D. Polli, R. Ramponi, P. Laporta, and S. De Silvestri, "Femtosecond micromachining of symmetric waveguides at 1.5 μm by astigmatic beam focusing," *Opt. Lett.* **27**, 1938–1940 (2002).

[15] K. Miura, J. Qiu, T. Mitsuyu, and K. Hirao, “Preparation and optical properties of fluoride glass waveguides induced by laser pulses,” *J. Non. Cryst. Solids* **256**–**257**, 212–219 (1999).

[16] W. Yang, C. Corbari, P. G. Kazansky, K. Sakaguchi, and I. C. S. Carvalho, “Low loss photonic components in high index bismuth borate glass by femtosecond laser direct writing,” *Opt. Express* **16**, 16215–16226 (2008).

[17] A. Zoubir, M. Richardson, C. Rivero, A. Schulte, C. Lopez, K. Richardson, N. Hô, and R. Vallée, “Direct femtosecond laser writing of waveguides in As2S3 thin films,” *Opt. Lett.* **29**, 748–750 (2004).

[18] N. D. Psaila, R. R. Thomson, H. T. Bookey, S. Shen, N. Chiodo, R. Osellame, G. Cerullo, A. Jha, and A. K. Kar, “Supercontinuum generation in an ultrafast laser inscribed chalcogenide glass waveguide,” *Opt. Express* **15**, 15776–15781 (2007).

[19] S. Sowa, W. Watanabe, T. Tamaki, J. Nishii, and K. Itoh, “Symmetric waveguides in poly(methyl methacrylate) fabricated by femtosecond laser pulses,” *Opt. Express* **14**, 291–297 (2006).

[20] Y. Hanada, K. Sugioka, and K. Midorikawa, “UV waveguides light fabricated in fluoropolymer CYTOP by femtosecond laser direct writing,” *Opt. Express* **18**, 446–450 (2010).

[21] J. Thomas, M. Heinrich, P. Zeil, V. Hilbert, K. Rademaker, R. Riedel, S. Ringleb, C. Dubs, J.-P. Ruske, et al., “Laser direct writing: Enabling monolithic and hybrid integrated solutions on the lithium niobate platform,” *Phys. status solidi* **208**, 276–283 (2011).

[22] A. G. Okhrimchuk, A. V Shestakov, I. Khrushchev, and J. Mitchell, “Depressed cladding, buried waveguide laser formed in a YAG:Nd3+ crystal by femtosecond laser writing,” *Opt. Lett.* **30**, 2248–2250 (2005).

[23] A. H. Nejadmalayeri, P. R. Herman, J. Burghoff, M. Will, S. Nolte, and A. Tünnermann, “Inscription of optical waveguides in crystalline silicon by mid-infrared femtosecond laser pulses,” *Opt. Lett.* **30**, 964–966 (2005).

[24] S. Campbell, R. R. Thomson, D. P. Hand, A. K. Kar, D. T. Reid, C. Canalias, V. Pasiskevicius, and F. Laurell, “Frequency-doubling in femtosecond laser inscribed periodically-poled potassium titanyl phosphate waveguides,” *Opt. Express* **15**, 17146–17150 (2007).

[25] V. Apostolopoulos, L. Laversenne, T. Colomb, C. Depeursinge, R. P. Salathé, M. Pollnau, R. Osellame, G. Cerullo, and P. Laporta, “Femtosecond-irradiation-induced refractive-index changes and channel waveguiding in bulk Ti3+:Sapphire,” *Appl. Phys. Lett.* **85**, 1122–1124 (2004).

[26] A. Marcinkevičius, S. Juodkazis, M. Watanabe, M. Miwa, S. Matsuo, H. Misawa, and J. Nishii, “Femtosecond laser-assisted three-dimensional microfabrication in silica,” *Opt. Lett.* **26**, 277–279 (2001).

[27] Y. Bellouard, A. Said, M. Dugan, and P. Bado, “Fabrication of high-aspect ratio, micro-fluidic channels and tunnels using femtosecond laser pulses and chemical etching,” *Opt. Express* **12**, 2120–2129 (2004).

[28] Y. Bellouard, A. A. Said, and P. Bado, “Integrating optics and micro-mechanics in a single substrate: a step toward monolithic integration in fused silica.,” *Opt. Express* **13**, 6635–6644 (2005).

[29] Y. Cheng, H. L. Tsai, K. Sugioka, and K. Midorikawa, “Fabrication of 3D microoptical lenses in photosensitive glass using femtosecond laser

micromachining," *Appl. Phys. A* **85**, 11–14 (2006).

[30] S. Gross and M. J. Withford, "Ultrafast-laser-inscribed 3D integrated photonics: challenges and emerging applications," *Nanophotonics* **4**, 332–352 (2015).

[31] L. Shah, A. Y. Arai, S. M. Eaton, and P. R. Herman, "Waveguide writing in fused silica with a femtosecond fiber laser at 522 nm and 1 MHz repetition rate," *Opt. Express* **13**, 1999–2006 (2005).

[32] S. M. Eaton, H. Zhang, P. R. Herman, F. Yoshino, L. Shah, J. Bovatsek, and A. Y. Arai, "Heat accumulation effects in femtosecond laser-written waveguides with variable repetition rate," *Opt. Express* **13**, 4708–4716 (2005).

[33] C. Hnatovsky, R. S. Taylor, E. Simova, P. P. Rajeev, D. M. Rayner, V. R. Bhardwaj, and P. B. Corkum, "Fabrication of microchannels in glass using focused femtosecond laser radiation and selective chemical etching," *Appl. Phys. A* **84**, 47–61 (2006).

[34] R. Osellame, S. Taccheo, M. Marangoni, R. Ramponi, P. Laporta, D. Polli, S. De Silvestri, and G. Cerullo, "Femtosecond writing of active optical waveguides with astigmatically shaped beams," *J. Opt. Soc. Am. B* **20**, 1559–1567 (2003).

[35] Y. Cheng, K. Sugioka, K. Midorikawa, M. Masuda, K. Toyoda, M. Kawachi, and K. Shihoyama, "Control of the cross-sectional shape of a hollow microchannel embedded in photostructurable glass by use of a femtosecond laser," *Opt. Lett.* **28**, 55–57 (2003).

[36] M. Ams, G. D. Marshall, D. J. Spence, and M. J. Withford, "Slit beam shaping method for femtosecond laser direct-write fabrication of symmetric waveguides in bulk glasses," *Opt. Express* **13**, 5676–5681 (2005).

[37] R. R. Thomson, A. S. Bockelt, E. Ramsay, S. Beecher, A. H. Greenaway, A. K. Kar, and D. T. Reid, "Shaping ultrafast laser inscribed optical waveguides using a deformable mirror," *Opt. Express* **16**, 12786–12793 (2008).

[38] A. Ruiz de la Cruz, A. Ferrer, W. Gawelda, D. Puerto, M. G. Sosa, J. Siegel, and J. Solis, "Independent control of beam astigmatism and ellipticity using a SLM for fs-laser waveguide writing," *Opt. Express* **17**, 20853–20859 (2009).

[39] F. He, H. Xu, Y. Cheng, J. Ni, H. Xiong, Z. Xu, K. Sugioka, and K. Midorikawa, "Fabrication of microfluidic channels with a circular cross section using spatiotemporally focused femtosecond laser pulses," *Opt. Lett.* **35**, 1106–1108 (2010).

[40] A. A. Said, M. Dugan, P. Bado, Y. Bellouard, A. Scott, and J. Mabesa Jose R., "Manufacturing by laser direct-write of three-dimensional devices containing optical and microfluidic networks," *Phot. Process. Microelectron. Photonics III. Proc. SPIE* **5339**, 194–204 (2004).

[41] Y. Nasu, M. Kohtoku, and Y. Hibino, "Low-loss waveguides written with a femtosecond laser for flexible interconnection in a planar light-wave circuit," *Opt. Lett.* **30**, 723–725 (2005).

[42] R. R. Thomson, N. D. Psaila, H. T. Bookey, D. T. Reid, and A. K. Kar, *Femtosecond laser micromachining, photonic and microfluidic devices in transparent materials*, R. Osellame, G. Cerullo, and R. Ramponi, Eds. (Springer, 2012).

Chapter 4 – Ultrafast laser inscription of volume gratings for astronomical instruments

4.1 Motivation

The dispersion element is the key component in a spectrograph, and in astronomical spectrographs is commonly a diffraction grating. Early diffraction gratings were surface gratings, produced by direct diamond ruling of the material surface. Later gratings were formed from a surface photoresist layer subject to a holographic exposure. These techniques have a few key drawbacks, most notably the grating being very fragile and requiring care when handling. Any contact with the surface has the potential to cause permanent and irreparable damage to the grating and its performance. This causes difficulties in cleaning the grating, prevents application of any protective or anti-reflective coatings and can limit the lifetime of the component. Grating customization can also be more difficult as these gratings are most commonly produced as a replica of an expensively ruled master.

Recently a new type of holographic grating has been developed, whereby light is diffracted due to a bulk refractive index modulation. These volume phase holographic (VPH) gratings are most commonly manufactured using dichromated gelatin (DCG). DCG is applied to a glass substrate, for example BK7 or fused silica, then exposed to an interference pattern and processed to permanently set the index modulation. Finally, a second glass substrate is affixed to the top to sandwich the DCG layer within the centre of the component to protect the grating and enable the component to be held and cleaned. VPH gratings can provide very high peak diffraction efficiencies, approaching 100 %. They also exhibit a number of benefits over surface relief (SR) gratings [1], these include:

(i) The ability to be more easily handled and cleaned.
(ii) The ability to apply an anti-reflective coating to the substrate.
(iii) A reduction in scattered light and ghost images.
(iv) More uniform gratings with less anomalies.
(v) Suitability for much higher line densities, especially for transmissive gratings with line densities of up to 6000 lines/mm.
(vi) Easier customisation and the ability to produce more complex structures.

All these properties have resulted in VPH gratings being the element of choice for many astronomical spectrographs [2].

There is, however one key limitation of VPH gratings which makes them unsuitable for certain astronomical applications. The holographic material DCG has a transmittance from 0.3 to 2.8 μm, with most being commonly made for wavelengths between 0.35 and 1.5 μm [1]. The DCG must have a high purity in order to access the higher end of its transmission window and a suitable base substrate must be used. This limitation makes VPH gratings unsuitable for use in mid-infrared spectroscopy. One potential alternative is the use of ULI to directly inscribe grating structures in a bulk material, which is transmissive in the mid-infrared wavelength range. As these gratings are volume gratings within the surface of the substrate they retain most of the advantages that VPH gratings have over SR gratings.

4.2 Theory of volume gratings

Diffraction gratings are essentially governed by the principles behind double slit interference, whereby a beam of light is passed through two slits, which effectively create two coherent point sources that interfere to form a diffraction pattern of light and dark fringes. The location of light fringes can be determined by:

$$d \sin \theta = m \lambda \qquad \text{(Eq. 4.1)}$$

Where d is the separation of the slits, θ is the angle of the beam after the slits, m is an integer indicating the diffraction order and λ is the wavelength of the light. As the number of slits is increased the position of the interference maxima remains the same, however the width of the bright band reduces, with some faint secondary maxima orders becoming apparent (Figure 4.1). In a diffraction grating there are effectively many slits producing very defined, sharp diffraction orders.

If the grating is transparent to the incident light it is a phase grating, with light passing through different thicknesses or refractive indices, and undergoing phase changes that cause the interference. For applications in spectroscopy, any light present in the zero order is wasted, by inscribing gratings with a controlled angle it is possible to create blazed gratings that preferentially diffract all the light to a single order. Volume gratings operate with optimum efficiency at the Bragg angle, which is dependent on wavelength. This results in volume gratings positioned at a fixed angle within a spectrometer having optimum efficiency for a smaller range of wavelengths than SR gratings, with the thicker the volume grating, the smaller range of wavelengths it will function over.

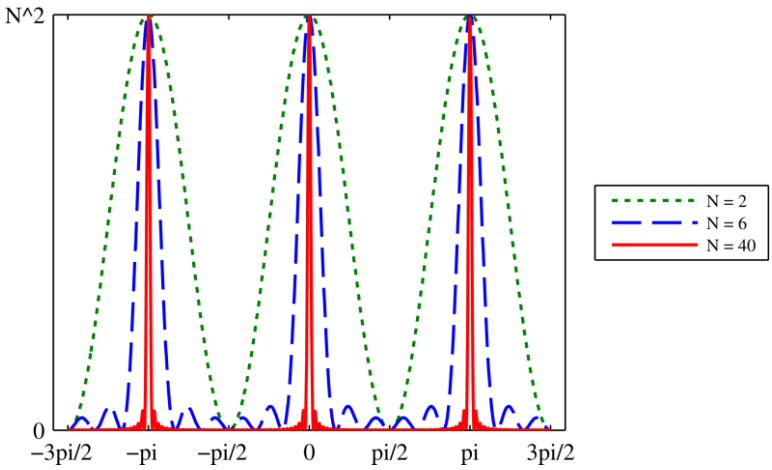

Figure 4.1 – Plot of diffraction intensity patterns for gratings with a differing number of slits, where N is the number of slits.

4.2.1 Applications of volume gratings in astronomical instruments

The benefits of VPH gratings over traditional SR gratings has led to their use in many current astronomical spectrographs. These include AAOmega at the 3.89 m Anglo Australian Telescope (AAT), a fibre-fed multi-object spectrograph covering a wavelength range from 370 to 950 nm [3]. The Goodman Spectrograph on the 4.1 m SOAR (SOuthern Astrophysical Research) Telescope, an imaging multi-object spectrograph optimized for high efficiency from 320 to 850 nm [4]. The Low Dispersion Survey Spectrograph (LDSS-3) on the 6.5 m Magellan 2 telescope was upgraded in 2004 including replacing the previous grisms (combined grating and prism element) with VPH grisms which demonstrated significantly improved throughput and resolution, the new set-up allowing efficient multi-object spectroscopy up to a wavelength of 1000 nm. The Faint Object Camera and Spectrograph (FOCAS) on the 8.2 m Subaru telescope contains several gratings, SR grisms for low resolution and VPH grisms for high resolution spectroscopy. Both the RSS (Robert Stobie Spectrograph, formerly the Prime Focus Imaging Spectrograph (PFIS)) [5] and the High Resolution Spectrograph (HRS) on the 9.2 m South African Large Telescope (SALT) utilise VPH gratings. OSIRIS (Optical System for Imaging and low Resolution Integrated Spectroscopy) on the 10.4 m GTC (Gran Telescopio Canarias) uses several VPH gratings to cover a wavelength range from 344 to 1000 nm [6].

Tests performed on VPH gratings have shown no degradation in performance at cryogenic temperatures [7] or evidence of performance change over successive thermal

cycling [8]. As such VPH gratings have also been used in instruments that require cryogenic temperatures, such as MOIRCS (Multi-Object near InfraRed Camera and Spectrograph) at the Subaru telescope [9].

VPH gratings are also being considered for spectrographs currently in development for the next generation of Extremely Large Telescopes (ELTs) with telescope apertures of 30 m. IRIS (InfraRed Imaging Spectrograph) for the Thirty Meter Telescope (TMT) is considering the use of VPH gratings to cover the wavelength range 1.19 - 1.37 μm and 1.51 - 1.82 μm [10]. Tested gratings demonstrated much higher efficiencies than SR gratings, but a much greater dependence on grating angle with the efficiency dropping significantly when the incidence angle is off the Bragg angle. New instruments on the Giant Magellan Telescope (GMT) are likely to use VPH gratings with the proposed GMACS instrument, a wide field, multi-object, moderate resolution optical spectrograph [11] and the GMTIFS, an integral-field spectrograph [12] both utilising VPH gratings in their design.

4.2.2 Previous work on the ULI fabrication of volume gratings

There have recently been several studies demonstrating the use of ULI to create volume gratings in a variety of materials. Initial studies used fused silica substrates [13], which had already been shown to work well with the ULI technique to produce gratings with peak first order diffraction efficiencies of 20 % at 633 nm achieved [14]. Further development resulted in diffraction efficiencies of 75 % for TE polarised light, with the most recent gratings demonstrating a peak diffraction efficiency of 90 % at 633 nm [15]. The fabrication of ULI volume gratings in other materials has also been investigated. A first order diffraction efficiency of 37 % at 633 nm has been demonstrated in Schott filter glass OG530 [16]. A synthetic polymer, poly(methyl)methacrylate has also been used and demonstrated 94 % first order diffraction efficiency [17], however these gratings were very thick, 4mm, therefore likely to demonstrate a very sharp reduction in the diffraction efficiency as the grating is rotated away from the Bragg condition. Gratings with a 56 % diffraction efficiency at 633 nm have been demonstrated in Schott *Foturan* photosensitive glass [18], with the samples requiring heat treatment and polishing after inscription. A mid-infrared transmitting material CaF_2 has also been used demonstrating an efficiency of 8.5 % at 633 nm [19], one possible reason for the low efficiency compared to that achieved in other materials may be the low refractive index change obtained during ULI.

4.3 ULI of volume gratings in GLS using a Fianium laser

Work previously performed at Heriot Watt University inscribed volume gratings in fused silica and Gallium Lanthanum Sulphide (GLS), a mid-infrared transmitting glass, using an IMRA FCPA μ-Jewel D400 laser [20]. This work shows that GLS was the most suitable material of the two, demonstrating less scatter than fused silica, achieving a first order diffraction efficiency of 49 % at 633 nm. The preliminary drive behind this work is to take this proof of principle demonstration and perform detailed parameter investigations to produce high efficiency mid infrared volume gratings suitable for practical applications particularly in compact spectrographs for astronomy.

4.3.1 Experimental setup

The initial fabrication was performed using a Fianium HE1060-fs laser producing 430 fs pulses of 1064 nm light. The laser light was directed through a power and polarization control setup consisting of a half wave plate and polarizing beamsplitter cube. A second half wave plate and a quarter wave plate were then used to adjust the polarisation state as required. For this work, a right circularly polarized beam was used. To ensure that the lens is fully filled, and the quoted lens NA achieved the beam is passed through a two times beam expander.

Following power and polarisation control, the laser beam was directed above crossed-roller bearing (Aerotech ANT130) stages, by way of fold mirrors, being directed through a 0.4 NA lens to form the focal spot. The translation stages allow smooth and precise translation of the sample through the focal spot. The final mirror in the setup was back polished, which allowed the back reflections from the sample surface to be monitored using a CMOS camera. This allowed the sample surface to be located and the orientation of the sample determined.

The fabricated gratings were tested at the UK Astronomy Technology Centre (ATC) at Blackford Hill in Edinburgh. The testing setup (Figure 4.2) consists of; a white light source, an order sorting filter, a monochromator, an optical fibre and a collimating lens, the grating under test and a detector. The detector used was a Silicon photodiode for measurements up to 1.2 μm and a Xenics camera for wavelengths from 1 to 2.5 μm.

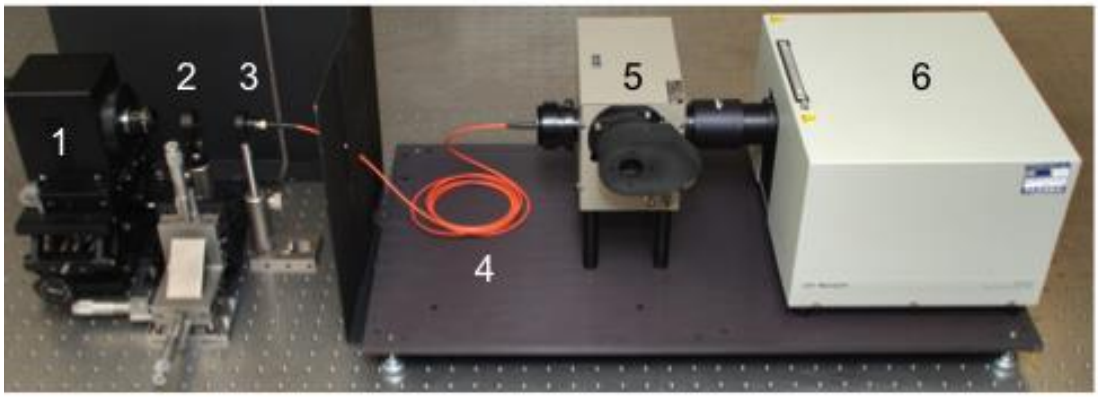

Figure 4.2 – Experimental setup for grating tests. 1. Xenics infrared camera, replaced by a silicon photodiode for visible measurements. 2. Grating under test. 3. Collimating lens. 4. Multimode fibre. 5. Monochromator. 6. White light source.

4.3.2 Optimization of pulse energy

The substrates used were 25 mm diameter, 1 mm thick discs of GLS. The test gratings were 3 mm by 3 mm in size, small enough to be relatively quick to manufacture and to allow several gratings to be inscribed on a single sample, while still big enough to be easily tested with a collimated beam with ~2 mm beam diameter. The gratings were arranged in a 4 by 4 array with a 1 mm gap between gratings (Figure 4.3 a). The gratings were inscribed by translating the sample back and forth through the focal spot at a speed of 10 mms^{-1}, with each adjacent line separated by 3 μm for a total of 1000 lines.

To allow for easy testing the first gratings were designed to work well at 633 nm, and as such the grating thickness was designed to be 41 μm thick, which with the predicted refractive index change induced by the ULI in GLS would produce efficient gratings at this wavelength. The grating thickness was built up by inscribing 17 layers of grating, one above the other by moving the stages down by 1 μm after each layer, equating to 2.4 μm spacing between layers within the material (due to the refractive index of GLS, 2.4 at the laser wavelength). When viewed under the shadowgraph the gratings are a uniform colour with the darker gratings indicating those that are most efficient in the first order (Figure 4.3 b). Viewing the gratings under a microscope the ULI process is seen to produce straight uniform lines, with the modified material appearing darker (Figure 4.3 c).

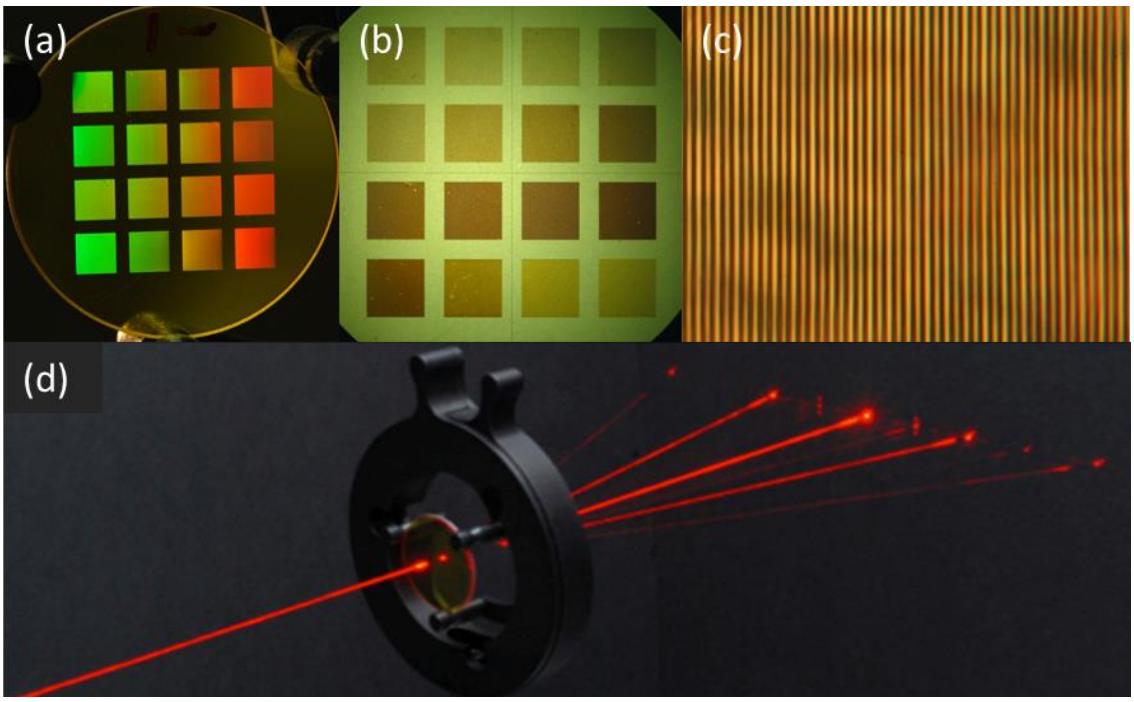

Figure 4.3 – (a) Photograph of GLS sample showing 16 inscribed gratings. (b) Shadowgraph image of sample showing uniform colour of gratings, marks in some gratings caused by dirt on sample surface, samples need to be very clean before performing ULI. (c) Close up microscope image of grating showing straight linear lines of modification, dark lines. (d) Photograph of HeNe laser incident on grating showing clear diffraction orders with very little scatter and a few ghost images. Image taken by Dr David Lee in a darkened room using a long exposure and a piece of black card moved through the laser beam by hand, showing the laser beam. At the end of the exposure the camera flash is used to illuminate the apparatus.

To determine the optimum pulse energy for the modification a sample was written with 16 gratings written from 11 to 177 nJ in approximately 11 nJ steps. The samples were initially tested with a 633 nm laser and very clear diffraction orders were visible with little visible scatter and only a few faint ghost images (Figure 4.3 d). The contribution of the ghost images and scattered light was determined by measuring the total integrated transmittance, and subtracting from this the measured efficiency of the expected diffraction orders. The total integrated transmittance of the grating was measured by placing the aperture of an integrating sphere within a few millimetres of the grating to capture the entire output beam. The efficiency of the diffraction orders was measured with the integrating sphere placed at a distance of a few centimetres from the grating to capture only the light contained within the individual diffraction order. The gratings were measured to produce less than 5 % scattered light at 633 nm, with longer wavelengths expected to produce less scatter and having < 1 % contribution at 2500 nm. Of interest the clearest ghost images were present equidistant between the expected, bright

diffraction orders of a 3 μm grating period and correspond to the diffraction pattern expected from a 6 μm grating period. The origin of this is expected to be an interference effect within the grating, the exact nature of which is currently unknown and could merit further investigation, however for this work parameters were chosen that reduced this effect as much as possible.

The grating efficiency was tested, with the angle of the grating altered to maximise the first order diffraction efficiency for each pulse energy (Figure 4.4 a). The measured diffraction efficiency of any given grating was deemed to be quite accurate with errors of ± 2 %, determined taking into account; repeat measurements; the stability of the light source; measurement error and dark counts of the detector; and positional dependency of the beam on the grating. There may however be larger differences between gratings written with nominally identical design and inscription parameters, but manufactured in different batches at different times due to the performance of the ULI process being susceptible to laboratory issues, such as room temperature, beam alignment and dust.

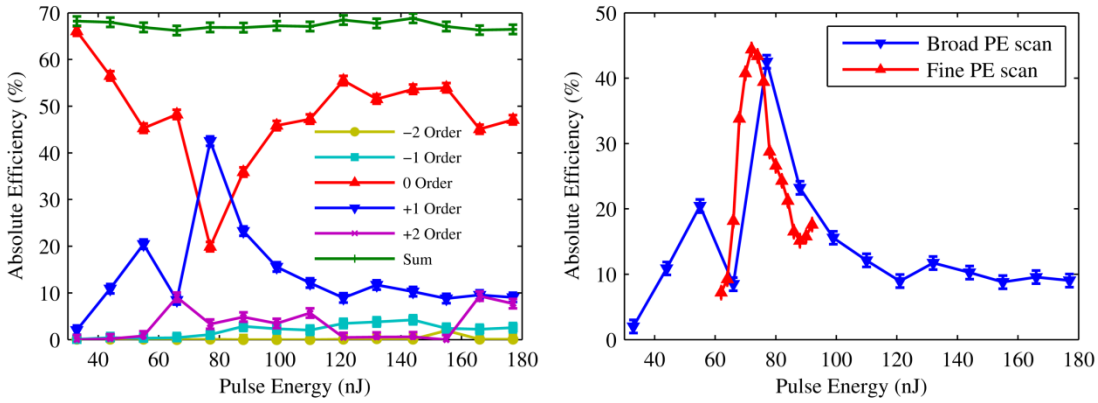

Figure 4.4 – (a) Plot of diffraction efficiency measured at 633 nm for the -2 to +2 diffraction order vs. laser pulse energy for gratings written with a broad PE scan by the Fianium laser. (b) Plot of diffraction efficiency measured at 633 nm vs. pulse energy for the 1st diffraction order for a broad and fine PE scan.

The optimum pulse energy was found to be 77 nJ producing a 42.5 % absolute diffraction efficiency in the first order. A second sample was inscribed with a much finer pulse energy scan of 2 nJ steps from 62 to 92 nJ. The optimum pulse energy in this sample was 72 nJ, producing a first order diffraction efficiency of 44.4 % (Figure 4.4 b). The slight difference between the optimum pulse energy found from the broad and fine pulse energy (PE) tests is due to the alignment of the system being adjusted between the two runs. After the fine PE scan the system alignment was not altered and subsequent tests showed that 72 nJ consistently produced gratings with diffraction efficiencies of 44 %.

4.3.3 Investigation of grating thickness

The effect of increasing the grating thickness was investigated using the optimum pulse energy of 72 nJ determined in the previous Section. Increasing the grating thickness increases the wavelength at which the first order diffraction is most efficient. Thicker diffraction gratings were manufactured by increasing the number of layers used to build up a single grating. Four gratings were inscribed with 17, 35, 53 and 71 layers resulting in approximate grating thicknesses of 41, 84, 127 and 170 μm within the sample respectively. All gratings started at a depth of approximately 150 μm below the sample surface. The grating performance in the first and zeroth orders was measured at the optimum angle for a range of wavelengths from 500 to 2500 nm (Figure 4.5 a).

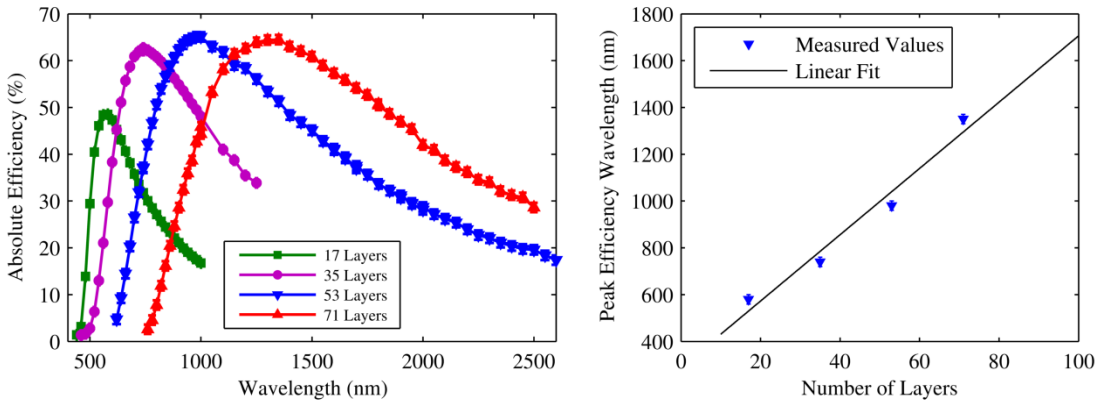

Figure 4.5 – (a) Plot of 1st order diffraction efficiency vs. wavelength for four gratings of different thicknesses with a 1.0 μm stage movement between layers. (b) Plot of the wavelength at which the 1st order diffraction efficiency is highest against the number of layers with a 1.0 μm stage movement (2.4 μm between layers within the sample).

Increasing the grating thickness increases the wavelength at which the grating is most efficient, with thicknesses of 41, 84, 127 and 170 μm resulting in peak efficient wavelengths of 580, 740, 1000 and 1350 nm producing first order diffraction efficiencies of 48.5, 62.7, 65.0 and 60.0 % respectively. The peak efficient wavelength plotted against number of layers (Figure 4.5 b) fits reasonably well to a straight line allowing a grating to be designed for a particular wavelength. Further gratings were inscribed with greater number of layers in order to push the optimum diffraction wavelength further into the mid-infrared, however these gratings always cracked or shattered the sample. This is assumed to be due to stress within the sample and in order to achieve thicker gratings it was clear that the parameters must be changed to prevent this effect.

The first order diffraction efficiency of the 71 layer grating was tested as a function of grating angle, with the first and zeroth order diffraction efficiency plotted (Fig 4.6). Dr David Lee of the ATC used GSolver grating modelling software to vary the grating profile, refractive index change and grating thickness of a simulated grating to best fit the experimental data, also plotted in Fig. 4.6. Three different grating profiles were tried, binary, sinusoidal and stepped, with the experimental data best fit by a 150 μm thick binary grating, with the modified regions having a width of 0.9 μm and a refractive index modulation of 0.0075. The simulated grating thickness of 150 μm is less than the actual thickness of the grating, approximately 170 μm. The cause of this is expected to be due to depth dependant spherical aberrations on the laser focus resulting in a depth dependent variation in the induced refractive index change.

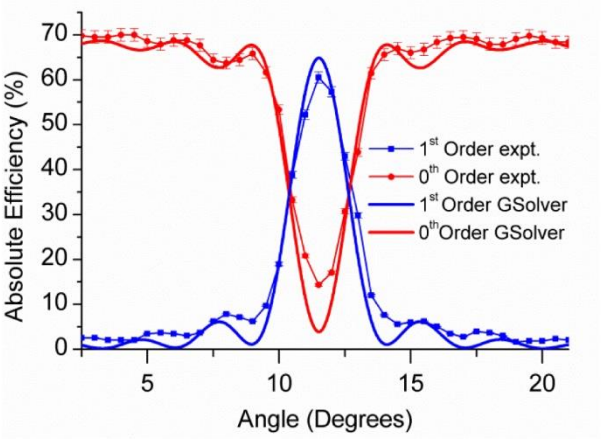

Figure 4.6 – Plot of 0th and 1st order diffraction efficiency vs. angle of incidence for the 71 layer GLS grating measured at 1300 nm, with best fit theoretical GSolver prediction also shown.

4.3.4 Investigation of anti-reflection coatings

The maximum absolute diffraction efficiency achieved was 65% at 1000 nm, this value includes losses due to light in other orders, ghost images, scattering and Fresnel reflection from the sample. GLS has a relatively high refractive index of ~2.4, resulting in significant Fresnel reflections at the air-glass interface ~17 % per surface. The transmission of GLS over the previously investigated wavelength range, 800 to 2500 nm is around 70 %. This implies that the Fresnel reflections account for most of the loss incurred in the gratings and if these effects could be reduced by applying an anti-reflection coating it may be possible to produce gratings with close to 100 % transmission. The sample discussed in Section 4.3.3 was sent to Crystran Ltd. to apply an anti-reflection coating for the range 600 to 1000 nm. The transmission of the coated material was

compared to that of the sample before the coating was applied (Fig 4.7 a), the transmission of the material increasing from around 72 % to 98 % over the designed wavelength range.

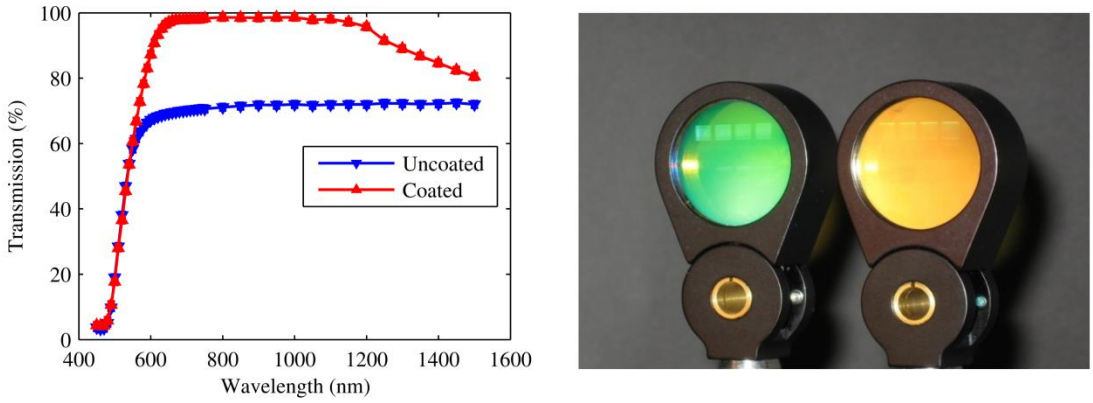

Figure 4.7 – (a) Plot of transmission vs. wavelength for a 1mm thick sample of GLS for an untreated and an anti-reflection coated sample. (b) Photograph of ULI manufactured volume gratings in (left) anti-reflection coated and (right) uncoated GLS substrates.

The sample investigating the grating thickness was retested after the application of the coating. The absolute efficiency of the 53 layer grating increased from 65 % to 89 % at 980 nm (Fig 4.8 a). For the thickest, 73 layer grating the maximum absolute efficiency increased from 65% at 1300 nm to 79.8 % at 1200 nm (Fig 4.8 b). The lower increase in the efficiency and the change in the optimum wavelength is due to the performance of the anti-reflection coating at these wavelengths. The coated gratings performed as expected with no adverse effects encountered due to the coating process. This demonstrates that ULI written gratings are very robust and can have a coating easily applied and demonstrate very high diffraction efficiencies.

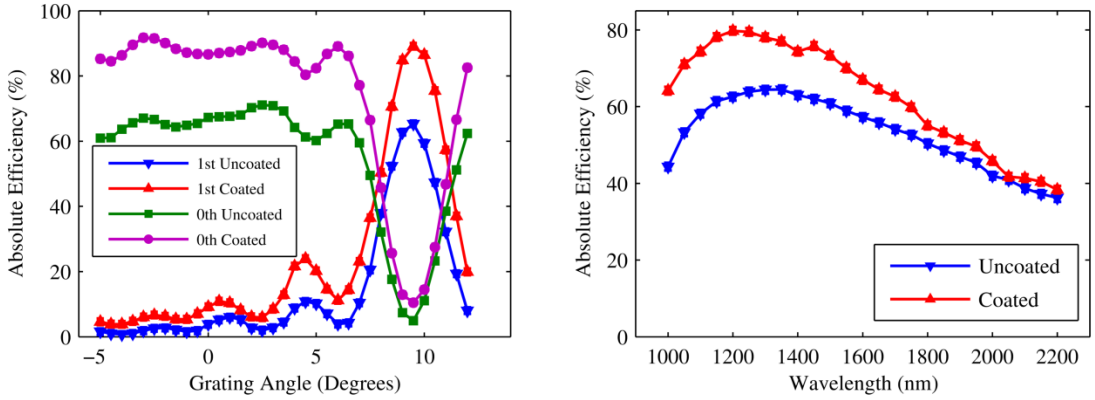

Figure 4.8 – a. Plot of 1st and 0th order diffraction efficiency vs. grating angle for an anti-reflection coated and uncoated 53 layer grating measured at 980 nm. b. Plot of 1st order diffraction efficiency vs. wavelength for an anti-reflection coated and uncoated 71 layer grating.

4.4 ULI of volume gratings in GLS using a Menlo laser

In October of 2014 the volume grating work was revisited using an improved experimental setup in order to create gratings efficient at longer wavelengths.

4.4.1 Experimental setup

The experimental setup was very similar to that described previously in Section 4.3.1, except using a new laser system and a new set of stages. The laser used was a Menlo BlueCut system providing 350 fs pulses at a wavelength of 1030 nm and a repetition rate of 500 kHz. The stages used to translate the sample were Aerotech air-bearing stages (ABL1000), which have a superior performance to the Aerotech crossed-roller bearing stages (ANT130) previously used (Table 4.1).

	Crossed-roller	Air-bearing
Resolution	1 nm	0.5 nm
Overall Accuracy	± 4 μm	± 2 μm
Repeatability	± 100 nm	± 50 nm
Straightness and Flatness	± 1.5 μm	± 0.4 μm
Pitch	12 arc sec	± 1.5 arc sec

Table 4.1 – Comparison of several key parameters of the ANT130 crossed-roller and ABL1000 air-bearing, both from Aerotech, demonstrating the superior performance of the air-bearing stages, all values taken from the Aerotech manuals for the crossed-roller bearing [21] and air-bearing [22] stages.

In an attempt to reduce the chances of the gratings cracking, the grating layout on the samples was altered to fit 14 gratings per sample, each grating separated from adjacent gratings by 1.5 mm. The grating size was 3 mm by 3 mm with 1000 lines, each separated by 3 μm, and a translation speed of 10 mms^{-1} was used as before. Initially these parameters produced much more pronounced ghost images corresponding to the diffraction pattern expected from a 6 μm grating period. This was found to be caused by the air-bearing stages not decelerating quick enough at the end of each line and then overcorrecting causing the sample and hence grating lines to not be linear at the edge of the grating. To correct this the translation speed was slowed to 0.2 mms^{-1} for the final 0.25 mm of each grating line, which produced the expected straight grating lines and a

diffraction pattern corresponding to a 3 μm grating period with minimal ghost images. As a result of this the usable area of the test gratings over which the translation speed was 10 mms^{-1} was reduced to 3 mm by 2.5 mm, which still comfortably accepted the collimated beam produced by the monochromator.

4.4.2 Optimization of pulse energy

An initial sample was fabricated with 17 layers, each separated by ~2.4 μm within the sample (stage movement of 1.0 μm) with a broad pulse energy range from 47 to 106 nJ in 6 % steps. A second sample was then written to investigate the optimum range from 61 to 69 nJ in 1.75 % steps. The optimum pulse energy was 67 nJ providing an absolute first order diffraction efficiency of ~60 % at 633 nm (Fig 4.9 a). The efficiency measured on the fine PE scan sample was slightly lower than that from the initial broad PE scan, assumed to be due to changes in the system or impurities within the GLS sample used, however a clear peak was seen demonstrating that the overall trend is reliable and identifying 67 nJ as the optimum.

Compared to similar gratings manufactured using the Fianium laser system it is clearly seen that the Menlo laser system results in gratings with a significantly higher first order efficiency, 61.4 % compared to 48.5 % (Fig 4.9 b). The optimum wavelength at which the grating operates is longer, at 660 nm when using the Menlo compared to 580 nm when using the Fianium, indicating that the Menlo induces a slightly higher refractive index change within the material.

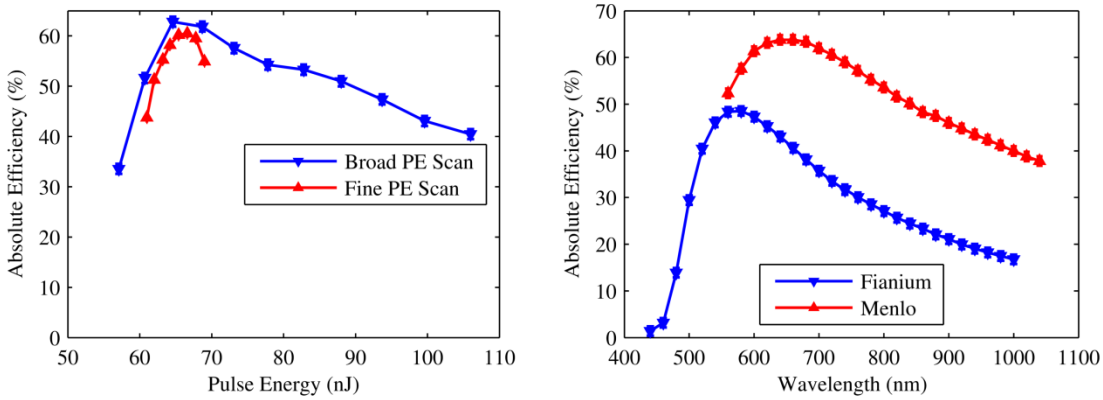

Figure 4.9 – (a) Plot of 1st order diffraction efficiency vs. pulse energy for a broad and fine scan of pulse energies at 633 nm performed using the Menlo laser. (b) Plot of 1st order diffraction efficiency vs. wavelength for 17 layer, 2.4 μm layer spacing gratings written using the Fianium and Menlo system.

4.4.3 Optimization of Layer Spacing

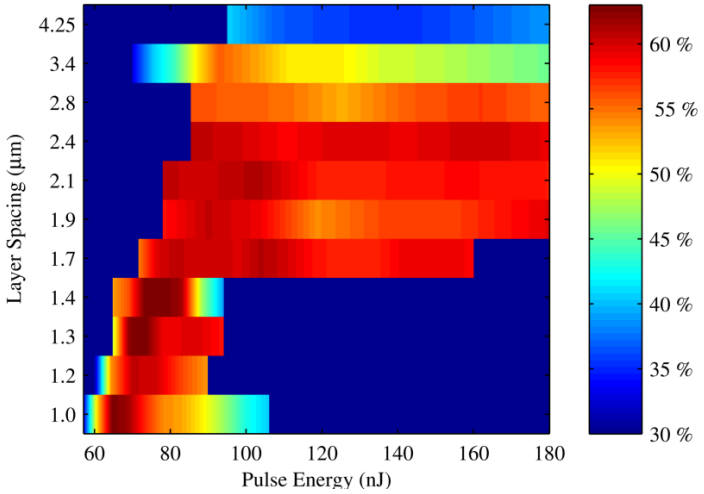

Stage movement (µm)	Number of layers	Grating thickness in sample (µm)
1.0	17	40.8
1.2	14	40.3
1.3	13	40.6
1.4	12	40.3
1.7	10	40.8
1.9	9	41.0
2.1	8	40.3
2.4	7	40.3
2.8	6	40.3
3.4	5	40.8
4.25	4	40.8

Figure 4.10 – Plot of 1st order diffraction efficiency vs. pulse energy for several different values of layer spacing (defined as the stage movement) at 633 nm. The number of layers is varied to maintain the overall grating thickness as close to 41 µm within the sample as possible. Dark blue areas indicate pulse energies that were not investigated for that particular layer spacing.

Table 4.2 – Number of layers used and overall grating thickness within the sample for each value of stage movement between layers used (the layer spacing within the sample is obtained by multiplying this with the GLS refractive index, 2.4).

One option to decrease the probability of the gratings cracking when thicker gratings are manufactured is to increase the spacing between grating layers. To investigate the effect of the layer spacing several samples were written increasing the spacing between the grating layers, while keeping the overall thickness of the gratings as uniform as possible at ~41 µm (Table 4.2). For each different layer spacing, several gratings were written in order to determine the optimum pulse energy for each spacing.

As the layer spacing increases, the optimum pulse energy also increases, however the peak of optimum pulse energy is much less pronounced, with efficiency showing a much reduced dependence on pulse energy (Fig. 4.10). As the layer separation is increased past 2.4 µm (5.76 µm within the sample), the optimum pulse energy achieved begins to fall below 60 % (Fig 4.11 a). This is most likely caused by the refractive index change within the thickness of the grating no longer being uniform as the grating layers are separated. A layer separation of 1.7 µm (4.08 µm within the sample) was selected as the optimum to use as it produced good efficiencies over a wide range of pulse energies while still being

close enough to be confident of a uniform refractive index change over the grating thickness.

The best gratings at a 1.0 and 1.7 μm layer spacing were compared (Fig 4.11 b), with the 1.7 μm spaced 10 layer grating more efficient, 65.3 % at 700 nm compared to the 1.0 μm spaced 17 layer grating, 61.3 % efficient at 660 nm. The 1.7 μm spaced grating was produced using a pulse energy of 110 nJ, and this pulse energy was used for further investigations. The increase in the layer spacing should reduce the likelihood of cracks and will also reduce the manufacture time, the 17 layer grating taking ~ 105 minutes to manufacture compared to ~ 180 minutes for the 10 layer grating.

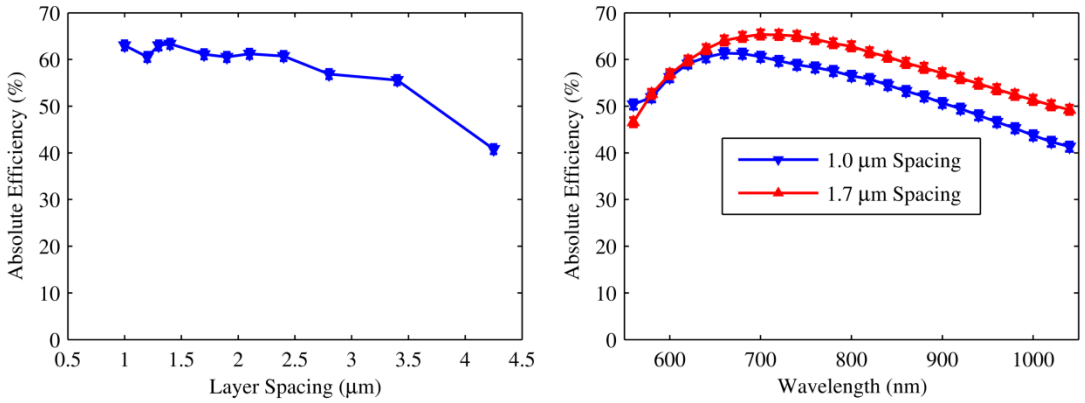

Figure 4.11 – (a) Plot of maximum 1st order diffraction efficiency vs. layer spacing (defined as stage movement). (b) Plot of 1st order diffraction efficiency vs. wavelength for 41 μm thick gratings (within the sample) with a 1.0 and a 1.7 μm stage movement (2.4 and 4.08 μm layer spacing within the sample respectively).

4.4.4 Optimization of grating thickness

Using the new parameters of 110 nJ pulse energy and a layer spacing of 1.7 μm in air, 4 μm within GLS, gratings of a varying number of layers were produced. These gratings were written individually on 10 mm by 10 mm by 1mm square samples of GLS, to prevent any chance of cracking being caused by a new grating being manufactured next to a completed grating. Gratings with 10, 20, 30 and 35 layers were manufactured with grating thicknesses of approximately 41, 82, 122 and 143 μm within the material respectively. All gratings perform well demonstrating first order diffraction efficiencies of 65, 67, 67 and 66 % at wavelengths of 700, 1350, 1600 and 1800 nm respectively (Fig 4.12 a).

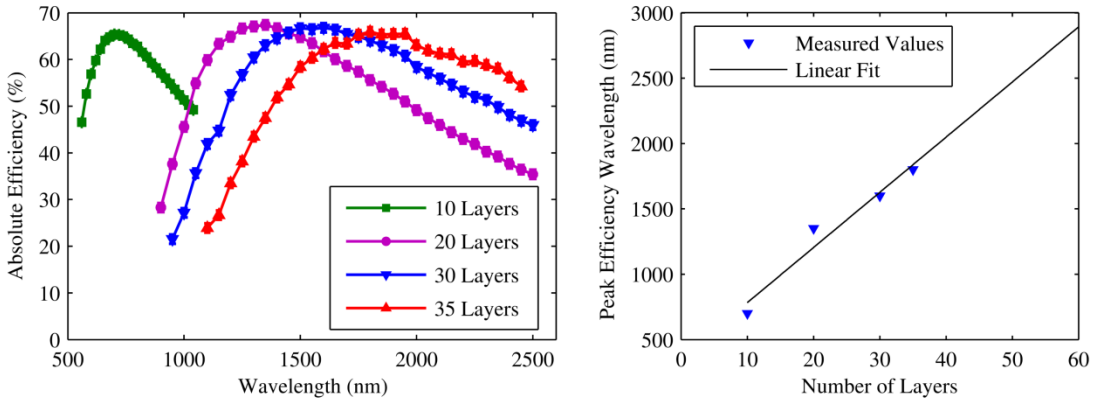

Figure 4.12 – (a) Plot of 1st order diffraction efficiency vs. wavelength for four gratings of different thicknesses with a 4.08 µm layer spacing within the sample. (b) Plot of the wavelength at which the 1st order diffraction efficiency is highest against the number of layers with a 4.08 µm layer spacing in the substrate.

By plotting the peak diffraction wavelength against the grating thickness a relatively linear relationship can be demonstrated allowing a grating which works at a desired wavelength to be easily designed (Fig 4.12 b). However, as before, attempts to produce gratings with more layers resulted in the sample cracking. The thickest grating produced using the Fianium laser, 72 nJ pulses and 2.4 µm layer spacing was 170 µm within the substrate, while the thickest grating produced using the Menlo laser, 110 nJ pulses and 4.08 µm spacing was 143 µm thick within the substrate. This shows that increasing the layer spacing does not prevent cracking, this may be due to a higher pulse energy being required to produce optimum gratings. The stress caused by the use of ULI within GLS may also cause an upper limit on the thickness of the grating achievable within the material.

4.4.5 Investigation of anti-reflection coatings 2

Previously in Section 4.3.4 the application of an anti-reflection coating to a previously inscribed volume grating was demonstrated, showing no adverse effects to the grating performance and producing very high diffraction efficiencies. An alternative scenario would be to directly write volume gratings into a sample that has already had the anti-reflection coating applied. To this end an anti-reflection coated sample was written, containing 14 gratings of 10 layers with a 4.08 µm layer spacing within the material over

a pulse energy range from 50 to 150 nJ. The antireflection coating applied was identical to that used for the sample in Section 4.3.4.

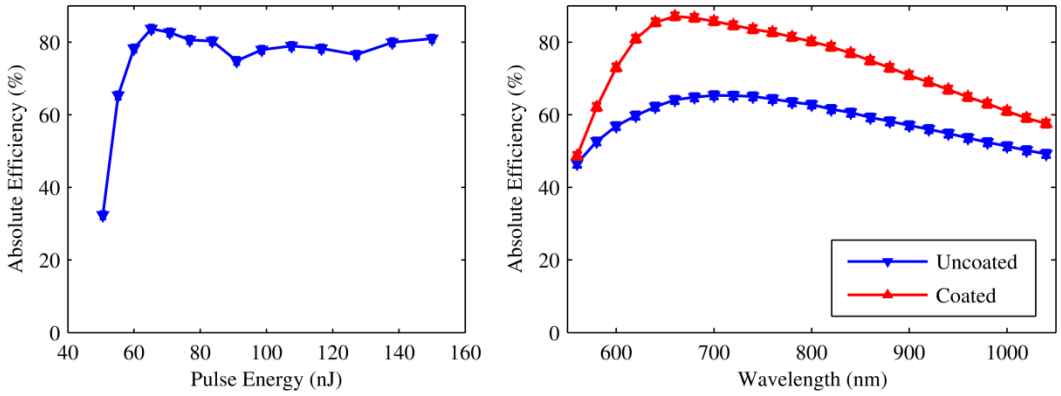

Figure 4.13 – (a) Plot of 1st order diffraction efficiency vs. pulse energy for 4.08 µm layer spaced, 10 layer gratings in anti-reflection coated GLS measured at 633 nm. (b) Plot of 1st order diffraction efficiency vs. wavelength for 4.08 µm layer spaced, 10 layer gratings in anti-reflection coated and uncoated GLS.

The optimum pulse energy for the coated sample was determined to be 65 nJ (Fig. 4.13 a), much lower than that in the uncoated sample, 110 nJ, from Section 4.4.2, as expected due to the reduction in Fresnel losses. The absolute diffraction efficiency of the coated sample 87.1 % at 660 nm is much improved from that of the uncoated sample, 65.3% at 700 nm (Fig. 4.13 b).

At wavelengths around 600 nm both the coating and the transmission of GLS are not at their optimum, therefore higher values of absolute diffraction efficiency should be possible for gratings designed for longer wavelengths. A similar new sample was written in anti-reflection coated GLS with 14 gratings made up of 14 layers, with a 4.08 µm layer spacing within the material to give a grating thickness of approximately 57 µm, covering a pulse energy range from 58 to 150 nJ. For this sample the efficiency against pulse energy was again very flat over the tested pulse energy range (Fig 4.14 a.)

For the best grating, an absolute diffraction efficiency of 95 % was achieved at a wavelength of 1020 nm (Figure 4.14 b). Gratings demonstrating a first order diffraction efficiency of 95 % are among the highest ever produced using ULI, and close to the ~99 % efficiencies achievable with VPH gratings.

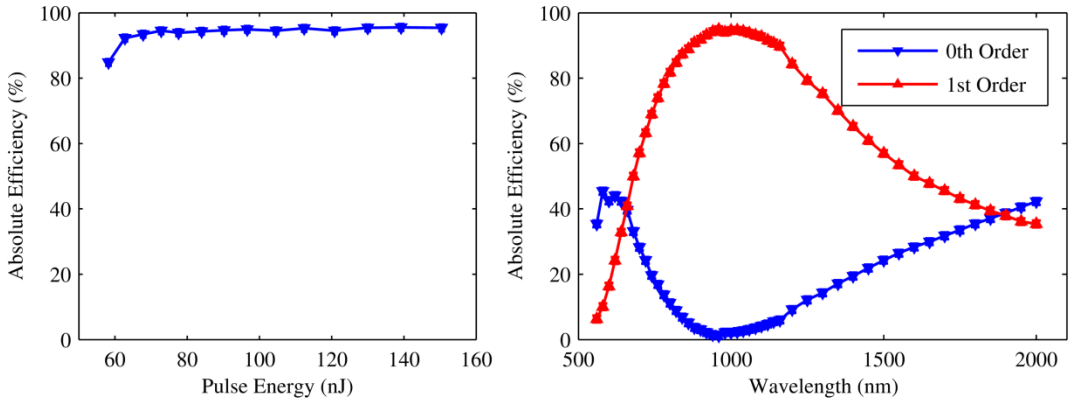

Figure 4.14 – (a) Plot of 1st order diffraction efficiency vs. pulse energy for 4.08 µm layer spaced, 14 layer gratings in anti-reflection coated GLS measured at 1000 nm. (b) Plot of 1st and 0th order diffraction efficiency vs. wavelength for the optimum 4.08 µm layer spaced, 14 layer grating.

4.5 ULI of volume gratings in IG2 using Menlo laser

It is possible from the investigations performed in GLS that there is a potential limit in the thickness of the gratings producible in the material using this setup. In order to produce gratings that work further into the mid-infrared wavelength range an alternative approach may be required. One solution would be to try a different mid-infrared transmitting material. A different material has the potential to undergo a greater refractive index change when subject to ULI, resulting in gratings that do not need to be as thick to work far into the mid-infrared. Thinner gratings would also have the advantage of demonstrating good performance over a wider wavelength range for a given grating angle. A material that requires a lower pulse energy for modification may also help by reducing the thermal expansion within the material. The mid-infrared transmitting glass Schott IG2, composed of Germanium, Arsenic and Selenium (Fig 4.15) was investigated, which has a transmission of 67 % from 2 to 10 µm for a 1 mm thick sample (Fig 4.16 a). The refractive index of IG2 at 1 µm is 2.6, slightly higher than that of GLS (2.4), again resulting in high losses due to Fresnel reflections.

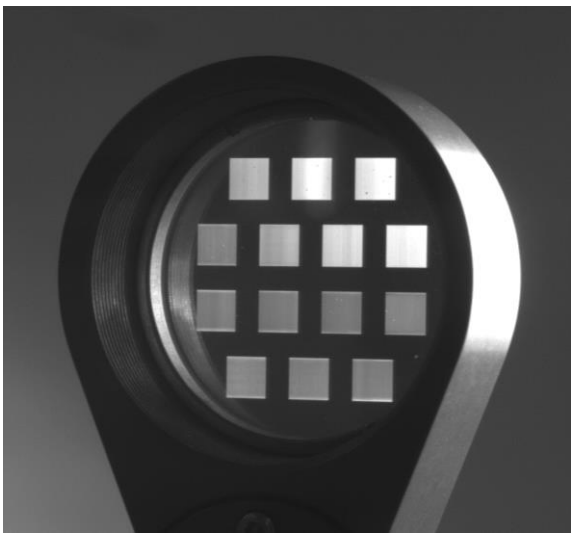

Figure 4.15 – Photograph of an illuminated, angled IG2 substrate inscribed with ULI written gratings. Gratings that appear bright are more efficiently diffracting to the 1st order.

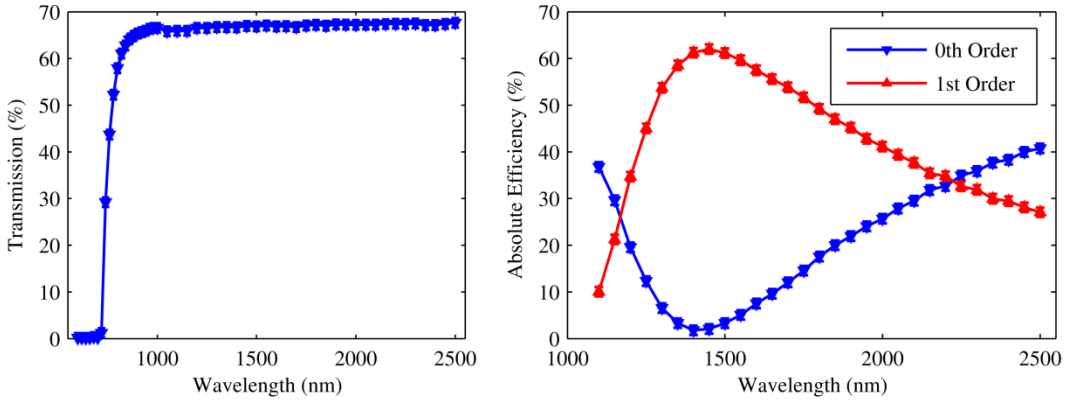

Figure 4.16 – (a) Plot of transmission of a 1 mm thick IG2 substrate vs. wavelength. (b) Plot of 1st and 0th order diffraction efficiency vs. wavelength of a 1.7 µm stage movement between layers (~4.42 µm between layers within the sample), 10 layer grating inscribed in IG2 with the Menlo laser at the optimum pulse energy of 13.8 nJ.

4.5.1 Optimization of pulse energy

Initial tests performed in IG2 were based on parameters that worked in GLS, 3 mm by 3mm gratings with 1000 lines with a line spacing of 3 µm written using the Menlo and air-bearing stages setup. The gratings were 10 layers, with a 1.7 µm stage movement, giving an approximate grating thickness of 44 µm within the material. Initial tests in IG2 showed that pulse energies higher than 80 nJ resulted in damage to the sample surface, and pulse energies above 30 nJ resulted in gratings that were opaque. A sample was written which tested pulse energies between 5 and 15 nJ. Three gratings were shown to

produce high diffraction efficiencies at 1550 nm with minimal scattered light, with the grating written with a 13.8 nJ pulse energy clearly being the most efficient. This grating demonstrated an absolute diffraction efficiency of 62 % at 1450 nm (Fig 4.16 b). The measured transmission of IG2 is ~ 67 % from 1000 to 2500 nm (Fig 4.16 a) demonstrating that very little light is lost to ghost modes and scatter, and that similar to GLS it should be possible to greatly improve the diffraction efficiency by applying a suitable anti-reflection coating. The 44 µm thick IG2 grating produced an optimum efficiency at 1450 nm, whereas the GLS grating had an optimum efficiency at a wavelength of roughly half this, 700 nm for a grating of approximately the same thickness, 41 µm, indicating that a much higher positive refractive index change is induced within IG2 than in GLS.

It is plausible that similar to GLS, the range of pulse energies that produce high diffraction efficiencies can be improved by increasing the layer spacing. Two samples were thus written investigating from 10 to 25 nJ, one with a 1.7 µm stage movement (4.42 µm layer spacing within the sample) and 15 layers, and the second with a 2.55 µm stage movement (6.63 µm layer spacing within the sample) and 10 layers, both giving an overall grating thickness of approximately 66 µm within the sample. Both samples resulted in high diffraction efficiencies with the 2.55 µm layer spacing sample resulting in a slightly higher optimum pulse energy and the range over which pulse energies provided high efficiency being slightly flatter, but not by a significant margin (Fig 4.17).

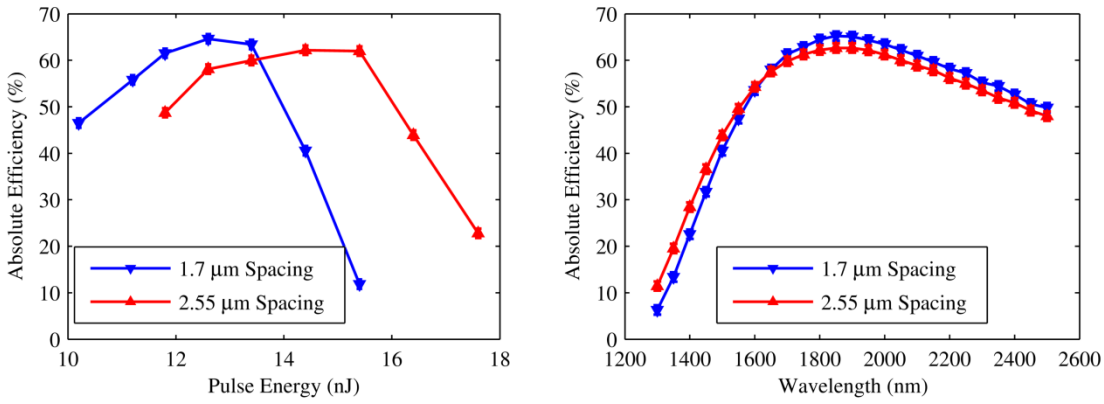

Figure 4.17 – (a) Plot of 1st order diffraction efficiency vs. pulse energy for a 1.7 µm spaced, 15 layer and a 2.55 µm spaced 10 layer grating in IG2. (b) Plot of 1st order diffraction efficiency vs. wavelength for a 1.7 µm spaced 15 layer grating at 12.8 nJ and a 2.55 µm spaced 10 layer grating at 14.4 nJ in IG2.

Comparing the Littrow curves of the best gratings manufactured using 1.7 and 2.55 µm stage movement produces very similar characteristics, 65 and 62.5 % absolute efficiency at 1900 nm respectively (Fig 4.17 b), showing very little loss in performance by reducing

the number of layers. It is possible that the number of layers could be further reduced; however the limits of the material, whereby it begins to be opaque at pulse energies higher than 30 nJ may limit the separation of the layers.

4.5.2 Optimization of grating thickness

The effect of grating thickness in IG2 was further investigated by writing samples with an increased number of layers. As there was no great benefit in using a 2.55 μm stage movement, a 1.7 μm stage movement (4.42 μm layer spacing within the material) was used. As the optimum pulse energy was so low at 13 nJ it was presumed that there was less likelihood of the sample cracking. Three samples were produced, each containing a larger 6 mm by 6mm grating in its centre, with 22, 30 and 40 layers, producing approximate grating thicknesses of 97, 133 and 177 μm within the sample respectively. A larger grating was used to make it easier to ensure the test beam was within the grating at infrared wavelengths.

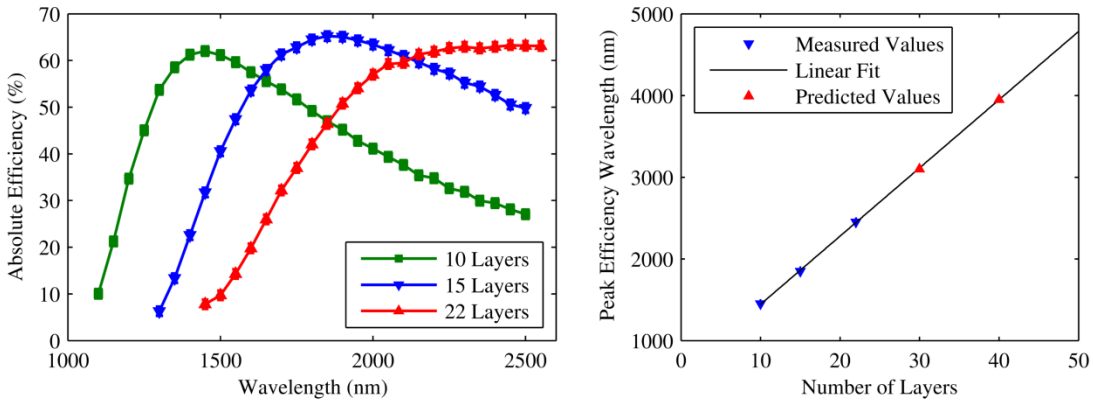

Figure 4.18 – (a) Plot of 1st order diffraction efficiency vs. wavelength for three gratings of different thicknesses with a 4.42 μm layer spacing. (b) Plot of the wavelength at which the 1st order diffraction efficiency is highest against the number of layers with a 4.42 μm layer spacing. Predicted values are the expected peak efficient wavelengths for manufactured, but untested gratings inferred from the best line fit from tested gratings.

The 10, 15 and 22 layer gratings produce a maximum first order efficiency of 62, 65 and 63 % at a wavelength of 1450, 1850 and 2500 nm respectively (Fig 4.18 a). Measurements for the 30 and 40 layer gratings were not performed, as the current measurement setup at the ATC did not allow measurements at wavelengths longer than 2.5 μm, requiring a new mid-IR detector. The wavelengths of the maximum diffraction efficiency were plotted, and a straight line fit was applied (Fig 4.18 b). The peak efficient

wavelengths for the 30 and 40 layer gratings were then predicted from the straight line fit to be 3100 and 3950 nm respectively.

The 30 layer grating was measured at Heriot Watt using a 3.39 μm HeNe laser producing a 53 % absolute first order diffraction efficiency, demonstrating that the trend shown in Fig 4.18 b is plausible and that the 40 layer grating could be efficient at 4 μm as predicted. This will be confirmed in the future with an improved measurement setup.

4.6 Conclusions and future work

In conclusion it has been shown that high efficiency, robust volume gratings can be inscribed in GLS for near-IR wavelengths and good efficiencies for mid-IR wavelengths, 55 % absolute efficiency at 2.5 μm. Anti-reflection coatings can be applied to the sample, both before and after inscription of the gratings with no detrimental effects and can greatly reduce the Fresnel losses, resulting in gratings that are up to 95 % efficient. This very high efficiency demonstrates that they are a viable alternative to VPH gratings for certain applications. Further work in GLS will be to solve the issue of cracking when inscribing thicker gratings.

It has been shown that IG2 performs well with ULI inscription to create high efficiency diffraction gratings with low scatter and few ghosts. IG2 has a few advantages over GLS; it is easily commercially available with a high manufacturing tolerance; the process of ULI induces a higher refractive index change within it compared to GLS; the pulse energy required for the modification is much reduced from that required in GLS. So far there have been no issues with IG2 cracking or shattering and gratings have been produced that perform well in the mid-IR, 63 % at 2.55 μm and 53 % at 3.39 μm. Thicker gratings have been successfully produced and when these are tested it is believed that these will work well at 4 μm and still produce reasonable efficiency out to 5 μm. Further work will be to produce and measure thicker gratings that can perform well in the astronomical L and M wavelength bands, 3.0 – 4.0 μm and 4.6 – 5.2 μm respectively. The gratings produced so far have demonstrated little scatter and few ghosts producing maximum diffraction efficiencies of 65 % with the transmission of blank IG2 being 67 %, showing that similar to GLS the application of a suitable antireflection coating should increase the diffraction efficiency to ~95 %.

4.7 Contributions

Prof. Robert Thomson from Heriot Watt, Prof. Colin Cunningham and Dr David Lee from the ATC came up with the initial proposal. Prof. Thomson carried out the initial grating tests on fused silica and GLS defining some initial parameters to fit a grating design defined by Dr Lee.

David MacLachlan designed, set up and aligned the initial ULI setup with the Fianium laser and crossed-roller bearings. David MacLachlan wrote the G-code commands to inscribe the gratings and carried out the manufacture of all the gratings. David MacLachlan drove forward the in-depth investigation into the effect of layer separation and performed the full characterisation of the gratings, both in the visible and near-infrared at the ATC.

Dr Lee modelled the gratings in GSolver grating modelling software to determine the theoretical parameters of the grating that best fit the measured data and suggested IG2 as an alternative material to try. Dr Lee took the photographs and shadowgraph images of the GLS samples and gratings.

The set-up and alignment of the upgraded ULI setup with the Menlo laser and air bearing stages was performed by Sebabrata Mukherjee and Dr Alexander Arriola, based on an earlier setup designed by David MacLachlan. Dr Debaditya Choudhury set up the compressor and air bearing stages.

4.8 References

[1] S. C. Barden, J. A. Arns, W. S. Colburn, and J. B. Williams, "Volume-phase holographic gratings and the efficiency of three simple volume-phase holographic gratings," *Publ. Astron. Soc. Pacific* **112**, 809–820 (2000).

[2] S. C. Barden, J. A. Arns, and W. S. Colburn, "Volume-phase holographic gratings and their potential for astronomical applications," *Opt. Astron. Instrum. Proc. SPIE* **3355**, 866–876 (1998).

[3] A. Green, S. Brough, A. R. Lopez-Sanchez, S. Sharp, R. Cannon, and T. Bridges, "2dF-AAOmega Manual, Volume I: User Guide," *Anglo Aust. Obs.*, 2015, <https://www.aao.gov.au/get/document/2dF-AAOmega-obs-manual.pdf> (1 August 2016).

[4] J. C. Clemens, J. A. Crain, and R. Anderson, "The Goodman spectrograph," *Ground-based Instrum. Astron. Proc. SPIE* **5492**, 331–340 (2004).

[5] H. A. Kobulnicky, K. H. Nordsieck, E. B. Burgh, M. P. Smith, J. W. Percival, T. B. Williams, and D. O'Donoghue, "The prime focus imaging spectrograph for the Southern African large telescope: Operational modes," *Instrum. Des. Perform. Opt. Ground-based Telesc. Proc. SPIE* **4841**, 1634–1644 (2002).

[6] A. Cabrera-Lavers, "Osiris User Manual," *Gran Telesc. Canar.*, 2014,

<http://www.gtc.iac.es/instruments/osiris/media/OSIRIS-USER-MANUAL_v3_1.pdf> (1 August 2016).

[7] P.-A. Blanche, S. Habraken, P. Lemaire, and C. Jamar, "Diffracted wavefront measurement of a volume phase holographic grating at cryogenic temperature," *Appl. Opt.* **45**, 6910–6913 (2006).

[8] N. Tamura, G. J. Murray, P. Luke, C. Blackburn, D. J. Robertson, N. A. Dipper, R. M. Sharples, and J. R. Allington-Smith, "Cryogenic tests of volume-phase holographic gratings: results at 100 K," *Appl. Opt.* **45**, 5923–5928 (2006).

[9] N. Ebizuka, K. Ichiyama, T. Yamada, C. Tokoku, M. Onodera, M. Hanesaka, K. Kodate, Y. K. Uchimoto, M. Maruyama, et al., "Cryogenic Volume-Phase Holographic Grisms for MOIRCS," *Publ. Astron. Soc. Japan* **63**, S605–S612 (2011).

[10] S. Chen, E. Meyer, S. A. Wright, A. M. Moore, J. E. Larkin, J. Maire, E. Mieda, and L. Simard, "The infrared imaging spectrograph (IRIS) for TMT: volume phase holographic grating performance testing and discussion," *Ground-based Airborne Instrum. Astron. V. Proc. SPIE* **9147**, 91478X (2014).

[11] D. L. Depoy, R. Allen, R. Barkhouser, E. Boster, D. Carona, A. Harding, R. Hammond, J. L. Marshall, J. Orndorff, et al., "GMACS: a Wide Field, Multi-Object, Moderate-Resolution, Optical Spectrograph for the Giant Magellan Telescope," *Conf. Ground-Based Airborne Telesc. IV. Proc. SPIE* **8446**, 84461N (2012).

[12] P. J. McGregor, G. J. Bloxham, R. Boz, J. Davies, M. Doolan, M. Ellis, J. Hart, D. J. Jones, L. Luvaul, et al., "GMT Integral-Field Spectrograph (GMTIFS) conceptual design," *Conf. Ground-Based Airborne Telesc. IV. Proc SPIE* **8446**, 84461I (2012).

[13] A. Y. Naumov, C. Przygodzki, X. Zhu, and P. B. Corkum, "Microstructuring with femtosecond laser inside silica glasses," *Conf. Lasers Electro-Optics CLEO*, CThC2 (Baltimore, Maryland, 1999).

[14] L. Sudrie, M. Franco, B. Prade, and A. Mysyrewicz, "Writing of permanent birefringent microlayers in bulk fused silica with femtosecond laser pulses," *Opt. Commun.* **171**, 279–284 (1999).

[15] M. Mikutis, T. Kudrius, G. Slekys, D. Paipulas, and S. Juodkazis, "High 90% efficiency Bragg gratings formed in fused silica by femtosecond Gauss-Bessel laser beams," *Opt. Mater. Express* **3**, 1862–1871 (2013).

[16] R. Martinez-Vazquez, R. Osellame, G. Cerullo, R. Ramponi, and O. Svelto, "Fabrication of photonic devices in nanostructured glasses by femtosecond laser pulses," *Opt. Express* **15**, 12628–12635 (2007).

[17] L. Ye, W. Perrie, O. J. Allegre, Y. Jin, Z. Kuang, P. J. Scully, E. Fearon, D. Eckford, S. P. Edwardson, et al., "NUV femtosecond laser inscription of volume Bragg gratings in poly(methyl)methacrylate with linear and circular polarizations," *Laser Phys.* **23**, 10 (2013).

[18] F. He, H. Y. Sun, M. Huang, J. Xu, Y. Liao, Z. H. Zhou, Y. Cheng, Z. Z. Xu, K. Sugioka, et al., "Rapid fabrication of optical volume gratings in Foturan glass by femtosecond laser micromachining," *Appl. Phys. a-Materials Sci. Process.* **97**, 853–857 (2009).

[19] Q.-Z. Zhao, J.-R. Qiu, X.-W. Jiang, C.-J. Zhao, and C.-S. Zhu, "Fabrication of internal diffraction gratings in calcium fluoride crystals by a focused femtosecond laser," *Opt. Express* **12**, 742–746 (2004).

[20] D. Lee, R. R. Thomson, and C. R. Cunningham, “Performance of volume phase gratings manufactured using ultrafast laser inscription,” *Mod. Technol. Space-Ground-based Telesc. Instrum. II. Proc. SPIE* **8450**, 84502X (2012).

[21] Aerotech Inc, “ANT130 Series Stage User’s Manual,” 2012, <http://www.aerotechmotioncontrol.com/ftp/pwpsoftware/manuals_helpfiles/Mechanical/Stages Tables and Slides/ANT130.pdf> (5 December 2016).

[22] Aerotech Inc, “ABL1000 Series Stage User’s Manual,” 2011, <http://www.aerotechmotioncontrol.com/ftp/pwpsoftware/manuals_helpfiles/Mechanical/Stages Tables and Slides/ABL1000.pdf> (5 December 2016).

Chapter 5 – Development and on-sky testing of a fully integrated reformatter for high resolution spectroscopy

5.1 Motivation

In this Chapter we present the design, manufacture and testing, both in-laboratory and on-sky of a photonic dicer (PD) device. This device is inspired by the PIMMS instrument concept proposed by Bland Hawthorn *et al.* [1] and is designed to accept a MM input from a telescope and efficiently reformat it into a linear array. As first suggested by Robert Thomson [2], the photonic dicer takes advantage of the three-dimensional capability of ULI to create a single chip that combines the photonic lantern and reformatting functions. Due to the control ULI enables it is possible to bring the output, linear array waveguides close enough together so they are coupled in one axis forming a planar waveguide, or pseudo-slit. This output is single mode and diffraction-limited in one axis and hence has the potential to be used as the input to a high-resolution spectrograph, which could in principle operate free of modal noise.

The design and manufacture of the PD was performed at Heriot Watt University in the summer of 2013 with equal contribution from Dr Robert J. Harris from the Centre for Advanced Instrumentation at Durham University. The chip was tested on-sky on the WHT in La Palma in collaboration with the CANARY AO system team in September of 2013. The on-sky testing presented in this Chapter is based upon [3] and was performed in collaboration with the authors of the paper.

5.2 Photonic dicer manufacture

5.2.1 Photonic dicer design

The PD was designed with the intention to test the device with the CANARY AO system, and hence match the Full Width Half Maximum (FWHM) of the PSF provided by CANARY. Averaged images of the input supplied by the CANARY team were used to determine the FWHM of the PSF. From these an estimate of the number of modes contained within the CANARY PSF was determined so a photonic dicer supporting an equal number of modes could be produced:

$$M = \left(\frac{\pi \chi D_T}{4\lambda}\right)^2 \qquad \text{(Eq. 5.1)}$$

Where M is the number of supported modes, χ is angular size of the PSF, defined as the FWHM intensity of the PSF, approximately 450 – 480 mas, D_T is the telescope diameter, in the case of the WHT, 4.2 m and λ is the central wavelength [4][5]. In the on-sky experiments the central wavelength is 1530 nm, determined by the pass bands of the Xenics Xeva-1.7 320 InGaAs camera and the H-band filter used [6]. This would result in approximately 25 spatial modes.

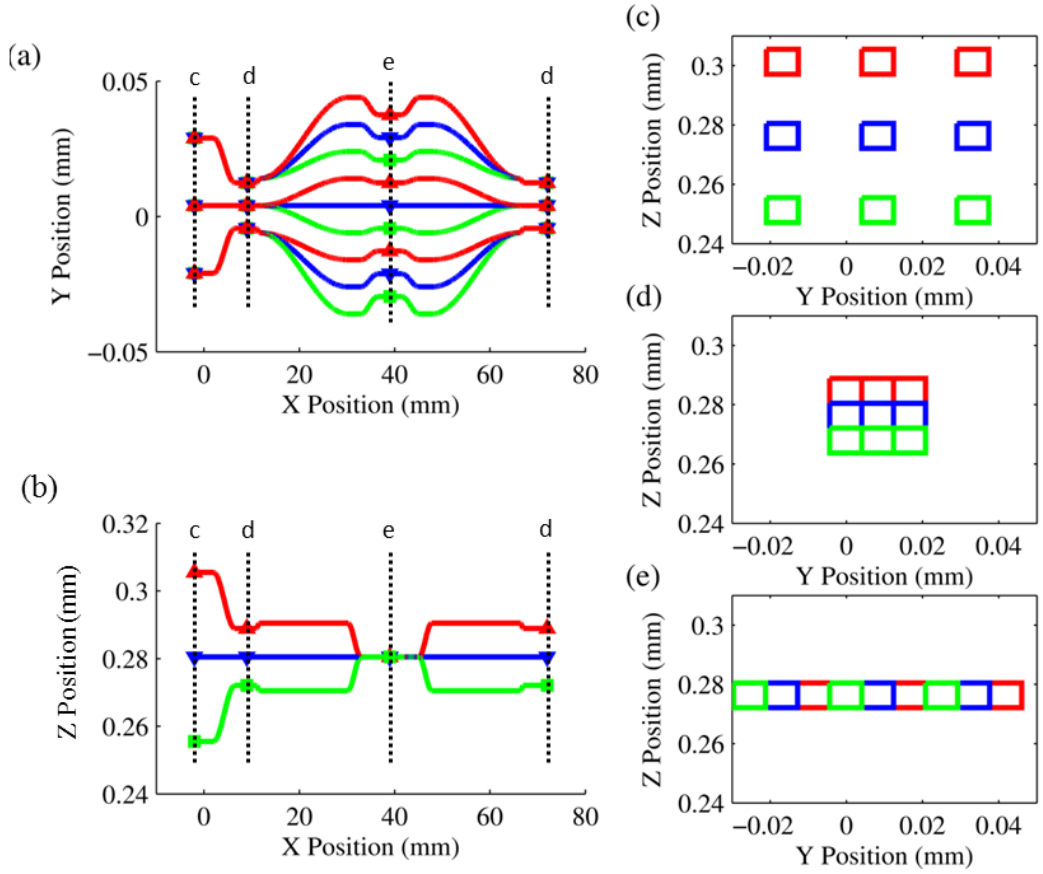

Figure 5.1 – Schematics of the waveguide paths for the full 9 mode photonic dicer showing (a) top view and (b) side view. Waveguide layout and separations are shown as cutaways for the; (c) input, (d) multimode and (e) slit configurations. The deepest waveguides, (in green) were inscribed first, followed by blue then red.

To best accommodate the varying seeing at the telescope caused by atmospheric turbulence a single chip containing several PD devices was manufactured, each supporting a different number of spatial modes. Each device could be tested on bench during the day using the telescope simulator in the CANARY set-up, with the ideal device

used for the on-sky tests. Individual waveguides were written by ULI using the multiscan geometry to produce a SM waveguide with a square symmetric cross-section. The PD devices are based on a multimode waveguide built up as a K x K array of SM waveguides, with K ranging from 2 to 7, producing dicers which could support 4, 9, 16, 25, 36 and 49 spatial modes respectively.

In order to perform a full in laboratory characterisation of the devices, they were written in a 70 mm long chip comprising of three sections (Fig 5.1). The first section was a 10 mm long input section and comprises an input of uncoupled single mode waveguides, arranged in a square with a 25 μm centre-to-centre separation (Fig 5.1 c), reformatting these to form a single square multimode waveguide (Fig 5.1 d). The second section was 30 mm long and is the photonic dicer, hereafter referred to as PD1, whereby the waveguides forming the multimode waveguide are separated and reformatted into a slit (Fig 5.1 e). The final section was 30 mm long and is the photonic dicer in reverse, referred to as PD2, taking the slit output and reformatting it into a square multimode waveguide. The input section allows easy characterisation of the full device by using a single mode fibre to measure the throughput of each of the single-mode input channels and averaging across all of these to the determine the throughput of the full device.

5.2.2 Photonic dicer manufacture

The on-sky tests would be performed over a wavelength range of 1450 to 1610 nm, as such the photonic dicers were designed to be well matched to 1550 nm. This wavelength was chosen as it is well within the passband with many optical fibres, lasers and detectors designed for this wavelength for easy testing. The waveguides were inscribed using a 500 kHz pulse train of 460 fs pulses with a central wavelength of 1064 nm generated by a fibre laser (Fianium Femtopower 1060fs). The substrate used was a borosilicate glass (Corning *EAGLE 2000*) and was mounted on crossed-roller bearing x-y-z translation stages (Aerotech ANT). The borosilicate glass *EAGLE 2000* was used as it is a readily available, relatively cheap glass of reliable, reproducible quality. In addition this material has demonstrated good performance with ULI, in particular in laser repetition rate regimes higher than 200 kHz, when accumulative heating effects begin to apply over other materials such as fused silica [7]. The waveguide parameters were determined by an iterative process to produce low loss single mode waveguides that was well matched to standard SMF-28 fibre. To determine these parameters a series of straight 20 mm long waveguides were inscribed in a substrate for a variety of pulse energies, translation

speeds, number of scans, scan separations and focusing lenses. The performance of each waveguide was tested by cleaving an SMF28 optical fibre transmission line and butt-coupling this to the grinded and polished optical quality facet of the substrate. The throughput of each waveguide was maximised, using decane as an index matching liquid and optimising the x,y,z and the pitch and yaw alignment of both the input and output fibres to the waveguide. The optimum waveguides were obtained when the pulses were focused using a 0.3 NA aspheric lens at a depth of 200 μm below the substrate surface with a pulse energy of 251 nJ and a circularly polarised beam. Each single mode waveguide was inscribed by translating the substrate through the focal spot of the laser 21 times at a speed of 8 mm/s, with each scan laterally offset from the previous by 0.4 μm to produce a modified region ~ 8.4 μm square. The use of the multiscan technique allows symmetrical square waveguides to be manufactured so they can be brought together both horizontally and vertically to create a multimode waveguide.

To create a low-loss PD, the optimum design of the multimode section was determined. To this end a sample was written to determine the separation of the single mode waveguides to create a uniform multimode waveguide. The sample had an input of two uncoupled single mode waveguides horizontally separated, then brought together to form on output where they are overlapped. This is repeated, with the output waveguides increasingly separated until they are decoupled. The throughput of each of these couplers was determined with the optimum two-mode waveguide being the device with the highest and equal transmission from both input waveguides, with the closest separation. This process was repeated with vertically separated waveguides, and the optimum waveguide separation determined to be 8.4 μm centre-to-centre in both axes.

Fig 5.2 shows facet images of each device size for the input, multimode and slit sections of the device. These facets have been ground back, to remove any tapering and polished to provide an optical quality finish. Fig 5.3 shows mode images of each device size for the input, multimode and slit images taken at 1550 nm using a Hamamatsu InGaAs camera. The input end images were obtained by exciting the square multimode output with an SMF-28 fibre. As this does not fully and evenly illuminate the multimode core there is a distinct difference in the illumination achieved in the single mode end with some cores oversaturated and others unlit, however this does clearly show discrete single mode outputs as expected. The multimode and slit images were obtained by exciting one of the input waveguides with an SMF-28 fibre, hence a distinct mode pattern being observed in the images.

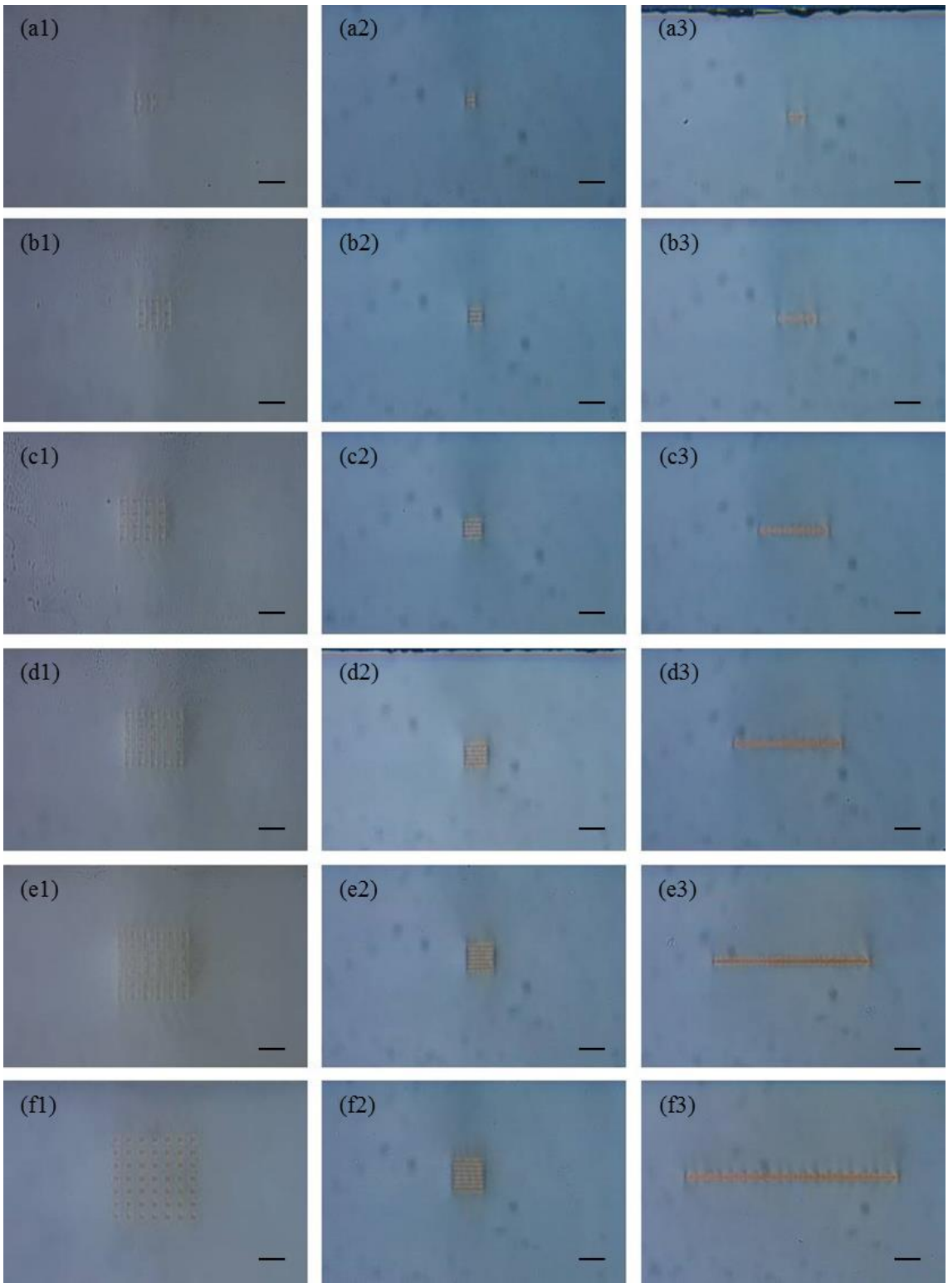

Figure 5.2 – Microscope images of the polished facets of the photonic dicer. Column 1 shows the input configuration, Column 2 the multimode configuration and Column 3 the slit configuration. Each row corresponds to the number of modes supported by the structure; Row a supports 4 modes; Row b, 9 modes; Row c, 16 modes; Row d, 25 modes; Row e, 36 modes and Row f supports 49 modes. The scale bar in each image represents 50 μm.

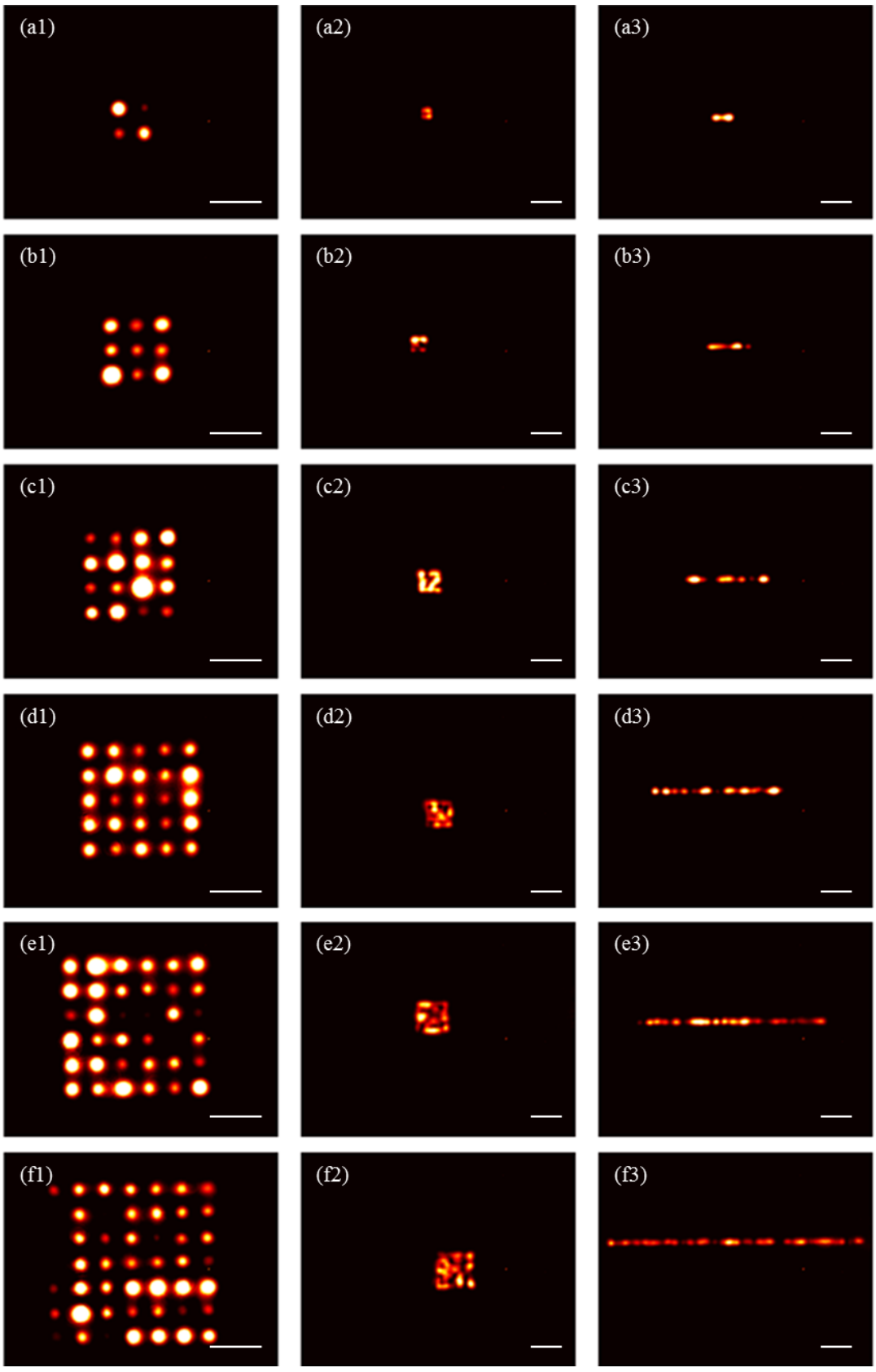

Figure 5.3 – Mode images taken on a Hamamatsu InGaAs camera with 1550 nm light. Column 1 shows the input configuration, Column 2 the multimode configuration and Column 3 the slit configuration. Each row corresponds to the number of modes supported by the structure; Row a supports 4 modes; Row b, 9 modes; Row c, 16 modes; Row d, 25 modes; Row e, 36 modes and Row f supports 49 modes. The scale bar in each image represents 50 μm.

5.2.3 Photonic dicer characterisation

The performance of the PD was tested in the laboratory by way of a cutback test. Initially the full device was investigated by using an SMF-28 fibre to excite each of the single mode ULI input cores with 1550 nm light and detecting the output from the multimode core on a Ge photodiode. The polarisation dependent loss (PDL) of each waveguide was investigated by using fibre paddles to alter the polarisation of the interrogating input to maximise and minimise the detected power. Each waveguides throughput is then calculated by comparing the power transmitted through it to the power delivered direct from the interrogation fibre. The overall performance of the device is calculated by averaging the throughput of each waveguide and the average throughput of all the waveguides. The 70 mm chip was then diced to a 40 mm length at the slit position, the facet was again polished and each waveguide remeasured. The 30 mm, PD2 diced off section of sample is a slit-to-MM dicer and its performance is determined by comparing the output of the 70 mm device to the 40 mm device. The full device is finally diced to a 10 mm length, re-polished and measured one final time. The removed 30 mm PD1 section contains a MM-to-slit dicer, and its throughput calculated by comparing the output of the 40 mm device to that of the 10 mm device.

Throughputs for each input waveguide for the MM-to-slit and slit-to-MM dicer devices are shown below (Fig 5.4 for the 4, 9 and 16 mode devices, and Fig 5.5 for the 25, 36 and 49 mode devices). In the left column are the MM-to-slit PD1 devices and the right column are the slit-to-MM PD2 devices. The averaged throughput of each of the devices is shown in Fig 5.7, with the throughput of each device size being similar whether written in the MM-to-slit or slit-to-MM direction indicating that the single mode, multimode and slit sections of the device all support an equal number of modes. The overall throughput falls as the number of waveguides increases as expected due to the increasingly tighter bends required to construct the device. Figs 5.4 & 5.5 show that the throughputs of each input waveguide are more uniform for PD2 than PD1. This is due to PD2 being measured on a 70 mm substrate with a longer section of the device being MM, thereby ensuring greater mode mixing, however the overall throughput is similar.

The individual waveguides used to construct these devices were tested to be SM throughout the 1320 to 1580 nm spectral region. The full 4 mode device on the 70 mm long substrate was also measured for 1500 and 1580 nm light, with the throughputs equal

to that measured for 1550 nm light, so it can be expected the PD devices will perform with a similar performance across this range.

The throughput of the 36 mode MM to slit PD used on-sky in the following section was also tested in the laboratory using an identical 36 mode ULI inscribed MM waveguide to excite the input end of the MM-to-slit PD. A throughput of 66 % ± 3% for 1550 nm light was determined which is in broad agreement with the value reported for PD1.

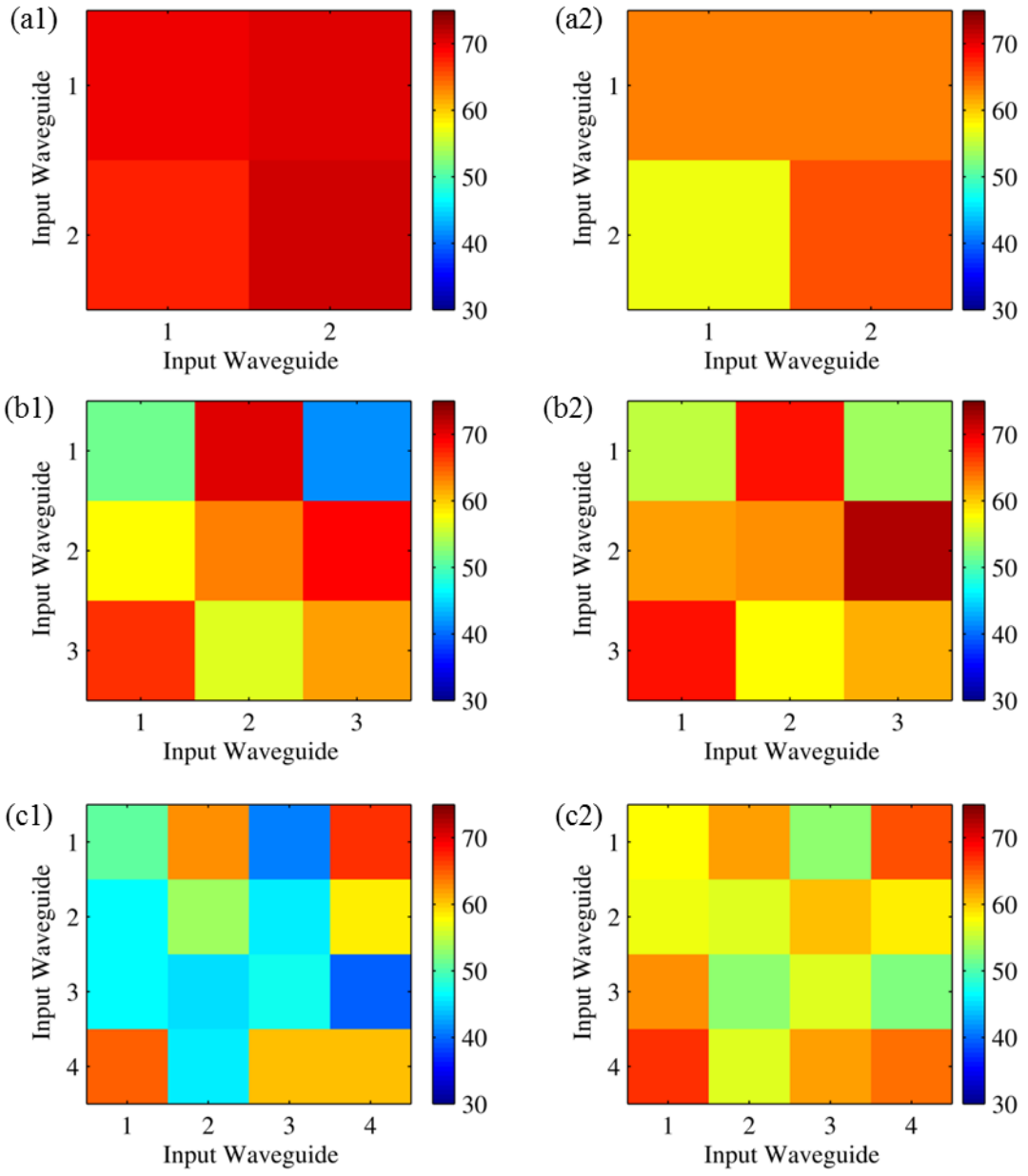

Figure 5.4 – Throughputs for each input waveguide in % for the photonic dicer. Column 1 shows the 10 mm to 40 mm MM-to-slit section of the full device (PD1), Column 2 shows the 40 mm to 70 mm slit-to-MM section of the full device (PD2). Row a is the 2 x 2, 4 mode device, Row b the 3 x 3, 9 mode device and Row c the 4 x 4 16 mode device.

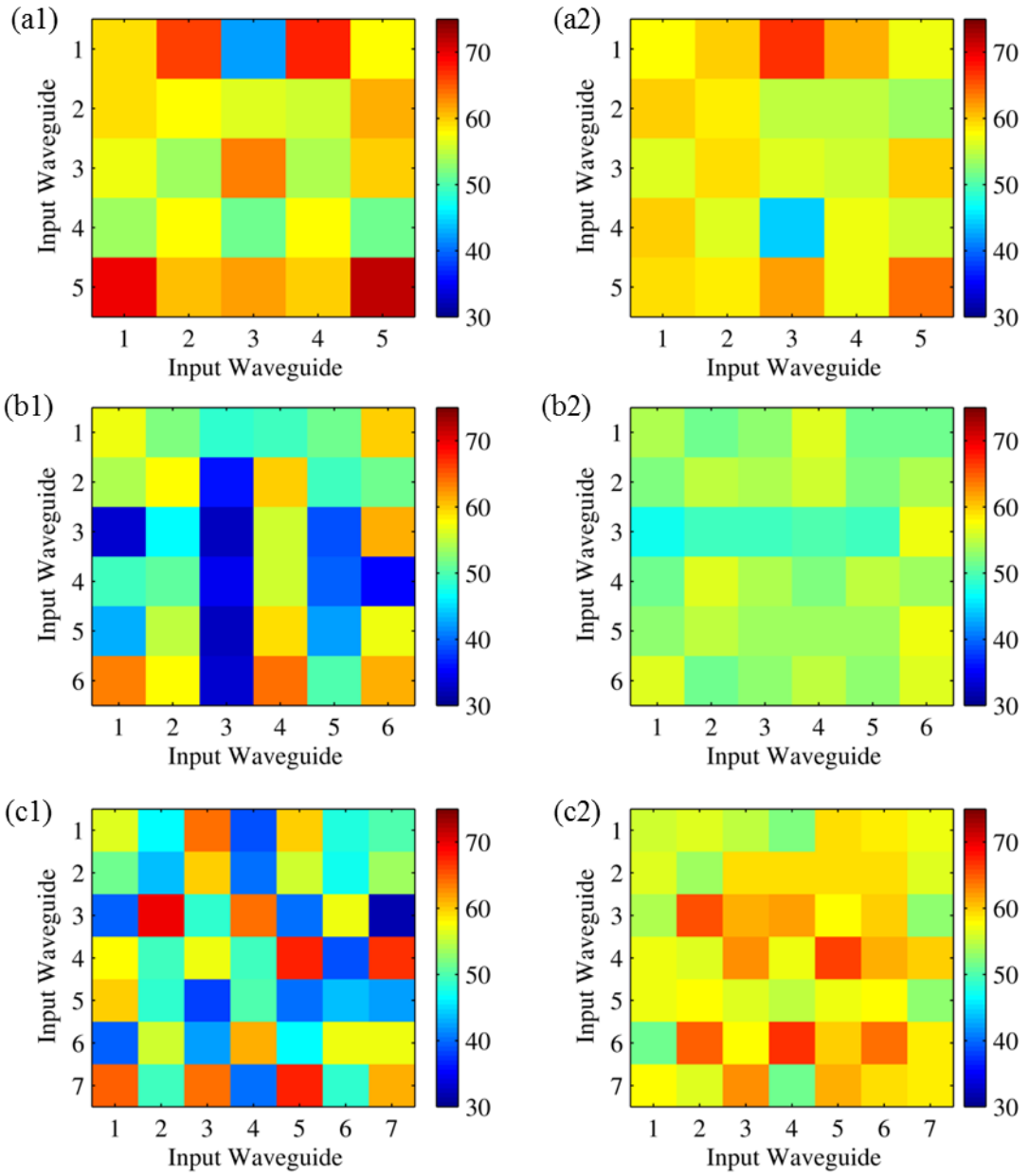

Figure 5.5 - Throughputs for each input waveguide in % for the photonic dicer. Column 1 shows the 10 mm to 40 mm multimode to slit section of the full device (PD1), Column 2 shows the 40 mm to 70 mm slit to multimode section of the full device (PD2). Row a is the 5 x 5, 25 mode device, Row b the 6 x 6, 36 mode device and Row c the 7 x 7, 49 mode device.

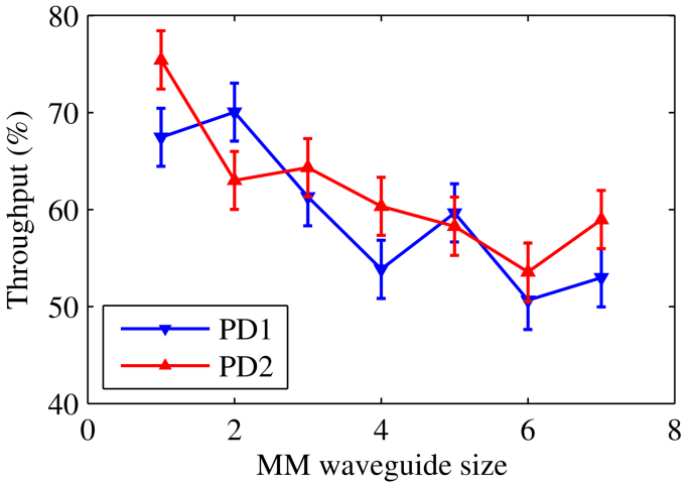

Figure 5.6 – Graph of averaged percentage throughput for the multimode to slit (middle section, PD1) and slit to multimode transition (end section, PD2). Horizontal axis indicates the K by K size of the input of the photonic dicer.

5.3 On-sky testing of photonic dicer

5.3.1 CANARY

The following section on the CANARY setup for the experiment is included for clarity, and was taken directly from Ref. [3] of which I was a joint first-author.

CANARY is an on-sky AO demonstrator system that was developed to investigate novel AO instrumentation and control techniques that will be required for the next generation of ELT AO systems [8]. For the work presented here, CANARY was configured to provide closed-loop AO correction using an on-axis natural guide star as the wavefront reference. Light with a wavelength >1000 nm was sent to the multimode entrance of the photonic dicer with visible wavelengths directed to a 36 sub aperture Shack-Hartmann Wavefront Sensor (WFS). The WFS measurements were used to drive a 56-actuator deformable mirror and separate fast-steering mirror which could provide a partially corrected PSF at a wavelength of 1500 nm. The WFS was placed behind the deformable mirror measuring the residual wavefront error after correction. The deformable mirror commands were calculated using a basic integrator feedback controller with a closed-loop gain of 0.3.

CANARY includes a range of sources that can be used when not on-sky to calibrate and optimize system performance. For our purposes, a 1550 nm laser was coupled into a single mode fibre and placed at the input focal plane of CANARY. Light from this calibration source passes through the CANARY optical train (including the deformable

mirror and fast-steering mirror) and the output PSF is reimaged onto the PD multimode entrance using the setup shown in Figure 5.7. The PSF at the multimode input of the PD was then modified by changing the surface shape of the deformable mirror to maximize the detected flux output at the pseudo-slit output. To modify the PSF, the AO-correction loop was engaged and static offset terms were artificially applied to the measured WFS signals. These offset terms were automatically adjusted through a process of simulated annealing [9]. The final WFS shape that provided maximum throughput was recorded and used as a reference for all subsequent on-sky operations.

CANARY was operated in three modes during data acquisition to investigate the PD performance under different degrees of AO correction. In closed-loop mode, CANARY provided correction of both tip-tilt and higher-order wavefront aberrations at an update rate of 150 Hz. Tip-tilt mode reduced the integrator loop gain on the high-order modes to a small value (typically 0.001). In this way only tip-tilt was corrected, but the reference wavefront was maintained without providing high-order AO correction. Open-loop mode additionally reduced the gain on the tip-tilt correction to maintain the PSF in the reference location for optimum coupling without providing high-frequency AO correction.

5.3.2 Instrument design

The on-sky instrument was designed by Dr Tim Morris based on an initial proposal by Prof. Robert Thomson. The set-up, shown in Fig 5.7 consists of two arms, the primary experimental arm containing the photonic dicer and a reference arm, which splits off 10 % of the telescope PSF and reimages it directly onto the camera. The initial 200 mm focal length lens L1 collimates the CANARY input and fold mirrors FM1 and FM2 reflect the beam into our experimental set-up allowing full control of the input beam. A 90/10 beamsplitter (BS) reflects 10 % of the telescope PSF into the reference arm with lenses L7 (focal length 750 mm) and L8 (focal length 1000 mm) directly reimaging the telescope PSF onto the camera allowing real-time monitoring of the telescope input. L2 is an identical lens to L1 and refocuses the beam. Lenses L3 and L4 act as a telescope to focus the beam into the MM end of the photonic dicer. Lens L4 was a 2.97 mm focal length aspheric lens, while L3 was interchangeable to optimise the focal spot for each size of photonic dicer.

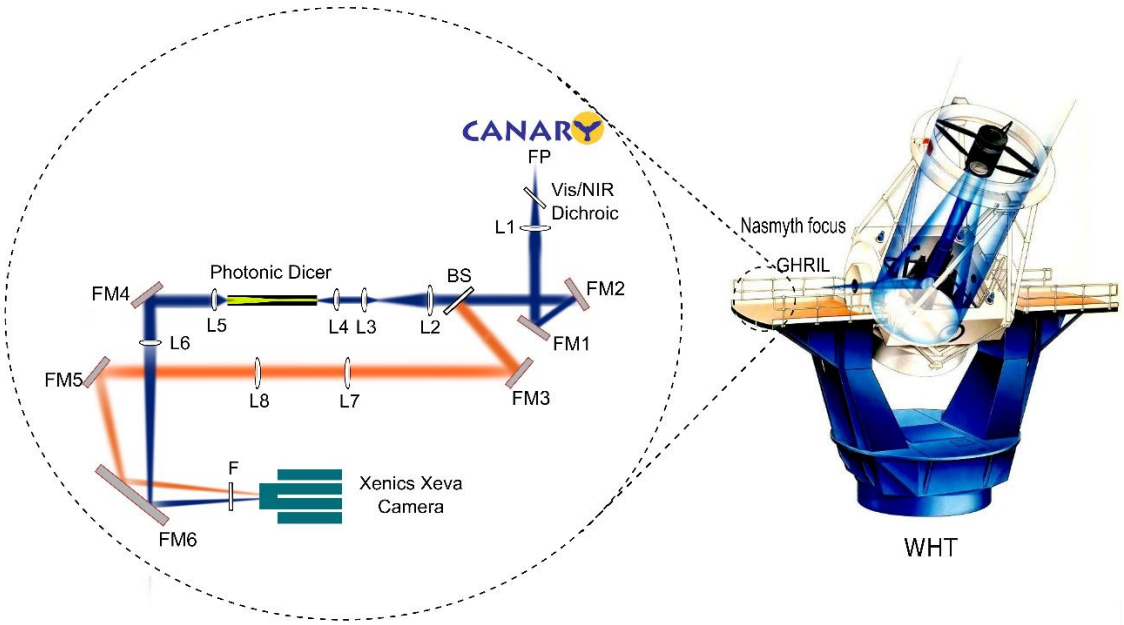

Figure 5.7 – Schematic of the on-sky experimental setup. Light is directed from the CANARY focal plane (FP), collimated by L1 and directed into the system (blue beam). The beamsplitter (BS) reflects 10% of the beam into the reference arm (orange beam) and is refocused onto the camera via L7 and L8. The remaining 90 % of the light is refocused by L2 and the telescope system L3 and L4 change the magnification to fit the input of the photonic dicer. Output light from the dicer is recollimated by L5 and focused onto the camera by L6. An H-band filter (F) is fitted in front of the camera. All fold mirrors in the system are for alignment. WHT image courtesy of the Isaac Newton Group of Telescopes, La Palma. Image adapted from one created by Debaditya Choudhury.

To accommodate the variable focal length of L3, the majority of the setup was mounted on a translating breadboard. The photonic dicer is mounted on a microblock and can be translated to focus the light into each device. Lens L5 (focal length 11 mm) collimates the slit output and L6 (focal length 200 mm) re-images the slit onto the camera. The Xenics InGaAs camera has an H-Band filter (F) in front to investigate wavelengths from 1450 nm to 1610 nm.

While testing the experimental setup on the bench it was found that changing the L3 lens and adjusting the breadboard to optimise the input coupling was time consuming. It was therefore decided that for the on-sky experiments a single dicer should be tested. As previously calculated, the CANARY PSF should support 25 spatial modes, and in order to allow for a margin of safety the 6 x 6 photonic dicer that supports 36 spatial modes was selected.

5.3.3 Data analysis

On-sky data was captured on the night of the 13th September 2013 at the WHT telescope in La Palma between 21:45 and 22:30 GMT. The star observed was TYC1052-3027-1 from the Tycho 2 catalogue [10], a third magnitude star in the astronomical H band. The astronomical seeing values, as measured using an on-site monitor [11], varied between 0.7 and 0.95 arcseconds over the course of the measurements, representative of median to poor seeing for the telescope site. Images were taken in data cubes capturing 100 images at a time, with a 400 ms integration time. The data taken from the Xenics camera is shown in Fig 5.8 a, although the signal can be seen it is not very clear due to the ~5000 intensity background counts and the hot and dead camera pixels. Throughout the experimental run periodic data cubes of dark images were captured, (Fig 5.8 b) and can be subtracted from the data image. The pixels surrounding the hot pixels are summed, averaged and used to replace the hot pixels to create a corrected image (Fig 5.8 c). The corrected image has the background centred around 0 and the vertical striations present in the camera removed, with no hot pixels, providing a much clearer image.

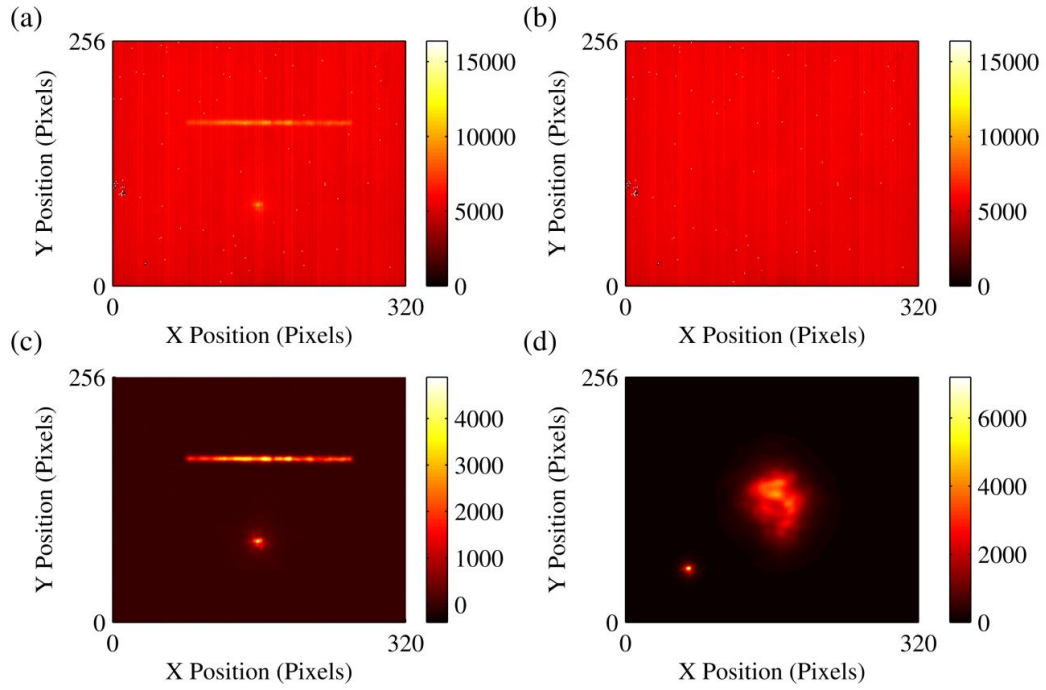

Figure 5.8 (a) Xenics camera image of the raw data, with the data visible but obscured by hot pixels and a high background. (b) Xenics camera image taken with the telescope PSF blocked to produce a background image. (c) Corrected data image with background removed and hot pixels averaged. (d) Corrected and averaged Xenics camera image of the reference with the photonic dicer removed and the CANARY PSF imaged directly onto the camera.

To calibrate the throughput of the device, the PD is removed from the system and L5 moved to the focus of L4 in order to obtain a reference image on the camera (Fig 5.8 d). Both the data image and the reference image have the spot from the reference arm present in the image. By summing the total flux in the slit and normalising it to the flux in the reference arm spot and repeating the procedure for the reference image we have calibrated values. The throughput of the photonic dicer is then calculated by using the value from the reference image as the input and the value from the data image as the output.

5.3.4 Throughput results

The performance of the photonic dicer was tested for all three CANARY AO modes, with averaged, corrected images shown in Fig 5.9 for closed-loop (a), tip-tilt (b), and open-loop (c) operation. The photonic dicer throughput was calculated for each image and histograms of the data for each AO mode presented in Fig 5.9 d-f. The average throughput of the dicer in closed-loop operation was 19.5 % ± 2 %. In tip-tilt operation the throughput was 9 % ± 2 % and in open loop mode the throughput was 10.5 % ± 2 %. Tip-tilt and open-loop operation result in very similar performance of the dicer. Theoretically open-loop performance should result in the worst PSF and hence the worst throughput, however worsening atmospheric turbulence resulted in the throughput of open-loop operation being higher than that in tip-tilt operation. The AO system operating with full correction doubles the throughput of the device. The on-sky throughput of 20 % is much reduced from the 66 % achieved in the lab, most likely due to a poor matching of the CANARY PSF input to the PD input.

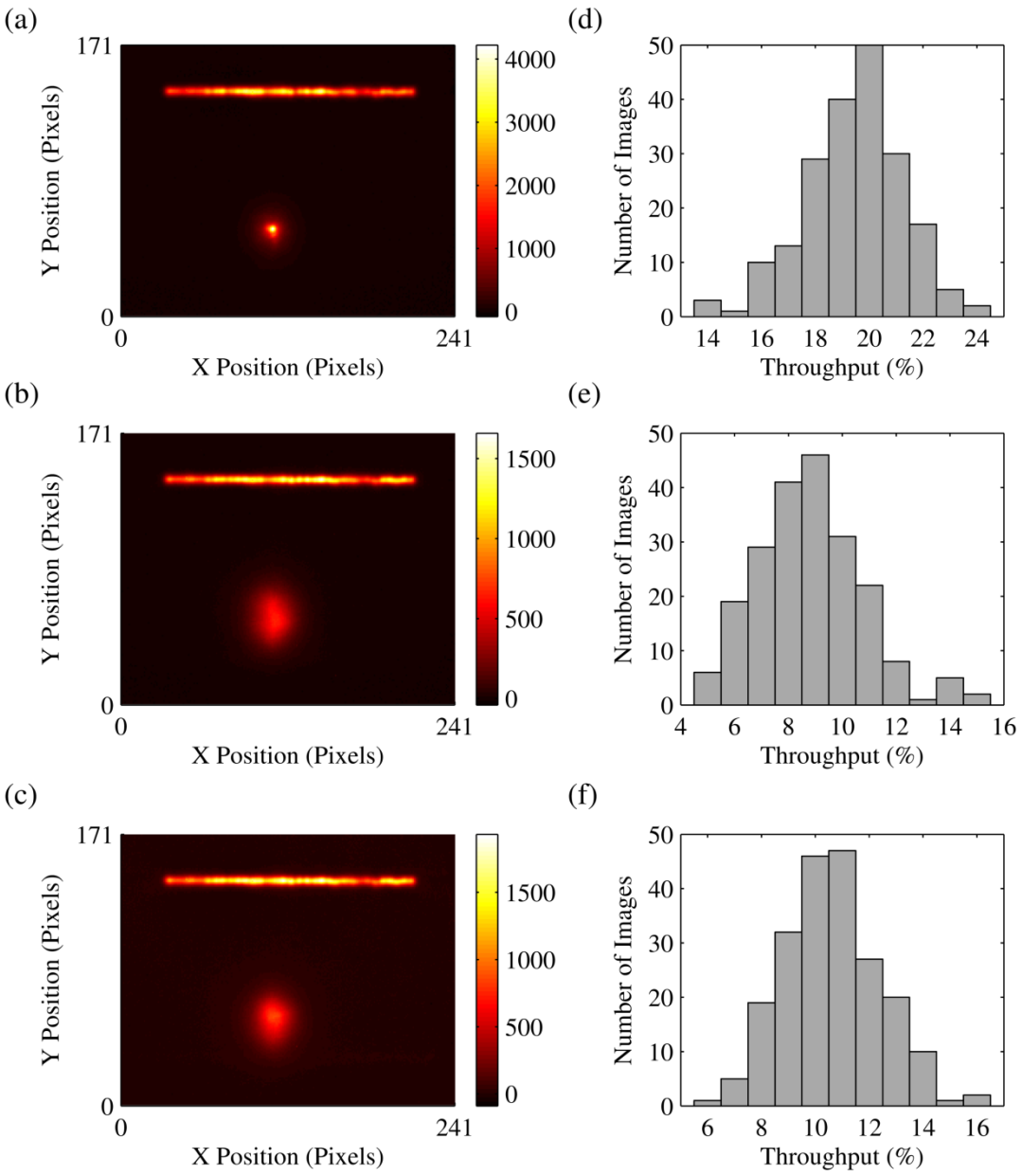

Figure 5.9 – Corrected, averaged image of the photonic dicer taken with CANARY operating in; (a) closed-loop, (b) tip-tilt and (c) open-loop operation. For clarity different intensity scales were used for each image. Histograms of photonic dicer throughput of each image for; (d) closed-loop, (e) tip-tilt and (f) open-loop operation.

5.3.5 Slit straightness

To act as an ideal input to a spectrograph the slit must be perfectly straight and uniform. This was tested by examining the on-sky data and taking each column of the camera data across the slit and fitting a curve to the data points (Fig 5.10 a). The centre point of this

fit can then be determined and plotted, performed for each column and repeated for several data frames. A straight line was plotted to these central positions and subtracted off to remove any overall tilt simply due to either the sample or camera being slightly off axis. There is a slight error in the slit centring from 0.2 to - 0.4 pixels, however there are some large jumps in adjacent waveguide positions. This is due to the slit waveguides not being written in order from left to right to facilitate minimum bend radii.

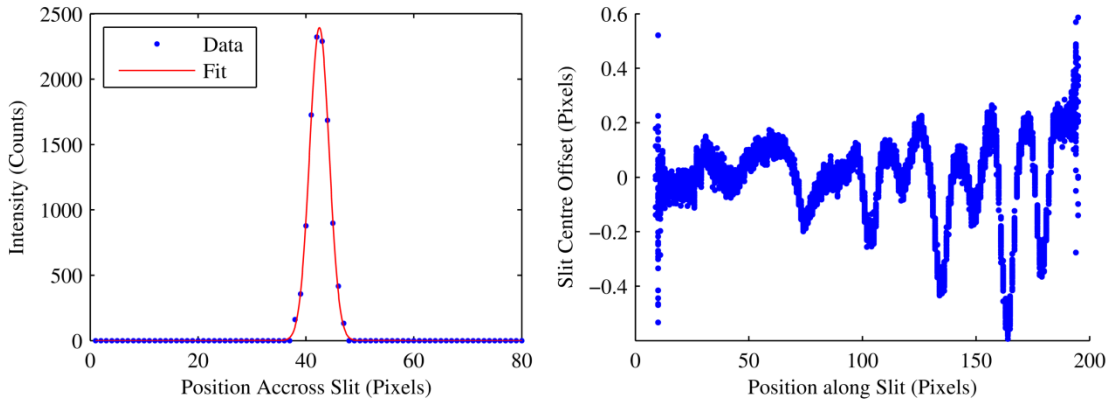

Figure 5.10 – (a) Plot of single column of data taken across the slit, with a Gaussian fit applied to locate the centre of the mode. (b) Plot of slit centre plotted against horizontal slit position, corrected for any angular tilt in the chip or camera.

5.4 Conclusions and future work

The photonic dicer device performs as designed transforming a multimode input into a slit output that is single mode in one direction and highly multimode in the other. Photonic dicers were inscribed that support 4, 9, 16, 25, 36 and 49 modes and the in-laboratory performance of the photonic dicer varied from 55 % to 70 % throughput for devices written and performing in both MM-to-slit and slit-to-MM directions. This clearly demonstrates that the multimode and slit end support the same number of modes as the separated single mode cores and the device performs equally in both directions. The throughput falls as the number of modes increases as expected, due to increasing bend losses. Photonic dicer performance was tested for orthogonal polarisations demonstrating little polarisation dependent loss. The performance of the 36 mode MM-to-slit photonic dicer was retested in the laboratory, providing a 66 % throughput for 1550 nm laser light. Laboratory tests demonstrating that the constituent waveguides are single mode from 1320 nm to 1580 nm. Additionally, the throughput performance does not vary from 1500 to 1580 nm indicating that the device performance should remain consistent over the on-sky measurement window of 1530 ± 80 nm.

The device was tested on-sky at the WHT with the assistance of the CANARY AO team under various modes of atmospheric correction. Closed-loop operation provides the maximum atmospheric compensation and produced a throughput of 19.5 %. Applying less AO correction with tip-tilt and closed-loop modes produced throughputs of 9 % and 10.5 % respectively.

The slit straightness was investigated and found to be relatively straight; however it is clear there are some thermal effects in the inscription setup and to improve the slit quality the slit waveguides should be written in order from one side to the other.

Several improvements can be made to increase the usefulness of the device for astronomy including:

(i) Ensuring the input of the photonic dicer is better matched to the CANARY input PSF to replicate in-laboratory throughputs on-sky.

(ii) Connecting the input of the dicer to a MM fibre, thereby separating the input and output alignment of the device. Many astronomical spectrographs are located in the basement of the telescope building for stability, with the telescope light delivered by way of optical fibre, so a fibre input dicer will be easily integrated into such an instrument.

(iii) Separating the lantern and reformatting functions of the device into separate sections to improve performance. It has been demonstrated that photonic lanterns made from MCF's can function with very low loss, this can be combined with a shorter ULI written chip to perform the slit reformatting function, thereby using each technology for its optimum performance.

(iv) Any future device should have the waveguides designed and written in an order such that the slit is constructed left to right in order to reduce thermal effects and improve the slit straightness, and improvements to the thermal stability of the laboratory.

5.5 Contributions

The initial proposal for the work came from communication and collaboration between Prof. Robert Thomson of Heriot Watt and Dr Jeremy Allington-Smith and Robert Harris of Durham University.

The device design came from discussions between Prof. Thomson, Robert Harris and David MacLachlan, with the final design by David MacLachlan and led by Robert Harris.

These designs were entered into software developed by Dr Graeme Brown of Heriot Watt to define the stage movements and produce the required G-code programs.

David MacLachlan designed, set up and aligned the ULI setup, the same one used in the volume grating work described in Chapter 4. David MacLachlan took the lead in the ULI inscription of the devices and the iterative process to determine the optimum waveguide parameters working together with Robert Harris.

David MacLachlan performed all lab characterisation of the photonic dicers including the full cut-back measurements of the devices.

The initial on-sky test setup came from an idea by Prof. Thomson with the final design contributed to by Robert Harris and David MacLachlan and led by Dr Tim Morris of Durham University who simulated and tested the design in Zemax.

The setup and tests at the telescope were performed by David MacLachlan, Robert Harris, Prof. Thomson, Dr Debaditya Choudhury and Dr Morris, who was key in the integration of the experiment to the CANARY AO system. The data capture software used on-sky was developed by Dr Alistair Basden from Durham University.

The code to determine the on-sky throughput of the device and the straightness of the slit was developed by David MacLachlan. This was also independently performed by Robert Harris to ensure confidence in the result. All values and images presented here for the on-sky performance were obtained from the code of David MacLachlan.

5.6 References

[1] J. Bland-Hawthorn, J. Lawrence, G. Robertson, S. Campbell, B. Pope, C. Betters, S. Leon-Saval, T. Birks, R. Haynes, et al., "PIMMS: photonic integrated multimode microspectrograph," *Ground-based Airborne Instrum. Astron. III Proc. SPIE* **7735**, 77350N (2010).

[2] R. Thomson, T. Birks, S. Leon-Saval, A. Kar, and J. Bland-Hawthorn, "Ultrafast laser inscription of an integrated multimode-to-single-modes waveguide transition for astrophotonics," *CLEO/Europe EQEC 2011 Conf. Dig.*, JSIII2_2 (Munich, 2011).

[3] R. J. Harris, D. G. MacLachlan, D. Choudhury, T. J. Morris, E. Gendron, A. G. Basden, G. Brown, J. R. Allington-Smith, and R. R. Thomson, "Photonic spatial reformatting of stellar light for diffraction-limited spectroscopy," *Mon. Not. R. Astron. Soc.* **450**, 428–434 (2015).

[4] R. J. Harris and J. R. Allington-Smith, "Applications of Integrated Photonic Spectrographs in astronomy," *Mon. Not. R. Astron. Soc.* **428**, 3139–3150 (2013).

[5] I. Spaleniak, N. Jovanovic, S. Gross, M. J. Ireland, J. S. Lawrence, and M. J. Withford, "Integrated photonic building blocks for next-generation astronomical

instrumentation II: the multimode to single mode transition," *Opt. Express* **21**, 27197–27208 (2013).

[6] F. Vidal, É. Gendron, G. Rousset, T. Morris, A. Basden, R. Myers, M. Brangier, F. Chemla, N. Dipper, et al., "Analysis of on-sky MOAO performance of CANARY using natural guide stars," *A&A* **569**, A16 (2014).

[7] S. M. Eaton, H. Zhang, P. R. Herman, F. Yoshino, L. Shah, J. Bovatsek, and A. Y. Arai, "Heat accumulation effects in femtosecond laser-written waveguides with variable repetition rate," *Opt. Express* **13**, 4708–4716 (2005).

[8] R. M. Myers, Z. Hubert, T. J. Morris, E. Gendron, N. A. Dipper, A. Kellerer, S. J. Goodsell, G. Rousset, E. Younger, et al., "CANARY: the on-sky NGS/LGS MOAO demonstrator for EAGLE," *Adapt. Opt. Syst. Proc. SPIE* **7015**, 70150E (2008).

[9] S. Kirkpatrick, C. D. Gelatt, and M. P. Vecchi, "Optimization by Simulated Annealing," *Science* **220**, 671–680 (1983).

[10] E. Hog, C. Fabricius, V. V Makarov, S. Urban, T. Corbin, G. Wycoff, U. Bastian, P. Schwekendiek, and A. Wicenec, "The Tycho-2 catalogue of the 2.5 million brightest stars," *A&A* **355**, L27–L30 (2000).

[11] N. O'Mahony, "RoboDIMM — The ING's New Seeing Monitor," *Newsl. Isaac Newt. Gr. Telesc.* **7**, 22–24 (2007).

Chapter 6 – Development and on-sky testing of a hybrid reformatter for high-resolution spectroscopy

6.1 Motivation

In Chapter 5, the development and testing of the fully integrated photonic dicer component was discussed, where a ULI fabricated photonic lantern and slit reformatting component are combined on a single chip for diffraction-limited spectroscopy. The manufactured component demonstrated a laboratory throughput of 66 % and an on-sky throughput of 20 %. This component acted as a basic proof of principle for a ULI written photonic component for an integrated astronomical spectrograph, however for use in a practical instrument several improvements can be made. In order to aid their stability large astronomical spectrographs are generally situated in a thermally isolated laboratory separate from the main telescope room, as a result a low-loss method of sending the light from the telescope to the spectrograph is required. The optimum method for this is by way of multimode optical fibres, so any reformatter device should be easily integrated with a multimode fibre. The photonic dicer's throughput also reduced from ~66 % in the laboratory to ~ 20 % on-sky, indicating that a better match of the telescope PSF to the device input is required.

Recent work performed by the team at Macquarie University has demonstrated that integrated components, such as the photonic dicer, also suffer from an additional modal noise component when fed with a multimode fibre [1]. This modal noise comes from the fact that the near-field modal pattern observed from a multimode fibre is highly wavelength dependent. Indeed Redding and Cao [2] have demonstrated that the strength of this effect is sufficient to create a high-resolution low-loss spectrometer consisting solely of a multimode fibre and camera. In an integrated component such as the photonic dicer there is a discontinuity in the guided modes between the MMF and the MM input to the device, which results in an imperfect match of the two near-field patterns and hence a wavelength dependence of the whole device thereby generating this additional modal noise term in the acquired spectra.

MCF lanterns have been shown to be producible with very low losses [3] compared to lanterns produced by ULI [4]. A ULI written device that simply reformats the input light from an MCF into a slit, similar to the device originally developed by Thomson *et al.* [5] can therefore be shorter, reducing the losses incurred by this component. Combining an

MCF lantern with a ULI written slit reformatting component, combines the advantages of the particular strengths of both these techniques and it is anticipated that connecting these two single mode systems will avoid any modal noise processes. These “hybrid reformatters” have the potential to create a device suitable for astronomical applications (Fig 6.1).

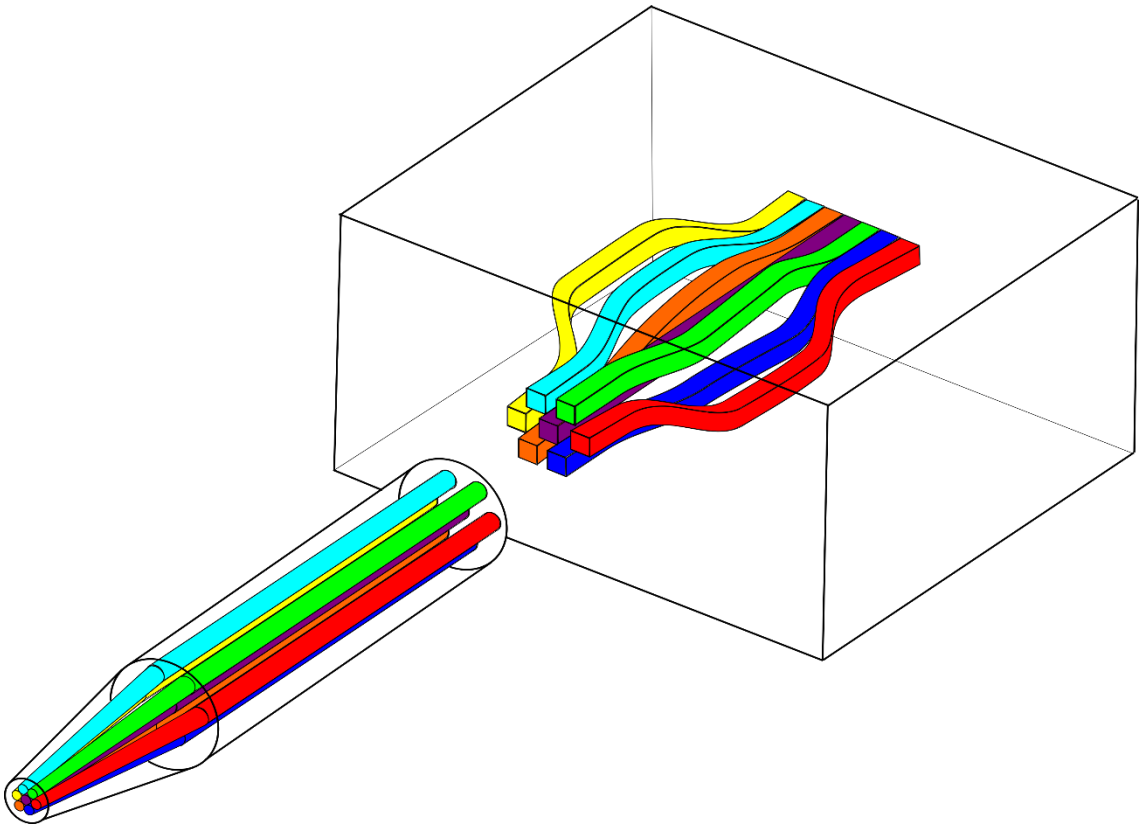

Figure 6-1. – Cartoon of simplified 7 core hybrid reformatter formed from an MCF lantern and a ULI reformatter.

6.2 Device development

6.2.1 MCF Lantern

The photonic lantern used for the hybrid reformatter is an MCF lantern designed and manufactured at the University of Bath by Dr Itandehui Gris-Sánchez. The MCF used contains solid cores in a solid cladding, with the cores designed to be well matched to standard SMF-28 optical fibre. The photonic dicer tested on-sky supported 36 modes, designed to couple the calculated 25 modes supported by the CANARY FWHM. To improve the matching of the mode number we considered the median seeing at the WHT, (0.7 arcseconds) and the shortest wavelength of the passband (1450 nm) to determine that the number of modes that form the uncorrected telescope to be ~ 60. To ensure better

matching to the telescope PSF it was decided to design the device support over 60 modes to demonstrate good device throughput. MCF lanterns are most easily constructed with a number of cores equal to a central hexagonal number, 7, 19, 37, 61, 91 etc. as such a 91 core MCF was used.

The base MCF was created by first drawing a commercially available step-index Ge-doped silica preform (NA = 0.11, diameter = 25mm) down into 1.8 mm diameter rods. These cores were inserted into thin-walled silica tubes and arranged into 5 hexagonal concentric rings around a central core, with a single core in the outer sixth ring to act as a marker. A standard stack and draw technique was used to manufacture a 243 µm diameter MCF with 9 µm diameter cores with a desired centre-to-centre separation of 17.32 µm (Fig 6.2 a). A cut-back measurement was performed on the MCF with the average attenuation at 1550 nm determined to be < 0.034 dB/m.

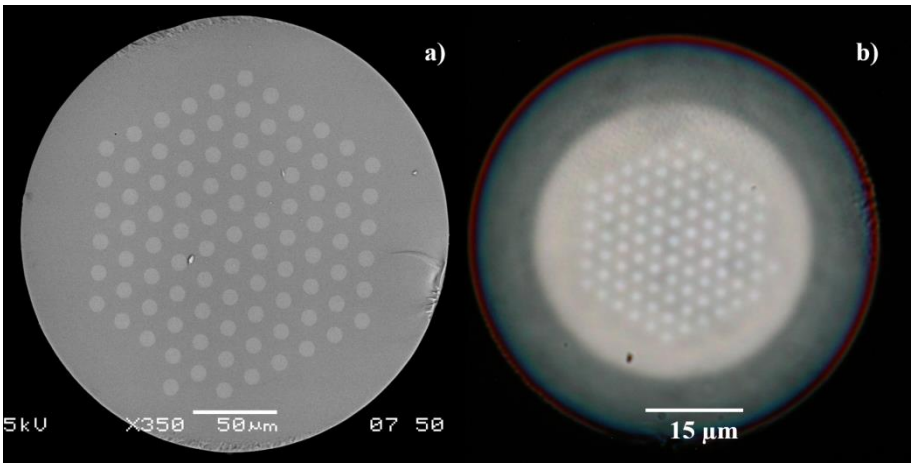

Figure 6-2 – (a) SEM image of the 92-core MCF, (b) Micrograph of the MM photonic lantern, the individual cores are still visible, with the darker shade surrounding the core being the F-doped cladding. Note the different scales for the two images. Image taken and provided by Itandehui Gris-Sánchez.

To create the photonic lantern transition one end of the MCF is inserted into a Fluorine doped silica capillary (NA = 0.22), which has a reduced refractive index compared to undoped silica. The F-doped capillary was then collapsed onto the MCF using an oxybutane flame. The structure is mounted in a fibre tapering rig, softened with the flame and stretched, forming a biconical fibre-like structure until the desired fibre diameter of 43 µm is reached. By cleaving the centre of the tapered waist the MM port is created (Fig 6.2 b). At this much reduced diameter, the single-mode cores become ineffective waveguides with the undoped silica surrounding the cores supporting the multimode system and the F-doped capillary acting as the cladding, this process is fully described in

[3] and [6]. Finally, the MCF lantern is secured in a glass capillary jacket to protect the fragile tapered end of the device. In order to achieve a low loss (< 0.5 dB) photonic lantern, the number of single mode cores must match the number of modes supported by the multimode end of the lantern. The multimode port diameter of 43 µm was chosen such that at a wavelength of 1550 nm the multimode port supports 92 modes, identical to the number of cores in the MCF. Several MCF lanterns were prepared and sent to Heriot Watt University.

6.2.2 ULI reformatter design

Recent research has shown that ULI waveguides written in Schott *AF45* glass can exhibit lower losses than those written in Corning *EAGLE 2000* glass due to fewer Fe^{2+} ions present within the material [7], as such AF45 was selected as the substrate for the new devices. The ULI setup used the Menlo laser and air bearing stages with a similar setup as described in Chapter 4. The laser was set to a repetition rate of 500 kHz, pulse duration of 350 fs with a right circular polarisation focused through a 0.4 NA lens. Many straight waveguides were inscribed and their loss measured when butt coupled to an SMF-28 fibre, with free space output coupling to identify the optimum multiscan parameters. The best waveguides written were constructed of 31 scans with a lateral separation of 0.2 µm between successive scans, a translation speed of 8 mm/s and a pulse energy of 174 nJ, resulting in a loss of 0.7 dB in a 15 mm long sample of AF45 glass. Viewing the inscribed waveguides under a microscope (Fig 6.3) a distinct modification region is seen, with a lighter square of positive refractive index modification, which supports the single mode light. Above this is a dark region of either damage, or negative refractive index modification, and finally above that a thin layer of lighter positive refractive index modification. These waveguides are lower loss than those used to construct the photonic dicer produced in Chapter 5, however these waveguides would be unsuitable to construct a photonic dicer device as they are unlikely to be able to be brought together vertically to form a multimode waveguide.

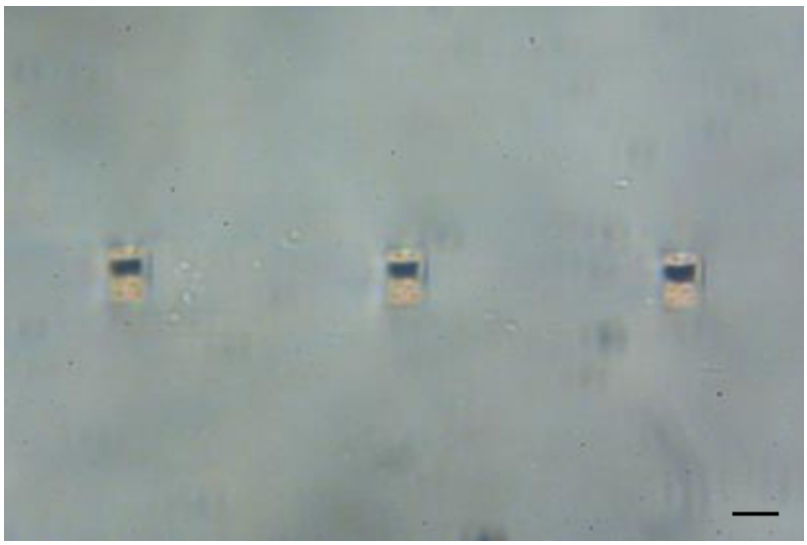

Figure 6-3 – Microscope image of polished chip facet showing three single mode waveguides. The lower lighter square below the rectangular black area supports the low-loss 1550 nm single mode. Scale bar represents 10 µm.

A set of 92 straight waveguides in the same pattern as the MCF (Fig 6.4 a) are inscribed with a centre-to-centre separation of 17.3 µm in order to confirm the correct dimensions had been used and the fibre matched well to the ULI chip. The initial tests demonstrated a poor match between the components and that the core separation of the MCF is larger in reality than that designed. Waveguides inscribed with a centre-to-centre separation of 17.6 µm demonstrate a good match to the MCF (Fig 6.4 b). In the final device a structure of 7 straight waveguides, the 6 corners and the alignment core (Fig 6.4 c), was inscribed 100 µm from the reformatter. This structure allows the MCF to be accurately aligned to the chip, as all 7 cores will only light up when the MCF and chip are correctly rotated and aligned. The chip can then be accurately moved 100 µm by the stages and only an optimisation of the horizontal and vertical axes are required to fully align the reformatter chip to the MCF lantern.

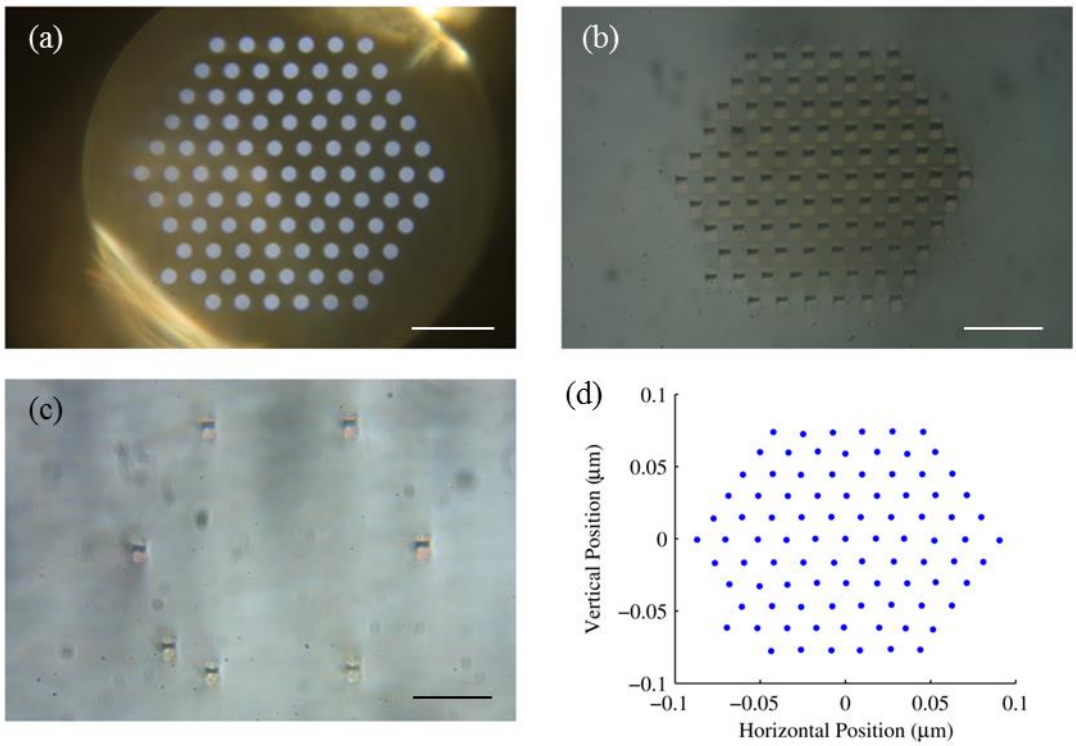

Figure 6-4 – (a) Microscope image of multicore end of the 92 core MCF lantern, with the extra alignment core clearly visible. (b) Microscope image of polished facet of ULI reformatter chip showing 92 core input. (c) Microscope image of polished facet of ULI reformatter chip showing 7 straight alignment waveguides. (d) Measured position of input waveguides to ULI reformatter chip. All scale bars indicate 50 µm.

The optimum order to write the hexagonal input of the reformatter is by inscribing the deepest waveguides first, this prevents the laser focus passing through modified material and producing less optimal waveguides. The bend radii of the waveguides must also be kept as large as possible in order to reduce loss, thus the optimum way to construct the device would result in the slit end of the reformatter not being inscribed in order from one end to the other (Fig 6.5). In a perfect inscription setup this may be possible, however temperature fluctuations in the lab cause the sample and inscription optics to expand and contract over the course of inscription ~ 3 hours, which resulted in very distorted slit, with many waveguides being uncoupled from their nearest neighbour (Fig 6.6 a).

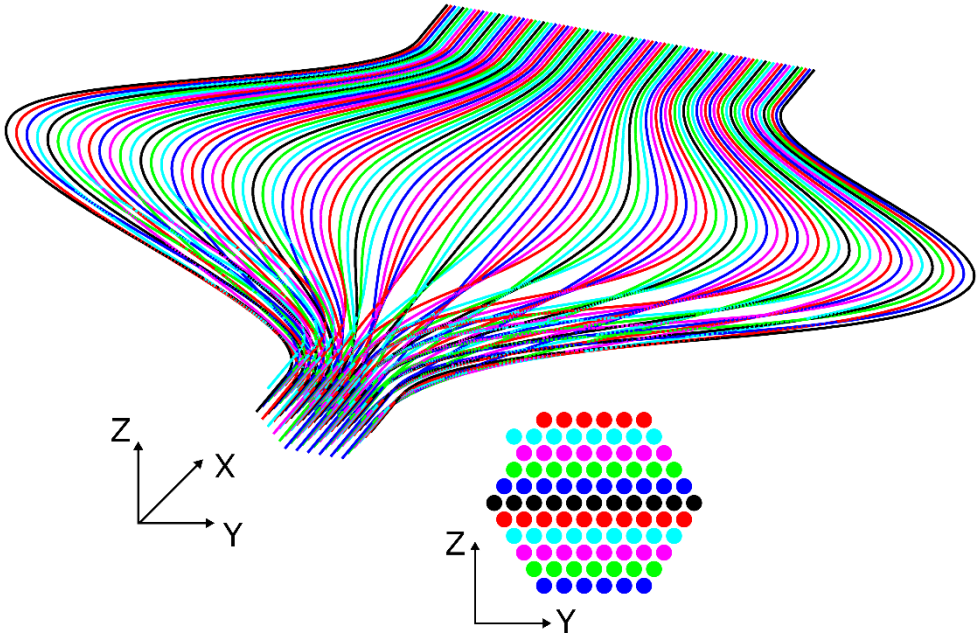

Figure 6-5 – Schematic of initial inscription geometry. The inset shows the design of the input to the dicer clearly, with the deepest waveguides written first in horizontal rows. As an example the row of black waveguides were written one after the other, however in the slit they are positioned far apart.

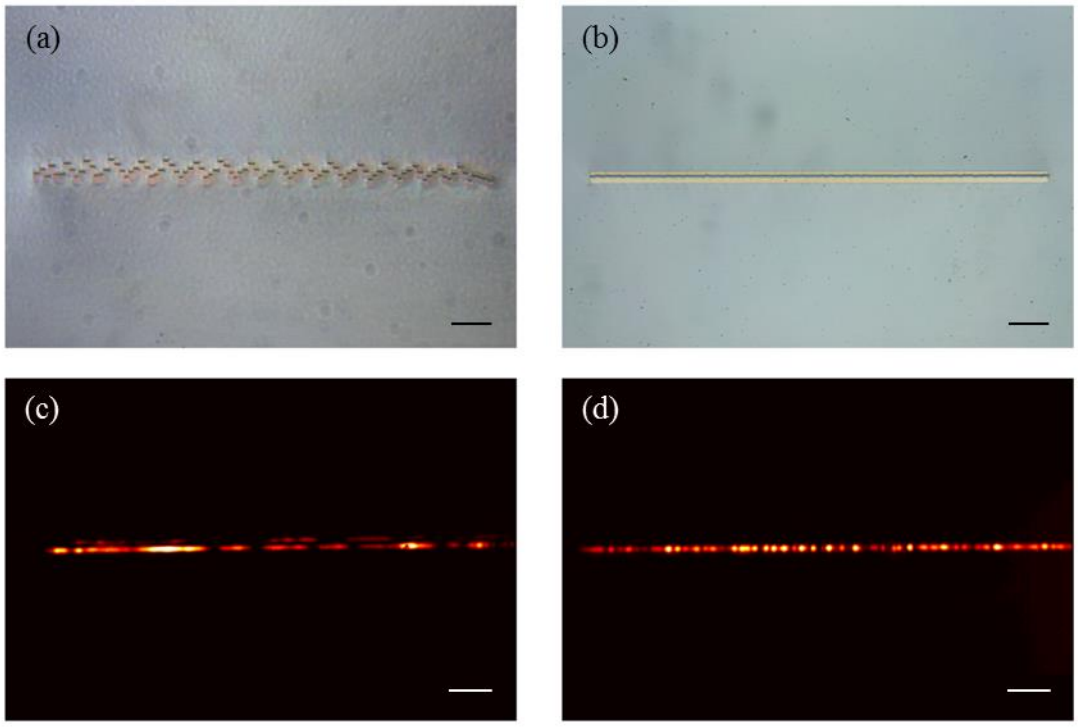

Figure 6-6 – (a) Microscope image of initial slit, written in a non-consecutive order and subject to significant thermal effects. (b) Microscope image of improved slit with waveguides written in consecutive order from right to left. (c) Mode image for 1550 nm light of a ULI reformatter constructed by the horizontal geometry showing a double slit with light supported in both positive refractive index modification regions. (d) Mode image for 1550 nm light of an improved ULI reformatter constructed by the vertical geometry demonstrating an improved slit supporting only a single mode in the vertical axis.

To produce a more uniform slit, the waveguides constructing it must be inscribed in order from one end of the slit to the other. As such, a new writing geometry was implemented whereby the hexagonal input end was written in order of horizontal layers starting with the deepest first and the slit from left to right (Fig 6.7).

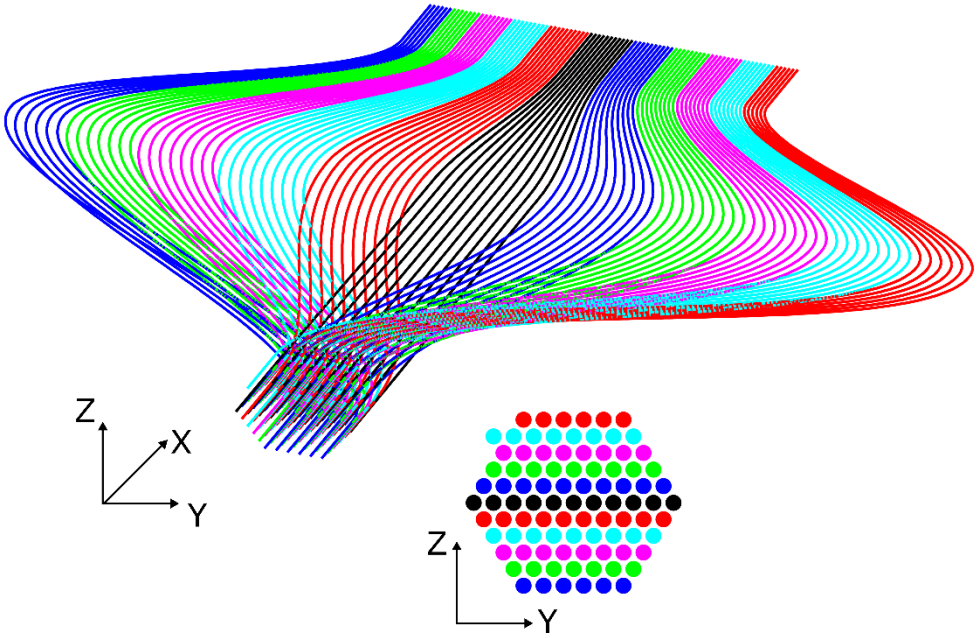

Figure 6-7 – Schematic of horizontal geometry for constructing the ULI reformatter. The inset shows the design of the input to the dicer clearly, with the deepest waveguides written first. As an example the row of black waveguides were written one after the other and in the slit they are positioned adjacent to each other.

This geometry has the effect of decreasing the bend radii of some waveguides and increasing losses. Imaged under the microscope the slit is clearly seen to be much improved, forming a slab waveguide (Fig 6.6 b). When butt coupling an SMF28 fibre to one of the input waveguides a double slit was clearly seen to exist (Fig 6.6 c) imaged on the Hammamatsu camera with 1550 nm light. This is theorised to be due to waveguides crossing over each other along the transitions and light being transferred from the desired square optimum area of positive refractive index change to the smaller area above the dark region. This result is undesirable and unsuitable as an input for a high-resolution spectrograph.

In order to prevent the light forming a double slit, without increasing the separation of the waveguides as they are reformatted into the slit, thereby greatly increasing bend losses a new reformatter geometry was investigated. In this case each column of the hexagonal input was inscribed from right to left, with each column inscribed in order of deepest

waveguide to shallowest, with the slit end still being inscribed in order from right to left (Fig 6.8). This vertical writing geometry also produced a very linear slit, and mode images demonstrated a single multimode slit output on the camera as desired (Fig 6.6 d).

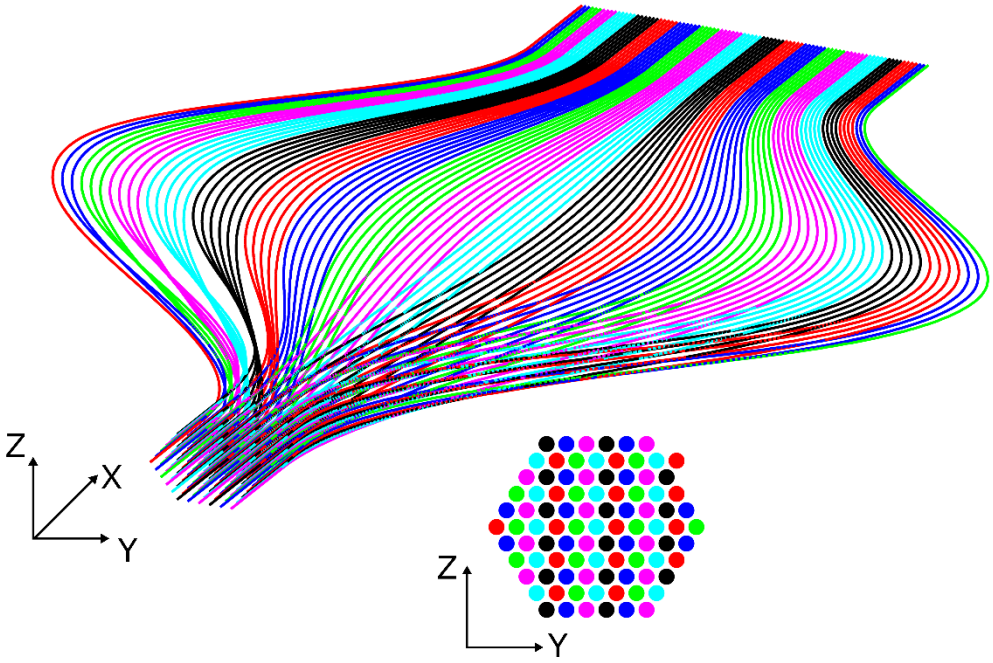

Figure 6-8 – Schematic of vertical geometry for constructing the ULI reformatter. The inset shows the design of the input to the dicer clearly, with the columns written in order from right to left with each column written in order from deepest to shallowest.

6.2.3 ULI reformatter characterisation

The reformatter was characterised with a 1550 nm laser using an SMF-28 fibre to measure the throughput of each of the 92 cores of the reformatter, with the average throughput being 67 % ± 2%, or 1.76 dB loss. Plotting the throughput of each waveguide against the horizontal position of the input waveguide shows a clear loss for all waveguides away from the centre of the structure (Fig 6.9 a). The minimum bend radii of each waveguide was calculated and plotted against its loss (Fig 6.9 b) and a clear trend is seen, demonstrating there is a significant increase in loss as the bend radius is reduced. In order to improve the throughput of the overall device the length of the device was increased in order to maintain the curvature below 0.05 µm/mm and keep each waveguide loss below ~1.2 dB.

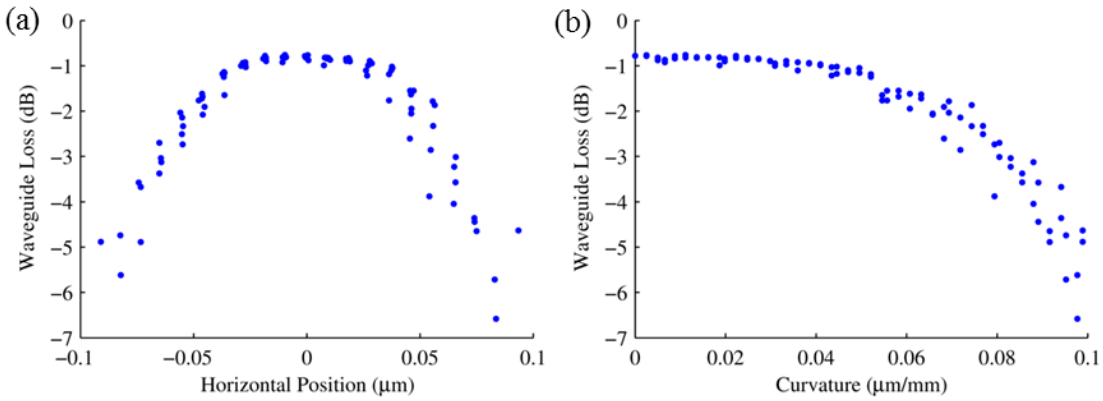

Figure 6-9 – (a) Plot of waveguide loss vs. the horizontal position of the input waveguides for a 15 mm long ULI reformatter written with the vertical geometry. (b) Plot of waveguide loss vs. the bend radii for a 15 mm long ULI reformatter written with the vertical geometry demonstrating a dramatic loss for any waveguides with a greater than 0.05 µm/mm bend radius.

The reformatter device was re-inscribed using the vertical geometry on a 30 mm long AF45 substrate. The single mode waveguides on this length of chip have a loss of 0.9 dB (throughput of 80 %). Overall, the average throughput of the reformatter device is 75 % ± 2%, or a 1.3 dB loss, an 8 % improvement on the 15 mm chip. By plotting the waveguide loss against the horizontal position of the input waveguide (Fig 6.10 a) it can be clearly seen that the loss on the right hand side is very low, but much higher on the left hand side of the device. This is not due to the bend losses but rather the fact that the left hand side waveguides are written using light that has propagated through previously modified material, aberrating the focal spot. A plot of waveguide loss vs. vertical position indicated no clear trend observed, demonstrating that waveguide depth had little effect on the measured loss. As only ~ 15 waveguides show a loss greater than 1.5 dB, and the overall average throughput of the device was 1.3 dB, close to the target maximum of 1.2 dB, this device was deemed acceptable for connectorisation to the MCF lantern.

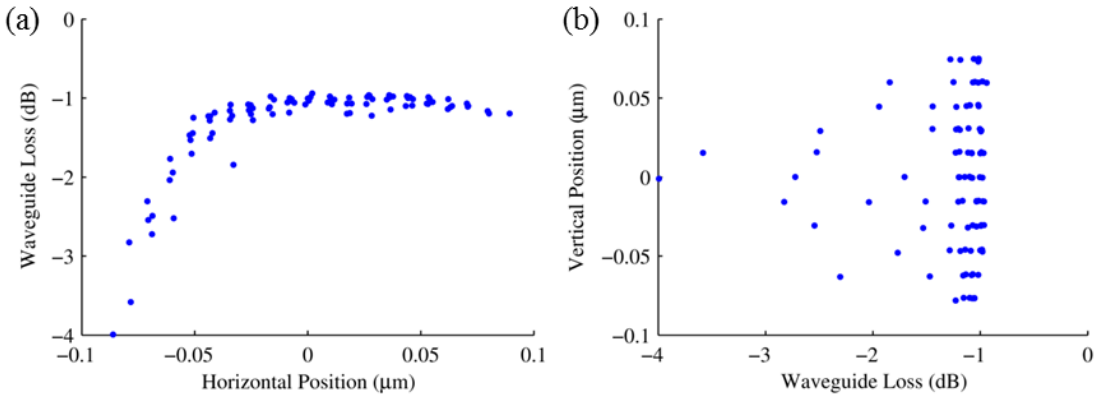

Figure 6-10 – (a) Plot of waveguide loss vs. the horizontal position of the input waveguides for a 30 mm long ULI reformatter written with the vertical geometry. (b) Plot of vertical position of the input waveguides vs. waveguide loss for a 30 mm long ULI reformatter written with the vertical geometry.

6.2.4 Hybrid reformatter assembly

In order to create the full hybrid reformatter device the MCF lantern must be permanently joined to the ULI reformatter chip. To ensure a secure connection, the fibre was mounted in a custom V-groove to provide a large surface area for the glue to adhere to. Dr Debaditya Choudhury manufactured the V-groove at Heriot Watt University, from a 9 x 5 x 1 mm fused silica substrate. The Menlo laser was used to provide 600 nJ, 350 fs pulses at a 500 kHz repetition rate with right circular polarisation, focused through a 0.4 NA lens. The substrate was mounted on the air bearing stages and rastored through the focus at a speed of 4 mm/s to build up a 200 µm wide hexagonal area of modification along the length of the substrate. The V-groove was soaked in a 5 % dilution Hydrogen Flouride solution for approximately 130 minutes to etch away the modified region to create a trench. The multicore end of the MCF lantern was secured in the V-groove (Fig 6.11 a) and glued in place using an ultraviolet cured adhesive (Norland NOA61). The facet was ground back (Fig 6.11 b) and aligned to the ULI slit reformatter device via the 7 alignment cores. The MCF lantern was glued to the reformatter chip with ultraviolet cured adhesive and the combined hybrid device placed on a hot plate for 2 hours to fully cure the adhesive and form a permanent bond (Fig 6.12).

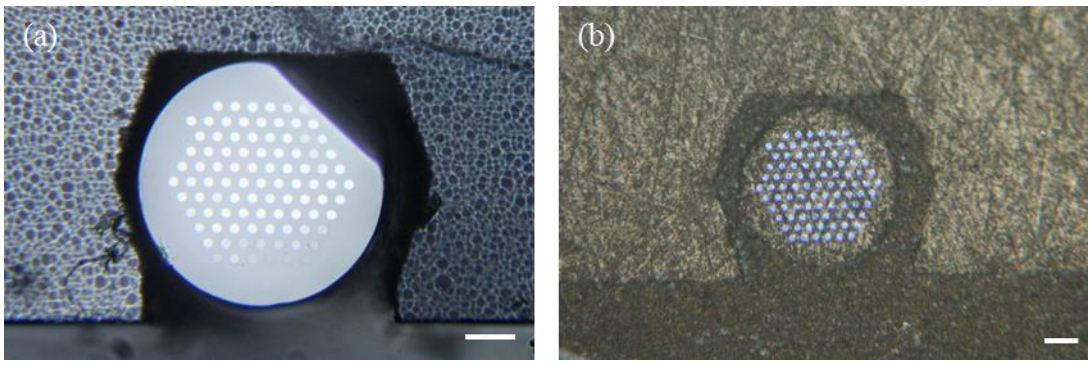

Figure 6-11 – (a) Microscope image of MCF lantern placed in the etched trench of the mounting chip. (b) Microscope image of glued up lantern and mounting chip, lantern illuminated by white light for clarity. The facet is ground back but not polished to aid adhesion of glue. Scale bars represent 50 µm.

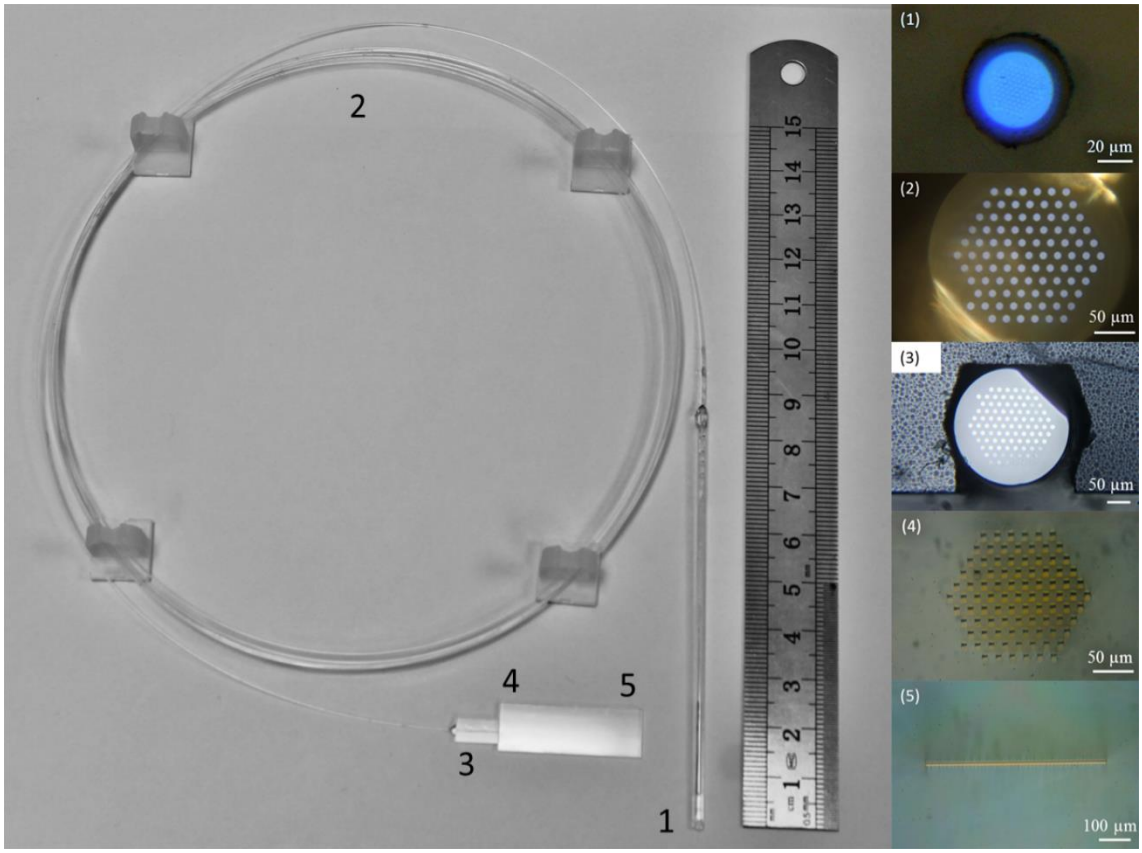

Figure 6-12 – Image of complete hybrid reformatter device showing: (1) the multimode MCF photonic lantern input; (2) MCF facet; (3) MCF in custom V-groove; (4) ULI reformatter input and (5) ULI reformatter output.

6.2.5 Hybrid reformatter characterisation

Dr Izabela Spaleniak tested the throughput of the hybrid reformatter in the laboratory at Heriot Watt University. A thermal white light source was focused into the multicore end

of an identical 92 core MCF lantern to that used in the hybrid reformatter to create an incoherent multimode output to use as a reference. The output from this lantern was used as the input to the hybrid reformatter and the output passed through a 1550 nm centred filter with a 40 nm bandwidth and measured on a photodiode, to determine the throughput of the device to be 69 % ± 2 %. A slit was present before the detector to ensure only light guided in the slit was measured. An image of the slit demonstrating an even illumination with all supported modes excited captured on an InGaAs camera is shown in Fig. 6.13.

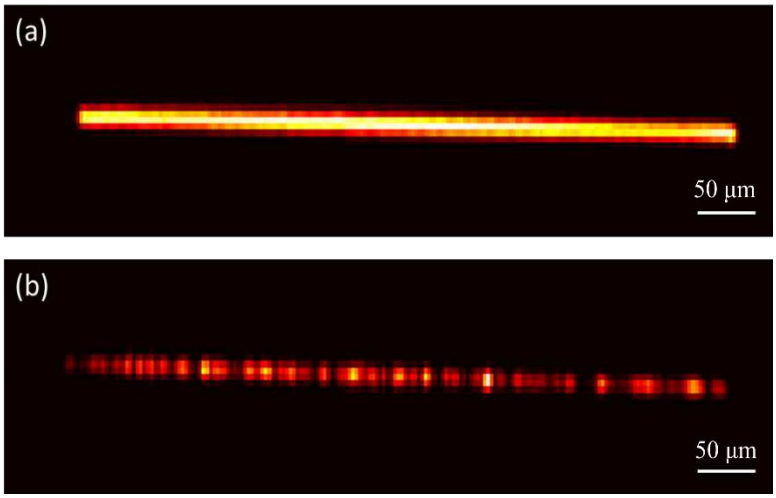

Figure 6-13 – Mode images of completed hybrid reformatter illuminated by filtered white light with a bandwidth of 40 nm centred around 1550 nm with the input injected with: (a) a multimode input and (b) a single mode input.

6.3 On-sky testing of hybrid reformatter

The device was tested on-sky at the 4.2 m William Herschel Telescope (WHT) in La Palma in collaboration with Dr Robert Harris, Dr Itandehui Gris-Sánchez and the CANARY team from the University of Durham and l'Observatoire de Paris in October 2015.

6.3.1 Instrument design

The on-sky experimental set-up was primarily designed by Dr Robert Harris from Durham University based on an idea by Prof. Robert Thomson and is shown in Fig 6.14. The set-up consists of three arms, the primary arm directs 9 % of the telescope light into the hybrid reformatter. The secondary arm directs 81 % of the light into an MCF lantern. The final arm directs 10 % of the telescope light directly onto the camera as a reference.

The percentage of telescope light in each arm was chosen in order to produce 3 images of equal intensity on the camera.

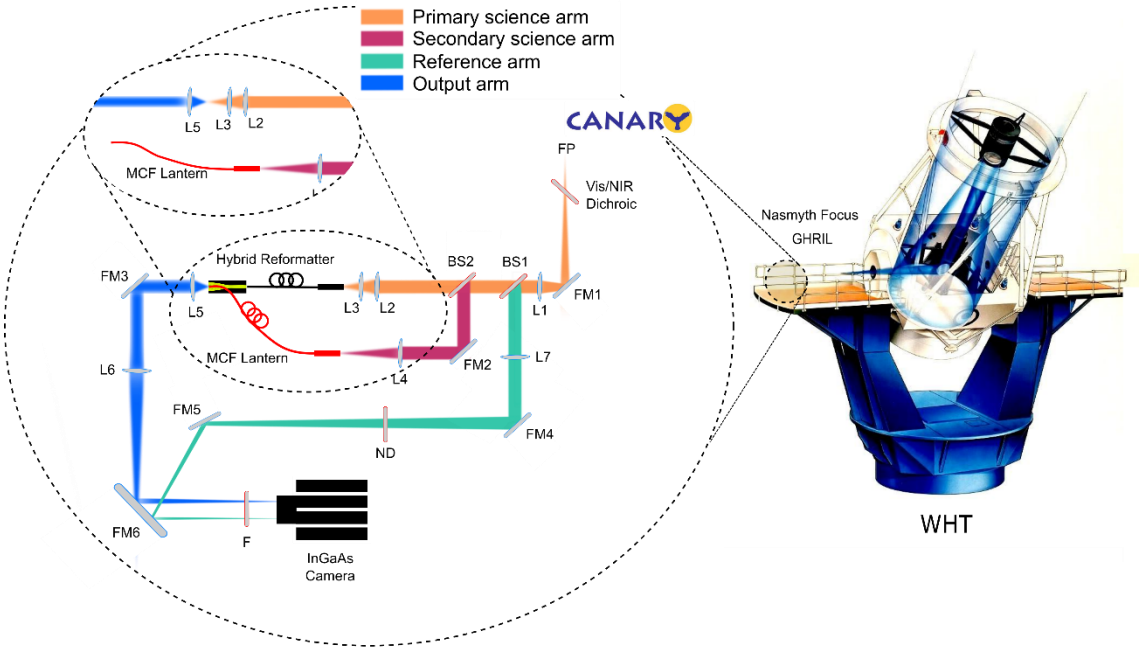

Figure 6-14 – Schematic of on-sky experimental set-up. Light is directed from the CANARY focal plane (FP), collimated by L1 and directed into the system (orange beam). The first beamsplitter (BS1) reflects 10% of the beam into the reference arm (green beam) and is refocused onto the camera via L7 through an absorptive 0.6 neutral density filter (ND) to ensure all the signals on camera are of similar intensities. A second beamsplitter (BS2) reflects 81 % of the light into a secondary arm focused into the multimode end of the 92 core MCF lantern by L4 (purple beam). The remaining 9 % of the light is injected into the multimode fibre end of the hybrid reformatter by the double lens system L2 and L3. The multicore end of the MCF lantern is placed on top of the ULI portion of the hybrid reformatter and the output of both are collimated by L5 and refocused onto the camera by L6 (blue beam). An H-band filter (F) is fitted in front of the camera. All fold mirrors in the system are for alignment. Inset shows hybrid reformatter removed from system and L5 moved towards L3 to reimage the PSF and gain a reference image. WHT image courtesy of the Isaac Newton Group of Telescopes, La Palma. Image adapted from one created by Debaditya Choudhury.

The initial lens, L1 collimates the input from the CANARY focal plane into each of the experimental arms. A 90/10 beamsplitter (BS1) reflects 10 % of the light into the reference arm and is refocused via L7 directly onto the camera to allow real time monitoring of the CANARY PSF and calibrate the throughput of the hybrid reformatter. The reference arm contains a 0.6 Neutral Density (ND) absorptive filter to ensure all arms of the experiment can be imaged on the camera without any being saturated. A 10/90 beamsplitter (BS2) reflects 90 % of the remaining light into the secondary arm and is

focused into the multi-mode end of an identical 92 core MCF lantern (the secondary lantern) as that was used to construct the hybrid reformatter, via lens (L4). This lens focuses the PSF to a large focal spot, so only the core can be coupled into the MCF lantern (angular size of secondary lantern input is 0.23 ± 0.01 arcseconds). This setup will demonstrate the power of CANARY as the throughput of the MCF will greatly improve with increasing AO correction. The remaining 9 % of the light passes directly through the beamsplitters and is focused into the multimode fibre end of the hybrid reformatter via lenses L2 and L3. The double lens setup focuses the entire PSF into the input of the hybrid reformatter (angular size of hybrid reformatter input is 1.1 ± 0.07 arcseconds). The multicore end of the MCF lantern in the secondary arm is cleaved and mounted on top of the ULI written slit end of the hybrid reformatter on a five axis alignment stage. Lens L5 collimates both outputs, with lens L6 to image these two devices simultaneously onto the camera. The hybrid reformatter and output of the MCF lantern were designed to be easily removed after on-sky data has been taken and lens L5 moved forward to re-image the telescope PSF directly to act as a reference to calculate the throughput of the dicer. The camera used was a Xenics (Xeva-1.7 320) camera, which combined with the H-band filter used provided a detection bandwidth of 1450 to 1610 nm (FWHM).

6.3.2 Throughput results

The device was initially tested on-sky on the night of 11th October 2015 between 20:30 and 22:45 GMT. The star observed was TYC 3156-2223-1 from the Tycho 2 catalogue, a 1st magnitude star in the astronomical H-band [8]. The astronomical seeing values, measured using an on-site monitor [9] varied between 0.5 and 0.8 arcseconds, representative of median seeing at the site. A Nelder-Mead simulated annealing algorithm was applied to maximise the throughput through the slit and determine the optimum deformable mirror shape that the CANARY system would correct to [10]. The hybrid reformatter was tested with CANARY operating in three different AO modes as before, described in Chapter 5.3.1. The data was corrected and analysed as before, fully explained in Chapter 5.3.3. Averaged images of closed-loop (a), tip-tilt (b) and open-loop (c) operation are shown in Fig 6.15. The image from the MCF lantern is distorted due to an imperfect cleave. In the case of open-loop correction the photonic dicer throughput was measured to be 48 % ± 5 %. With CANARY operating with tip-tilt correction the photonic dicer has a throughput of 47 % ± 5 %. When the system was providing full AO correction in closed-loop mode the throughput was measured to be

53 % ± 4 %. Histograms of the throughput data obtained for the three modes of AO operation are shown in Fig 6.15 d-f.

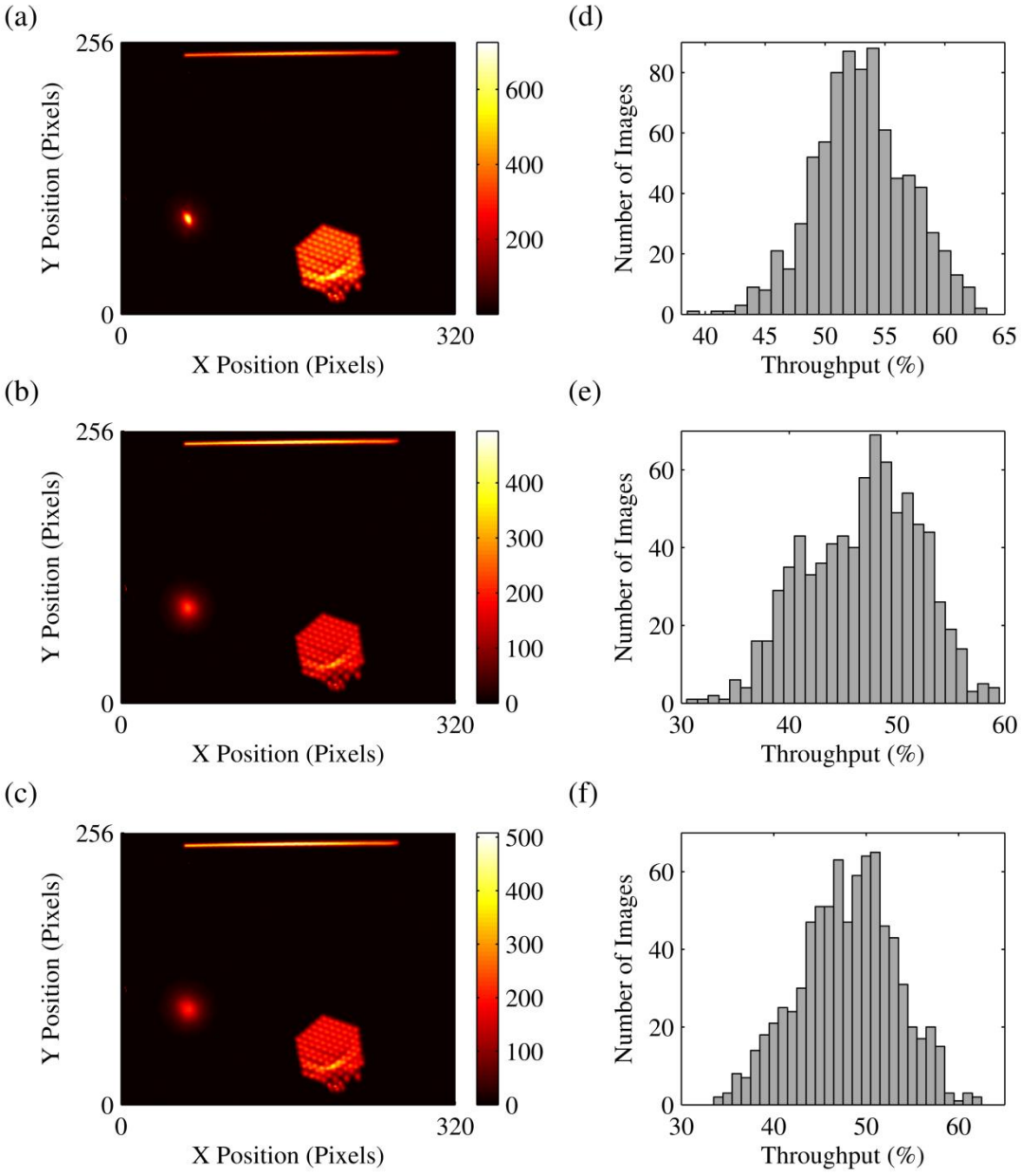

Figure 6-15 – Corrected, averaged image of the hybrid reformatter and MCF lantern taken with CANARY operating in: (a) closed-loop, (b) tip-tilt and (c) open-loop operation. Histograms of hybrid reformatter throughput of each image for: (d) closed-loop, (e) tip-tilt and (f) open-loop operation.

6.4 Dither

A second set of on-sky measurements were performed on the night of the 12th October 2015 between 20:30 and 22:45 GMT on the same star as the previous night. For these experiments the multicore end of the MCF lantern in the secondary arm is re-cleaved to improve the image. For this night the position of the CANARY PSF was moved with a series of 10 images taken for each position. The PSF was shifted to 121 positions in an 11 by 11 grid with the central position being similar to the tested position on the previous night. The experiment was performed for both closed-loop and tip-tilt operation of the AO system, with averaged corrected images of each AO mode shown in Figs 6.16 a & b. Figs 6.16 c & d show the closed-loop and tip-tilt total fluxes of the slit of the hybrid reformatter for each PSF position normalised to the maximum flux in the slit. Figs 6.16 e & f repeats this for the total flux in the MCF lantern in the secondary arm for each position, normalised to the maximum flux in the MCF lantern. Closed-loop operation produces a 38 % improvement in performance over tip-tilt operation for the MCF lantern compared to a 15 % improvement for the hybrid reformatter. The hybrid reformatter is relatively insensitive to the position of the PSF input compared to the MCF lantern. The optimum position of the PSF is off centre for the MCF lantern as the PSF was not correctly positioned with the simulated annealing algorithm for this experimental arm.

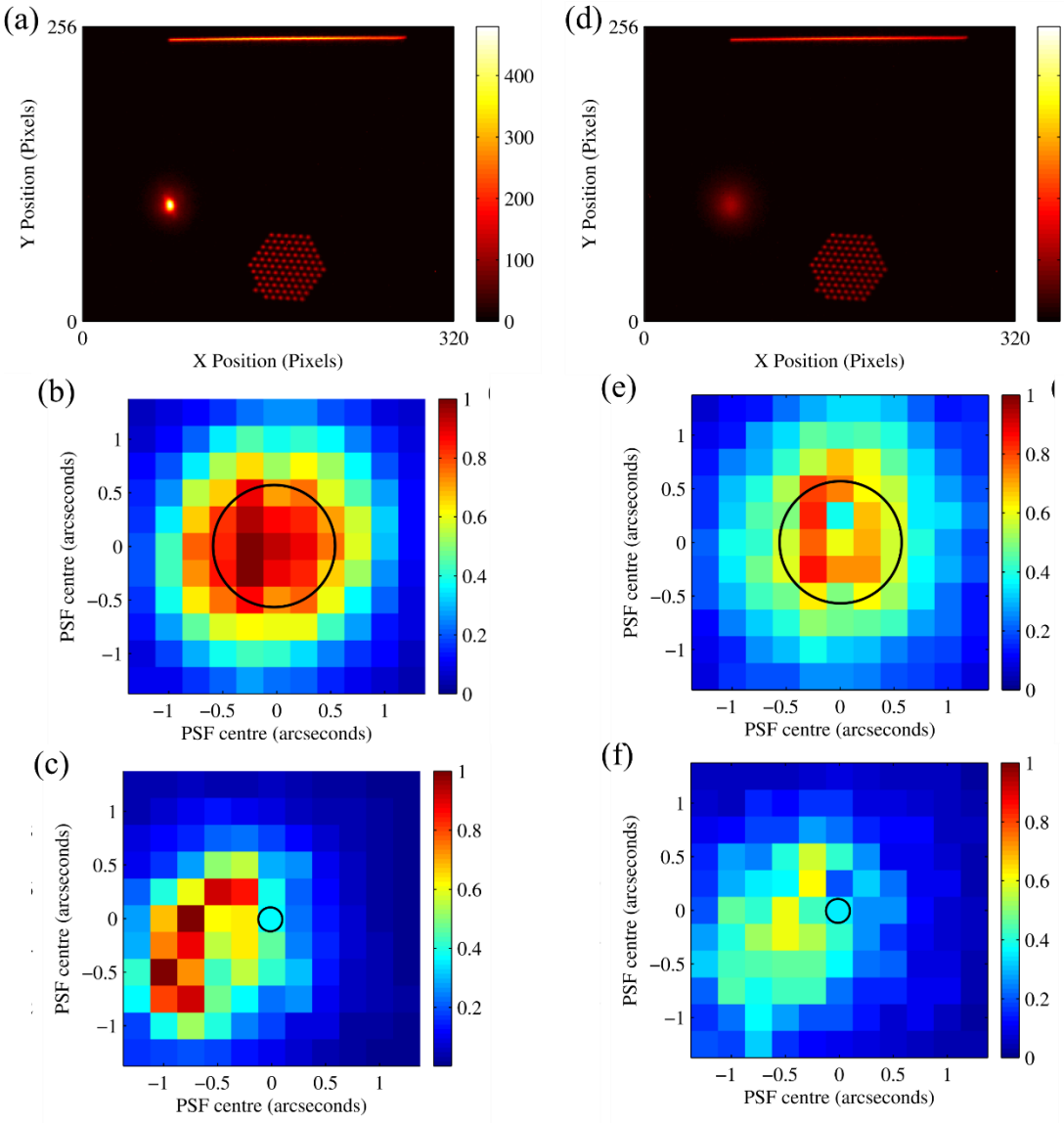

Figure 6-16 – Corrected, averaged image of the hybrid reformatter and MCF lantern taken with CANARY operating in; (a) closed-loop and (d) tip-tilt operation. Hybrid reformatter slit flux for; (b) closed-loop and (e) tip-tilt operation normalised to the closed-loop slit flux for different positions of the CANARY PSF input. MCF lantern flux for; (c) closed-loop and (f) tip-tilt operation normalised to the closed-loop MCF flux for different positions of the CANARY PSF input. The black circles represent the angular size of the input fibre in each science arm.

6.5 Slit straightness

6.5.1 On-sky analysis

The straightness of the slit was analysed as described in Chapter 5.3.5, by fitting a Gaussian to each vertical column of the image and locating the peak centre. This was performed for 100 images and plotted in Fig 5.17. The overall accuracy of the slit centre position was + 0.3 to – 0.4 pixels, similar to that achieved in the photonic dicer, however

with the slit being written from right to left, the positioning of each adjacent waveguide is much improved. The increase in the right hand side of the image is believed to be due to an edge effect of the final written waveguide. The MFD of the slit was also calculated as the FWHM of the signal and plotted as the blue lines in Fig 6.17. As can clearly be seen there is some variation in the central position and a clear increase in mode size along the slit. Due to the length of the slit and the magnification required to ensure the entire slit is imaged there were very few data points across the slit (~ 3 to 4) and as such these measurements have quite a large uncertainty.

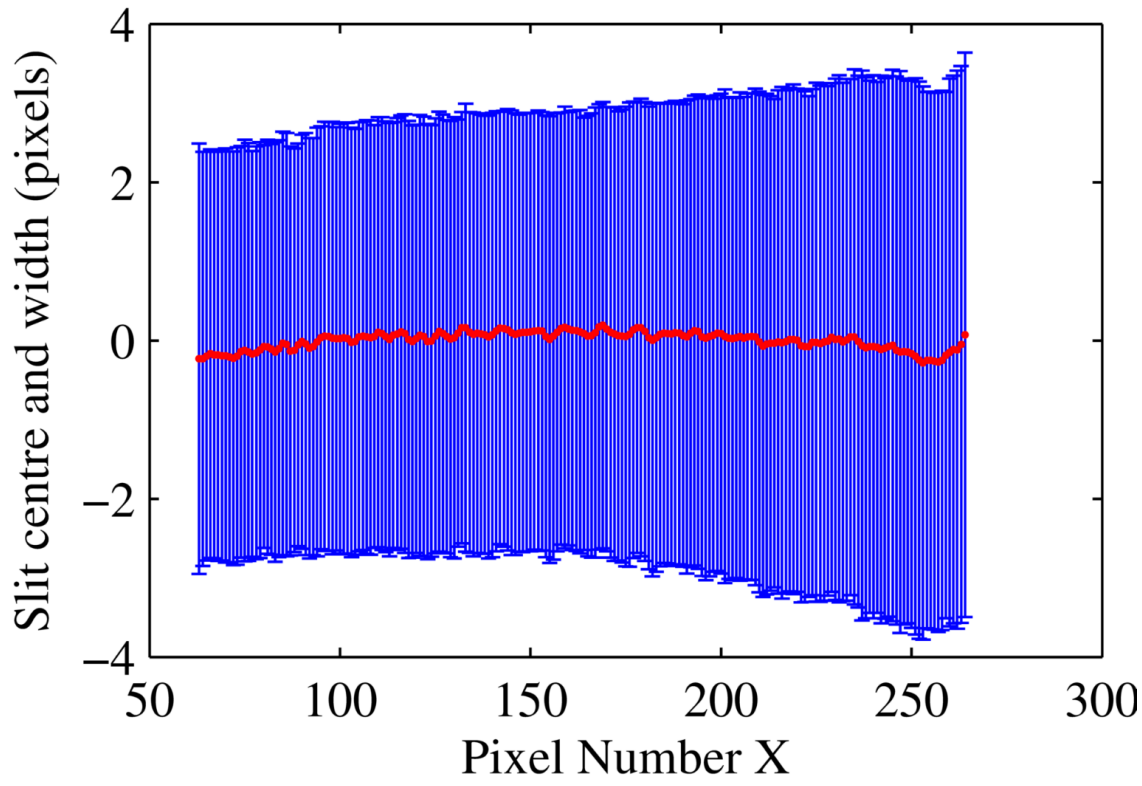

Figure 6-17 – Plot of slit centre (red line) plotted against horizontal slit position, corrected for any angular tilt in the chip or camera. Blue bars represent the FWHM of the slit at that position

6.5.2 Laboratory analysis

To perform a more accurate analysis of the slit straightness and device performance, Dr Izabela Spaleniak carried out further tests in the laboratory at Heriot Watt University. A 76 μm long section of the slit was imaged, and 1550 nm light injected into the MM end of the hybrid reformatter using an SMF-28 fibre at three different input positions (Fig 6.18). To ensure an evenly illuminated slit, the MCF was gently agitated while 800 frames of data were obtained on a Hamamatsu InGaAs C10633 camera with an integration time of 20 ms. The average MFD of the slit was 8.4 μm at the $1/e^2$ point.

Across the analysed length the slit centre was measured to vary by 0.7 μm and the MFD width varied by 0.5 μm. Variation in the slit centre position and width was relatively small as the injection position was changed, varying by 0.07 and 0.12 μm respectively.

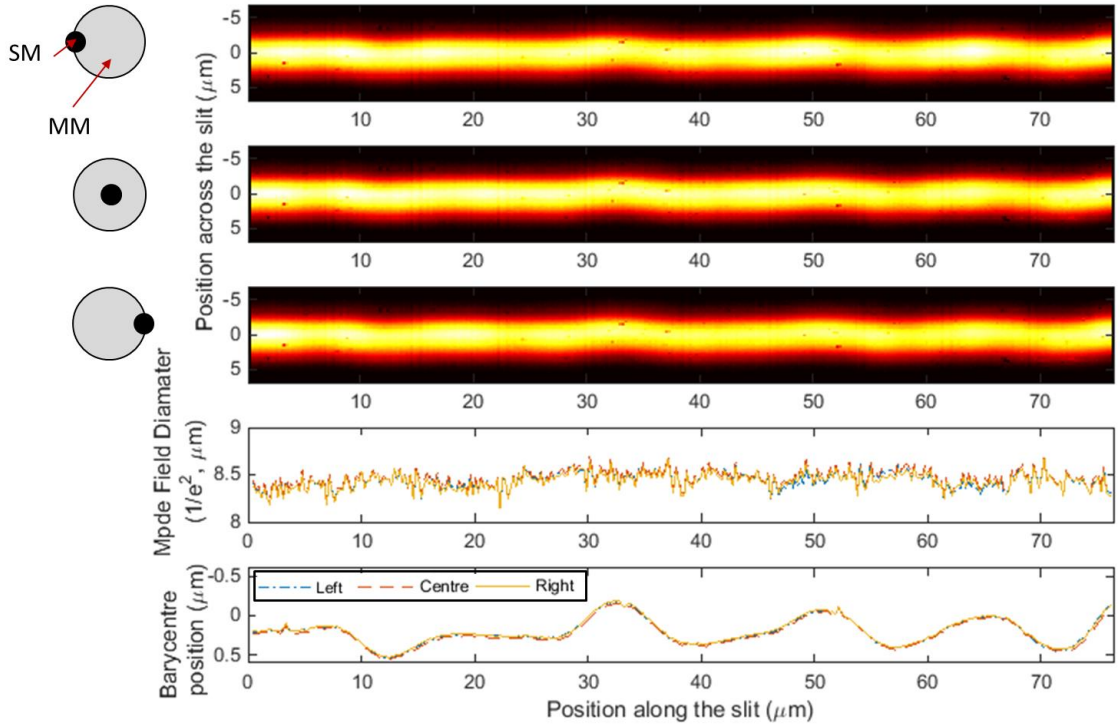

Figure 6-18 – Near field images of a ~76 μm length of the hybrid reformatter slit for three different injection positions indicated at the left of the images (Top three panels). Images obtained by recording and stacking 800 frames at a 20 ms integration time. Mode field diameter at the $1/e^2$ point (Fourth panel) and slit centre position (barycentre) (Fifth panel) calculated along the slit.

When the individual frames used to create Figure 6-18 are analysed, it is clear that the intensity along the length of the slit varies over time and the measured MFD is affected by which modes are and are not being excited in the output slab. For each of the 800 frames, the maximum and minimum MFD and barycentre position were calculated, and compared to the summed average value for each pixel column (Fig 6.19). The average variation in MFD was measured to be 1 μm, while the average variation in barycentre position was 0.6 μm. The observed variations in MFD are not unexpected, as higher order spatial modes in the slab will exhibit a reduced n_{eff} and larger MFD as a consequence. However, the variations in barycentre are unexpected and are almost certainly the result of the non-uniformity of the slit itself. These variations are exactly the type of variation in barycentre that the hybrid reformatter is designed to mitigate and it is clear that if this device were to be used in its current state modal noise would be present in the measured spectra. Encouragingly, it was observed that the hybrid reformatter acts as an extremely

efficient mode scrambler, and it is useful to note that the device operates in a similar fashion to the MM-to-SM-to-MM photonic lantern modes scrambler first proposed by Birks et al [3].

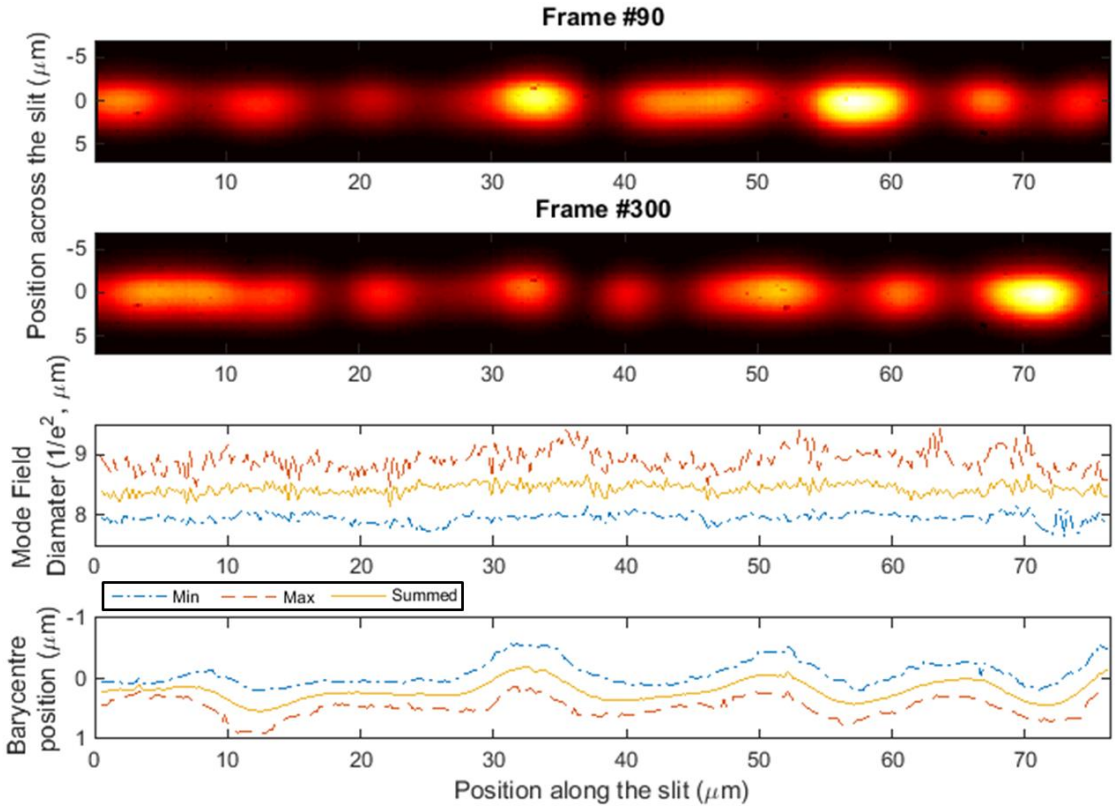

Figure 6-19 – Near field images of a 76 μm long section for two separate 20 ms frames coupling single mode 1550 nm light into the multimode end of the hybrid reformatter (top two panels). Maximum minimum and summed values of the MFD (Third panel) and barycentre position (Fourth panel) measured for each column over the 800 individual frames.

Improvements to the output array will be made to the current prototype for a future astronomical instrument. One route will be to improve the manufacture of the slit by decreasing fabrication time and stabilising the ambient conditions in the laboratory environment. An alternative solution might be to reformat the waveguides to an uncoupled linear array of single mode waveguides, rather than a planar slab, however this would significantly increase the length of the detector array used, with a subsequent penalty in read-out noise.

6.6 Conclusions and future work

The 53 % throughput of the hybrid reformatter measured on-sky is much improved from the 19.5 % on-sky throughput of the photonic dicer, and is much more feasible to be seen as a potential astronomical instrument. The hybrid reformatter on-sky throughput is also much closer to its laboratory throughput, 53 % to 69 % respectively than that of the photonic dicer, 19.5 % and 66 % respectively, due to a better matching of the multimode input of the device to the PSF achieved under median to poor seeing at the WHT. There is very little increase in throughput from open loop to closed loop operation at 48 % to 53 % respectively. This is as expected due the focusing lenses for the hybrid reformatter designed to couple the entire PSF with no CANARY correction under poor atmospheric seeing, making this experiment perfect for demonstrating high throughput, but not for showing the true power of the CANARY AO system. A secondary experimental arm tested an MCF lantern with lenses only coupling the core of the PSF to the device, this demonstrated a much greater improvement in performance of 38 % for closed-loop compared to tip-tilt CANARY operation. The straightness of the slit was investigated, with the central position shown to be relatively stable over its length with no large discontinuities between adjacent waveguides.

Future work for this device could include inscribing fibre-Bragg gratings into the MCF used in the hybrid reformatter for extinction of atmospheric absorption lines. The output of the device should also be fed into a spectrometer to produce an on-sky spectrum. Further optimisation of the ULI reformatter geometry should be performed in order to prevent waveguides being inscribed in previously modified material, which reduces throughput. Investigations into improvement of the straightness and uniformity of the pseudo-slit output should be performed and compared to a device that reformats the modes into an uncoupled linear array of waveguides.

6.7 Contributions

This work is a continuation and update to the previous device described in Chapter 5 with additional design input from Prof. Tim Birks and Dr Itandehui Gris-Sánchez of the University of Bath alongside the original team of Dr Jeremy Allington-Smith, Robert Harris and Dr Tim Morris of Durham University and Prof. Robert Thomson and David MacLachlan from Heriot Watt.

The MCF photonic lantern was designed and manufactured by Dr Gris-Sánchez.

The determination of the optimum inscription parameters, and the design and full characterisation of the various inscription geometries was performed by David MacLachlan. The designs were entered into software developed by Dr Graeme Brown of Heriot Watt to define the stage movements and produce the required G-code programs.

The set-up and alignment of the ULI setup with the Menlo laser and air bearing stages was performed by Sebabrata Mukherjee and Dr Alexander Arriola, based on an earlier setup designed by David MacLachlan. Dr Debaditya Choudhury set up the compressor and air bearing stages.

Dr Choudhury manufactured the custom V-grooves and jointly with David MacLachlan aligned and bonded the fibre and reformatter to construct the completed device.

Dr Izabela Spaleniak performed the in-laboratory throughput and performance tests of the completed device.

The on-sky test setup was adapted from that described in Chapter 5 led by Dr Morris and Robert Harris, who performed the Zemax simulations.

The setup and tests at the telescope were performed by David MacLachlan, Robert Harris, Dr Gris-Sánchez, and Dr Morris, who was key in the integration of the experiment to the CANARY AO system. The data capture software used on-sky was developed by Dr Alistair Basden from Durham University.

The code to determine the on-sky throughput of the device and the straightness of the slit was developed by David MacLachlan. This was also independently performed by Robert Harris to ensure confidence in the result. All values and images presented here for the on-sky performance were obtained from the code of David MacLachlan.

6.8 References

[1] I. Spaleniak, "Overcoming the effects of the Earth's atmosphere on astronomical observations with 3D integrated photonic technologies" (Macquarie University, 2014).

[2] B. Redding and H. Cao, "Using a multimode fiber as a high-resolution, low-loss spectrometer," *Opt. Lett.* **37**, 3384–3386 (2012).

[3] T. A. Birks, B. J. Mangan, A. Díez, J. L. Cruz, and D. F. Murphy, "'Photonic lantern' spectral filters in multi-core fibre," *Opt. Express* **20**, 13996–14008 (2012).

[4] R. R. Thomson, T. A. Birks, S. G. Leon-Saval, A. K. Kar, and J. Bland-Hawthorn, "Ultrafast laser inscription of an integrated photonic lantern," *Opt. Express* **19**,

5698–5705 (2011).

[5] R. R. Thomson, R. J. Harris, T. A. Birks, G. Brown, J. Allington-Smith, and J. Bland-Hawthorn, "Ultrafast laser inscription of a 121-waveguide fan-out for astrophotonics," *Opt. Lett.* **37**, 2331–2333 (2012).

[6] T. A. Birks, I. Gris-Sánchez, S. Yerolatsitis, S. G. Leon-Saval, and R. R. Thomson, "The photonic lantern," *Adv. Opt. Photonics* **7**, 107–167 (2015).

[7] T. Meany, S. Gross, N. Jovanovic, A. Arriola, M. J. Steel, and M. Withford, "Towards low-loss lightwave circuits for non-classical optics at 800 and 1,550 nm," *Appl. Phys. A* **114**, 113–118 (2014).

[8] E. Hog, C. Fabricius, V. V Makarov, S. Urban, T. Corbin, G. Wycoff, U. Bastian, P. Schwekendiek, and A. Wicenec, "(Erratum) Letter to the Editor - The Tycho-2 catalogue of the 2.5 million brightest stars," *Astron. Astrophys.* **363**, 385 (2000).

[9] N. O'Mahony, "RoboDIMM — The ING's New Seeing Monitor," *Newsl. Isaac Newt. Gr. Telesc.* **7**, 22–24 (2007).

[10] J. A. Nelder and R. Mead, "A Simplex Method for Function Minimization," *Comput. J.* **7**, 308–313 (1965).

Chapter 7 – Conclusions & Future Work

7.1 Overview

The work in this thesis is primarily designed to develop new astrophotonic devices using the technology of ULI. This technique allows waveguides and gratings to be inscribed within a bulk glass material enabling the potential development of low cost, compact and stable components for use with astrophotonic spectrometers.

7.2 Volume gratings

7.2.1 Conclusions

In Chapter 4, volume gratings were inscribed in a mid-infrared transmitting material, GLS. Initial tests determined the optimal pulse energy to produce gratings that provided a 60 % first order diffraction efficiency at 633 nm. A selection of thicker gratings with a greater number of layers were inscribed to create efficient diffraction at longer wavelengths. Gratings with a 65 % efficiency at 1350 nm were produced that still provide reasonable efficiencies of 30 % at 2500 nm [1]. The maximum efficiency achieved was 65 % as the transmission of the substrate is 70 % due to its high refractive index. An anti-reflective coating was applied to an inscribed substrate to provide a 95 % substrate transmission over the wavelength range 600 – 1000 nm and diffraction gratings which achieved a first order efficiency of 80 % at 1200 nm [2]. Attempts to produce thicker gratings were unsuccessful as the gratings and samples cracked and shattered due to heat accumulation and stress.

An improved x-y-z air-bearing stage and laser system was implemented and further investigations were performed. Work performed with the new laser produced a slightly higher refractive index change than previously achieved, allowing diffraction gratings efficient at longer wavelengths for the same grating thickness. A detailed investigation of grating layer separation was performed to determine the optimum layer separation to be 4 μm within the material, which increased the pulse energy range over which optimum gratings were produced, reducing the depth dependent efficiency of the gratings. Gratings producing a first order diffraction efficiency of 66 % were achieved at a wavelength of 1800 nm, still performing with a 55 % efficiency at 2500 nm. To remove the effects of Fresnel reflection and achieve the maximum possible efficiency an anti-reflection coating

was applied to a blank substrate and gratings inscribed into the treated material. The gratings performed as expected with no damage to the substrate, simply requiring a lower pulse energy for optimal performance. The best grating demonstrated an absolute diffraction efficiency of 95 % at 1020 nm. This performance is similar to that produced by currently used volume phase holographic gratings showing these devices have the potential to be used in astronomical spectrographs. Attempts to produce thicker gratings to perform with a high efficiency at wavelengths of 3.5 and 4.9 μm, the astronomical L and M bands, were once again unsuccessful due to the substrates cracking.

In an attempt to solve the issue of the sample cracking an alternative material, IG2, was investigated. Volume gratings inscribed in this material proved to be highly efficient, with the same relative thickness of gratings producing optimum first order diffraction efficiency at a longer wavelength than those produced in GLS. This indicates a much higher refractive index change induced at the laser focus. The optimum pulse energy of laser inscription was also found to be much lower than that required for GLS. For different layer thicknesses first order diffraction efficiencies of ~ 63 % were achieved at wavelengths of 1450, 1850 and 2500 nm, demonstrating a linear relationship between grating thickness and the wavelength of maximum efficiency. The IG2 material has a transmission of 67 % and similarly to GLS it can be expected that the application of an anti-reflective coating will improve the diffraction efficiency to ~ 95 %. There was no visible evidence of the sample cracking and thicker gratings were produced with an expected maximum efficiency at wavelengths of 3100 and 3950 nm respectively. The detectors and lenses used in the characterisation experiment did not work at wavelengths longer than 2500 nm and specialist infra-red detectors and sources will be required for a full characterisation. The grating predicted to have maximum efficiency at 3100 nm was tested using a 3390 nm HeNe laser and a first order diffraction efficiency of 53 % was measured at this wavelength.

7.2.2 Future work

Future work on this project will include applying and testing an anti-reflective coating to an IG2 sample. A mid-infrared characterisation set-up will be constructed to fully characterise the thickest gratings. Gratings designed to provide a maximum efficiency in the L and M astronomical observation bands will be produced. GLS and IG2 materials will be tested at cryogenic temperatures to determine if there is any change in grating

performance and confirm whether they may be suitable for low temperature applications such as space-based instruments. Larger gratings will be produced, designed for a custom microspectrograph designed and built by Dr David Lee at the UK ATC. Long term plans will include on-sky testing of these gratings as proof they are a suitable alternative to surface gratings in the mid-infrared wavelength range, combining the benefits of volume phase holographic gratings with a high mid-infrared efficiency.

7.3 Photonic dicer

Chapter 5 describes the design, fabrication and testing of a custom integrated device, the "photonic dicer" which combines a photonic lantern transition with a waveguide reformatting function into a single ULI fabricated device. The photonic lantern function accepts an AO corrected multimode telescope PSF and produces an array of single mode waveguides with low loss. The reformatting function reshapes this array of single mode waveguides into a pseudo-slit, suitable as a diffraction limited input for a spectrograph. Such an input has the potential to provide a diffraction limited input to a spectrograph allowing the size of the instrument to be decoupled from the size of the telescope aperture. This will, in principle, allow more compact and stable instruments to be developed suitable of achieving the high precision required for the identification of extrasolar planets.

Initially 7 devices of varying sizes, supporting from 4 to 49 modes were inscribed in a single substrate. These test devices consisted of two multimode to slit photonic dicers connected back-to-back with a single mode input section to facilitate full characterisation of the devices via cut-back measurements. The throughput of the PD devices falls from 70 % to 55 % at 1550 nm as the number of modes supported by the device increases due to bend losses [3]. The throughput of the devices was measured to be similar irrespective of whether the device was inscribed from multimode to slit or slit to multimode direction [4]. The single mode waveguides used to construct the PD devices were measured to be single mode over the wavelength range 1320 to 1580 nm and the throughput of a 4 mode PD device measured to be measured at 1500 and 1580 nm, and as such, the devices can be expected to perform with a similar performance across these wavelength ranges.

With the aid of the CANARY AO team from the University of Durham and l'Observatiore de Paris a 36 mode photonic dicer device was tested on-sky at the 4.2 m William Herschel Telescope in La Palma. The device was tested for a variety of AO

modes applying different levels of atmospheric correction providing a throughput of 9 % for minimal correction and 19.5 % for maximum correction [5]. The low on-sky throughput of 19.5 % compared to the 66 % measured in-laboratory is due to poor matching of the CANARY PSF to the PD input. The straightness of the pseudo-slit was measured and was found to vary slightly along the length of the slit due to the order of waveguide inscription and thermal effects within the laboratory.

7.4 Hybrid reformatter

7.4.1 Conclusions

Chapter 6 describes the design, manufacture and testing of the hybrid reformatter, an improved and updated version of the photonic dicer. The hybrid reformatter combines a photonic lantern fabricated from a multicore fibre with a ULI fabricated reformatter. This device takes advantage of the low loss nature of the MCF photonic lantern with the reformatting capability of ULI. In addition, an ideal component should be readily fed from a multimode fibre as opposed to the free space coupling required for the photonic dicer. Work performed by Macquarie University has also shown evidence of modal noise incurred at the interface between a multimode fibre and a multimode waveguide. The hybrid reformatter avoids this form of additional modal noise by connecting the discrete single mode waveguides of the multicore fibre to the single mode waveguide input of the reformatter.

The multicore fibre lantern contains 92 cores and was manufactured by the U. of Bath and has a throughput greater than 89 %. The 92 single moded waveguide input of the ULI reformatter was designed to match the array of single mode cores in the MCF, reshaping them into a slit ~570 μm long. Three different inscription geometries were tried and tested to determine the most efficient. To ensure that the slit was straight and reducing any thermal effects within the laboratory the slit waveguides were written in order from one side to the other. The measured throughput of the optimum inscription geometry reformatter was 75 % at 1550 nm. UV cured adhesive was used to permanently bond the two components to form the hybrid reformatter with a measured throughput of 69 % at 1550 nm.

The device was once again tested on-sky at the William Hershel demonstrating a throughput of 53 % with maximum AO correction [6].

7.4.2 Future work

Future work on this device would include producing a hybrid reformatter that supports a fewer number of modes to reduce the slit length while still maintaining the high throughput. A hybrid reformatter device should also be tested, feeding a spectrometer on-sky in order to fully determine whether it provides an input free of modal noise. Further optimisation of the slit design and stage accuracy is required to improve the straightness of the pseudo-slit. It may additionally be beneficial to consider alternative output arrays, such as a discrete linear array of uncoupled waveguides [7]. Bragg gratings can be inscribed within the single mode waveguides, or the multicore fibre to provide filtering of atmospheric OH emission lines.

There is also potential to investigate the combination of the reformatter and the volume gratings while taking advantage of selective chemical etching to create lenses and produce a fully integrated spectrograph component.

7.5 References

[1] D. G. MacLachlan, R. R. Thomson, C. R. Cunningham, and D. Lee, "Mid-Infrared Volume Phase Gratings Manufactured using Ultrafast Laser Inscription," *Opt. Mater. Express* **3**, 1616–1623 (2013).

[2] D. G. MacLachlan, D. Choudhury, A. Arriola, C. Cunningham, R. R. Thomson, A. Kirkham, and D. Lee, "Developing ultrafast laser inscribed volume gratings," *Adv. Opt. Mech. Technol. Telesc. Instrum. Proc. SPIE* **9151**, 91511H (2014).

[3] D. G. MacLachlan, R. J. Harris, D. Choudhury, R. D. Simmonds, P. S. Salter, M. J. Booth, J. R. Allington-Smith, and R. R. Thomson, "Development of integrated mode reformatting components for diffraction-limited spectroscopy," *Opt. Lett.* **41**, 76–79 (2016).

[4] D. G. MacLachlan, R. Harris, D. Choudhury, A. Arriola, G. Brown, J. Allington-Smith, and R. R. Thomson, "Development of integrated photonic-dicers for reformatting the point-spread-function of a telescope," *Adv. Opt. Mech. Technol. Telesc. Instrum. Proc. SPIE* **9151**, 91511W (2014).

[5] R. J. Harris, D. G. MacLachlan, D. Choudhury, T. J. Morris, E. Gendron, A. G.

Basden, G. Brown, J. R. Allington-Smith, and R. R. Thomson, “Photonic spatial reformatting of stellar light for diffraction-limited spectroscopy,” *Mon. Not. R. Astron. Soc.* **450**, 428–434 (2015).

[6] D. G. MacLachlan, R. J. Harris, I. Gris-Sánchez, T. J. Morris, D. Choudhury, E. Gendron, A. G. Basden, I. Spaleniak, A. Arriola, et al., “Efficient photonic reformatting of celestial light for diffraction-limited spectroscopy,” *Mon. Not. R. Astron. Soc.* **464**, 4950–4957 (2017).

[7] I. Spaleniak, D. G. MacLachlan, I. Gris-Sánchez, D. Choudhury, R. J. Harris, A. Arriola, J. R. Allington-Smith, T. A. Birks, and R. R. Thomson, “Modal noise characterisation of a hybrid reformatter,” *Adv. Opt. Mech. Technol. Telesc. Instrum. II. Proc. SPIE* **9912**, 991228–991229 (2016).